SMALL SCALE TESTING TO ASSESS MECHANICAL BEHAVIOR OF ANISOTROPIC MOLECULAR CRYSTALS

by

Alexandra Burch

A Dissertation

Submitted to the Faculty of Purdue University

In Partial Fulfillment of the Requirements for the degree of

Doctor of Philosophy

School of Materials Engineering

West Lafayette, Indiana

May 2020

THE PURDUE UNIVERSITY GRADUATE SCHOOL
STATEMENT OF COMMITTEE APPROVAL

Dr. David Bahr, Chair
School of Materials Engineering

Dr. Teresa Carvajal
Department of Agricultural & Biological Engineering

Dr. John Howarter
School of Materials Engineering

Dr. Steven Son
School of Mechanical Engineering

Dr. John Yeager
Los Alamos National Laboratory

Approved by:
Dr. David Bahr

For my dad, Dr. John Russell Burch Jr., my favorite Dr. Burch.
"In the infamous words of Elza Fain Burch, it will toughen you up"

ACKNOWLEDGMENTS

I have been fortunate to have an exceptional amount of help and support during the course of this work, and I have many people to thank for that. I'd first like to thank Dr. David Bahr and Dr. John Yeager for imparting seemingly infinite amounts of knowledge, advice, and support. I would also like to thank my advisory committee members, Dr. Theresa Carvajal, Dr. John Howarter, and Dr. Steven Son, for their significant contributions and encouragement.

I have had the privilege of working at Los Alamos National Laboratory while completing this work, which was made possible by the financial support of the Delivery Environments Program at LANL under Dr. Antranik Siranosian. Much of the experimental work was performed at the Center for Integrated Nanotechnologies, where Dr. Nan Li graciously allowed me to commandeer the nanoindenter for months at a time, and Dr. Jonathan Gigax provided me with technical support.

I would like to give an enthusiastic thanks to Dr. Raheleh Rahimi, whose presence has been truly invaluable to me, for providing help and answers at every turn; I cannot adequately stress how much I have valued the opportunity to work with you and learn from you. I would also like to thank Dr. Amanda Higginbotham Duque for mentorship, encouragement, and help with obtaining materials and subsequent crystallization.

It was not without incredible academic support and advising during my years of undergraduate study that I began this endeavor, and for that I would like to sincerely thank Dr. Matthew Beck, who was an incredible support to me during my time studying materials science at the University of Kentucky and somehow even more so upon my departure, and Dr. Christopher Bullock, who I had the pleasure of learning from and being continuously challenged by during my time studying mathematics at Campbellsville University.

I am incredibly grateful for the constant support from my friends, Amber Dawn Bright and Jaelynn Dawn Bright, Hannah and Craig Shepherd, Michelle Wolfe, Dr. Anna Walter, Stacia Campbell, Efam and Laila Whitt, Devin and Adam Caldwell, and Samantha Robillard, who all listened to my many frustrations, encouraged me, and provided stress relief in the form of visits, adventures, nights out, and nights in. I'd also like to thank Dr. Connor Callaway for his great support and its development over the last 7.5 years.

I have been so grateful for Abbie and Mayor these last several years, they are truly an endless source of unconditional love and comfort, and have kept me company on countless evenings while I worked and studied.

I would like to thank Dr. Andrés A. Villa Pulido for an immeasurable amount of support, which has included moving 1300 miles across the country for my job. I am so grateful for everything you do and everything you are.

I am also incredibly grateful to my family for their love and their endless belief in me. I would especially like to acknowledge my tia, Stacey Burch O'Malley, my grandfather, John Russell Burch Sr., and my grandmothers, Donna Crawford and Idalia Burch, for the gift of their love and support. My nephews, Samson Hunter Melvin and Callum Leon Melvin, have been an incredible source of joy during this process. I'd like to thank my sisters Morgan Melvin and Kayleigh Burch; having sisters has been one of the greatest blessings of my life. I'd also like to thank my mom, Samantha Burch, for absolutely everything. Whether I've needed a moving truck, a dog sitter, a safe place to escape to in times of great stress, a shoulder to cry on, a friend, or anything in between, you have been there.

Finally, I would like to thank my dad, Dr. John Russell Burch Jr. This opportunity to share the title of Dr. Burch with you is one of the greatest honors of my life, second only to the immense privilege of being your daughter.

TABLE OF CONTENTS

LIST OF TABLES

LIST OF FIGURES

ABSTRACT

Due to the inherent dangers associated with handling high explosive materials, it is often useful to have access to inert simulant materials that mimic certain physical or mechanical properties, called "mock" materials. Mock materials can take the place of explosives in experiments, allowing experimental results to be obtained with less difficulty and risk. Recently there has been an interest in identifying new mechanical mock materials for the explosives HMX and PETN. These energetic materials and their prospective mocks are often used and tested in the form of small submillimeter crystals, with which typical size and geometry make many mechanical tests difficult or impossible. Additionally, these materials are typically prone to brittle fracture, which can further limit the usage conditions of the material as well as the range of conditions in which mechanical testing results are valid. Nanoindentation is a useful technique to measure mechanical properties in particulate form without the need to grow large single crystals or do additional processing on existing crystals.

Here, nanoindentation tests were performed on PETN, HMX, and several inert molecular crystals selected as potential mocks based on density, crystal structure, and previous thermal testing results. Comparisons were made on the basis of hardness, elastic modulus, yield point behavior, indentation fracture response, and sensitivity to non-uniform indenter orientation. Based on the results of these experiments, the inert material idoxuridine was selected for further consideration as an HMX mock, and the inert materials meso-erythritol and 2,4,6 trifluorobenzoic acid were selected for further consideration as PETN mocks.

As a result of this study, potential mechanical mocks were selected for two energetic materials, nanomechanical properties were reported for the first time ever for 6 inert molecular crystals, and nanoindentation was shown to be a versatile tool for rapid initial screening of materials as well as detailed investigations of materials of interest.

1. INTRODUCTION

1.1 Molecular Crystals

Molecular crystals, in the current context organic molecular crystals, are molecules organized into a crystal lattice and held together with weak intermolecular forces[1]. These are distinct from other types of crystals, such as ionic or metallic, because of these weak intermolecular forces holding together discrete molecules; other types of crystals tend to have strong intermolecular forces binding individual atoms or ions. These weak forces characteristic of molecular crystals work alongside strong intramolecular forces that exist within the molecules themselves; but the lack of strong intermolecular forces can cause molecular crystals to be prone to defect formation during crystallization, as these weak forces fail to orient molecules effectively as they arrange themselves into the crystal lattice (though this can be helped by slowing the crystallization process). Some common molecular crystals include sugar, aspirin, and ice.

This group of materials spans a wide array, including materials such as pharmaceuticals, foods, and explosives. They are often processed in powder or particulate form, due in part to their brittle nature and in part to their applications, where high surface area may be desirable (e.g. faster drug dissolution rate). Measurement of mechanical properties of molecular crystals is of great interest as they impact compaction [2–6], amorphization[7,8], and contribute to composite mechanical properties when formulated with a binder [9]; however, testing the mechanical properties of these powders and small powder-like particles can be difficult, due both to the small size of many of these materials in their as-formed state as well as the anisotropy and brittleness that molecular crystals are known for. Testing can also be difficult with regard to forming or machining samples to meet standard mechanical test geometries. While particulate materials may be more difficult to test mechanically than larger samples, a larger sample may not be representative of the mechanical behavior of the particulate, particularly in molecular crystals where producing a larger crystal often requires altering the growth conditions that are used in precipitation of particulate matter[10].

1.2 Explosives

While explosive materials are nothing new, the intentional engineering of explosives is a newer technology. The explosive/pyrotechnic material black powder has been used for millennia in applications such as fireworks and smoke signals. In 1846, the explosive material nitroglycerin was discovered, though it was finicky and extremely dangerous. In efforts to create a safer and more reliable explosive option, Alfred Nobel invented nitroglycerin-based dynamite in 1866, with the inert material kieselguhr added as a stabilizer[11]. In the late 19th century came "smokeless powders" which were used extensively in World War I. The early 20th century also saw the introduction of TNT. With World War II came the introduction of military explosives cyclotrimethylene-trinitramine (RDX) and pentaerythritol tetranitrate (PETN), and later cyclotetramethylene-tetranitramine (HMX)[12].

Energetic materials are commonly sorted into one of three categories: explosives, propellants, and pyrotechnics. Explosives stand out among these categories due to the ability of many to detonate, which is a decomposition reaction producing gas and heat with a propagation velocity exceeding the speed of sound in the detonating material [13]. Due to this extremely rapid reaction rate (with detonation velocity typically between 1-9 km/s), in order for the reaction to sustain itself the fuel and oxidizer must be contained on the same molecule. In organic explosives, which often occur in the form of molecular crystals, the fuel is carbon and is on the same molecule with the necessary oxygen, typically separated by a nitrogen atom. Therefore, these explosives will have the general chemical makeup $C_wH_xN_yO_z$.

Explosives can be further categorized into high and low explosives: high explosives possess the ability to detonate, whereas low explosives can only escalate to deflagration. High explosives (HE) can then be separated into those that are primary, secondary, or tertiary. Primary HE detonate very easily, secondary less easily, and tertiary are the most difficult materials in which to initiate detonation and are often called insensitive high explosives. The boundary between primary and secondary explosives is set by PETN, generally accepted as the most sensitive secondary explosive, meaning that any explosive more sensitive than PETN is considered to be primary[14].

These materials are not often used in their pure crystalline form, but rather they are typically used in composite systems with polymer binders. In the composite form, these materials are called plastic bonded explosives (PBX). One common PBX is PBX 9501, composed of 95% HMX and 5% binder. While it is typical for most explosives to be used in the form of a PBX, some materials such as PETN are often used neat, meaning pressed as a pure material with no binder; however, PETN is also used in composite systems in products such as Primasheet, and Primacord.

Many of the explosive materials mentioned here including HMX and PETN are molecular crystals, meaning that along with the challenges of working with energetic materials they also bring the aforementioned challenges of working with molecular crystals such as anisotropy and brittleness.

1.3 Mock Materials

Given the inherent danger associated with explosives and other energetic materials, handling these materials can often require extensive safety measures. Experiments with these materials, therefore, can be difficult and expensive. In order to eliminate these safety concerns that are specific to energetic materials, it is helpful to have an inert material that simulates properties of the energetic and therefore can be used in place of the energetic in certain experiments. Such a material is referred to as a "mock". Depending on the type of result that is to be replicated with the mock, different properties may be of interest. For example, thermal mocks can be expected to behave similarly to their explosive counterpart in various thermal conditions and processing, with the notable exception of environments that would lead to detonation. Mechanical mocks can be expected to behave similarly to their explosive counterpart in scenarios where a force is expected to be applied to the material.

Sucrose has previously been used as a mock material for the energetic materials RDX, HMX, and PETN [15,16]. The mechanical properties of these materials have been tested using nanoindentation by Ramos et al and Taw et al.[17–19] Ramos tested the (100) and (001) planes of single sucrose crystals and found that the elastic modulus of the (100) plane was 38 GPa, that the elastic modulus of the (001) plane was 33 GPa, and that the hardness of the material, relatively independent of orientation, was approximately 1.5 GPa. Ramos later tested the (210), (021), and

(001) planes of RDX and obtained elastic modulus and hardness values of 21.0 and 0.672 GPa, 18.2 and 0.681 GPa, and 16.2 and 0.615 GPa, respectively. Taw later reported the modulus and hardness of HMX to be 24.5 GPa and 0.99 GPa respectively[19], and the average modulus and hardness of RDX to be 19.1 GPa and 0.741 GPa respectively[20]. By these measures, the elastic modulus of sucrose (001) and HMX are 35% different, and the elastic modulus of sucrose (001) and RDX (210) are 57% different. These differences are even larger if other planes of sucrose and RDX are considered. These differences in properties are relatively large, but in cases such as these, a material such as sucrose can be desirable for reasons such as affordability, availability, good particle size distribution match, or ease of crystallization.

Acetaminophen [21] and pentaerythritol [22] have also been used to mock HMX, but both these materials as well as sucrose have lower density than HMX, which has a density of 1.902 g/cm^3, whereas acetaminophen, sucrose, and pentaerythritol have densities of 1.295 g/cm^3, 1.587 g/cm^3, and 1.393 g/cm^3 respectively. Yeager et al. recently identified three inert materials with densities more similar to HMX that could serve as potential mocks[23], as well as being similar in other properties, such as thermal stability and crystal structure, the three materials being 5-iodo-2'-deoxyuridine (IDOX), 2,3,4,5,6-pentafluorobenzamide (PFBA), and N,N'-bis(2,3,4,5,6-pentafluorophenyl)oxamide (N-BPFPO). Three more materials had initially been under consideration as potential HMX mocks: 4,5-methylenedithio-1,3-dithiol-2-one (MDTTO), 1-(2-iodo-ethyl)-2-methyl-5-nitro-1H-imizadole (MET-I), and pentafluorobenzeneboronic acid (PFBBA). However, Yeager et al. were in pursuit of a thermomechanical mock for HMX, and MDTTO, MET-I, and PFBBA were found to be too dissimilar in thermal properties as measured by differential scanning calorimetry (DSC), shown in Figure 1.1.

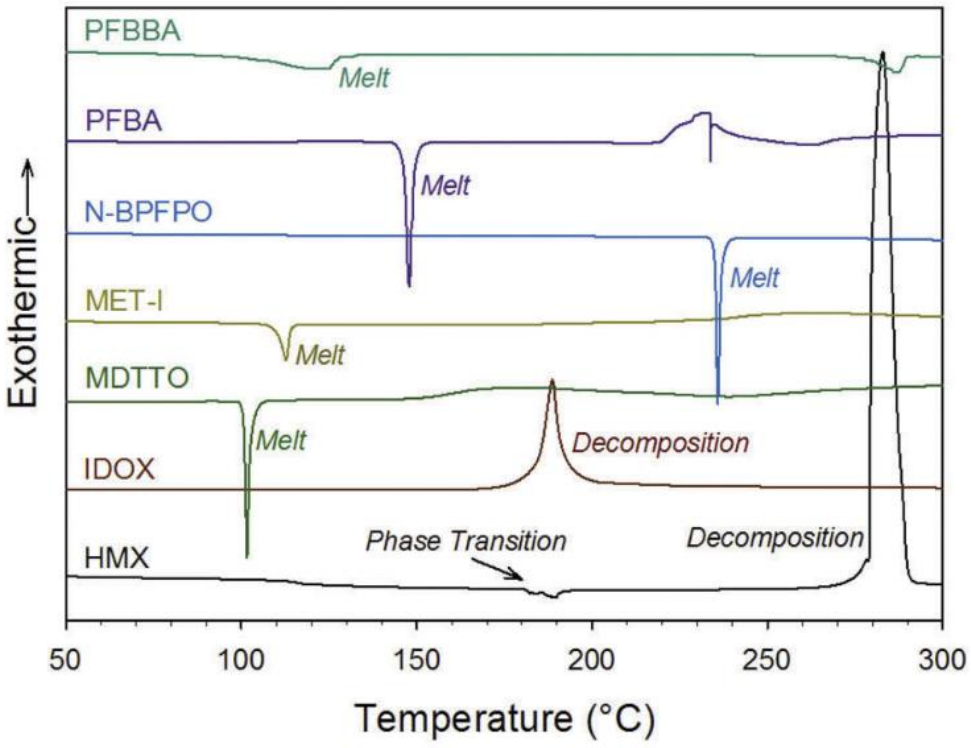

Figure 1.1 *DSC data for HMX and its initial mock candidates as selected by Yeager et al.*[23] *Polymorphic behavior was not indicated for any materials except HMX.*

Similarly, PETN has also been of interest recently in terms of finding a suitable mock material. An inert mock candidate, meso-erythritol, has recently been proposed by Wilde et al[24].

In the previous examples of work done by Ramos and Taw, the focus was on quasistatic mechanical responses of explosives as well as an inert molecular crystal that is commonly used as a mock material, with nanoindentation used as the primary characterization technique. This study will continue to focus on mechanical properties of explosives, as well as their potential mocks, as characterized via nanoindentation.

1.4 Nanomechanical testing

Mechanical tests measure a material's response to a physical force. The applied force can come in many forms; the force may subject the material to tension, compression, torsion, or some combination of the three; the force may be applied to the sample as a whole, or to a localized area; the magnitude of applied force may be large or small, and may be constant or change over time; the force may be instantaneous or applied for an extended time period. This

obviously allows for an enormous variety of mechanical tests to exist, and allows for an enormous variety of tests to be performed on a single material. One popular variety of mechanical tests is hardness testing, in particular indentation hardness testing.

Early indentation tests were introduced in the late 19th century with spherical contact models by Hertz[25] and Auerbach[26], followed by the introduction of the Brinell hardness test[27], the Meyer hardness test[28], all using spherical indenters, and the Rockwell hardness test which typically uses a conical probe. With the introduction of the Vickers indentation test came the use of pyramidal indenter probes[29]. Vickers indentation probes are four-sided pyramids with an included angle of 136° (an angle chosen to relate to typical Brinell *d/D* ratios where *d* is the chordal diameter of the residual indent impression and *D* is the diameter of the spherical probe). Vickers hardness tests are *micro*hardness tests, which means typical applied loads are less than 1000 g, and in a Vickers microhardness test, the material is indented and then the indent impression is optically measured. Following Vickers, one particular indenter probe was designed called a Berkovich which is also a pyramidal geometry, but now three-sided instead of four-sided. Three-sided pyramids have an advantage in that the three planes of the pyramid necessarily meet at a point, making a pointed tip far easier to achieve and maintain than for a four-sided pyramid. Berkovich probes have an included angle of 142.3°, an angle chosen to have the same projected contact area as a Vickers probe[30]. Later, microhardness tests were created in which the instrumentation could continuously measure applied load and indentation depth during the test[31,32], a method now known as nanoindentation regardless of scale.

1.4.1 Nanoindentation

Nanoindentation is a common small-scale instrumented indentation method that has previously been applied to single molecular crystals[17,19,20,33–38] as well as plastic-bonded composites of molecular crystals[39]. During nanoindentation, a load on the order of uNs to mNs is applied to the surface of a material via a diamond probe. The tip of this probe typically measures on the order of a few hundred nm, and is typically either pyramidal, conical, spherical, or a flat punch. During the indentation experiment, both applied load and vertical depth/displacement of the probe into the material are measured continuously. This information is then reported

graphically with load on the y-axis and depth on the x-axis, a load-depth curve, as shown in Figure 1.2[40].

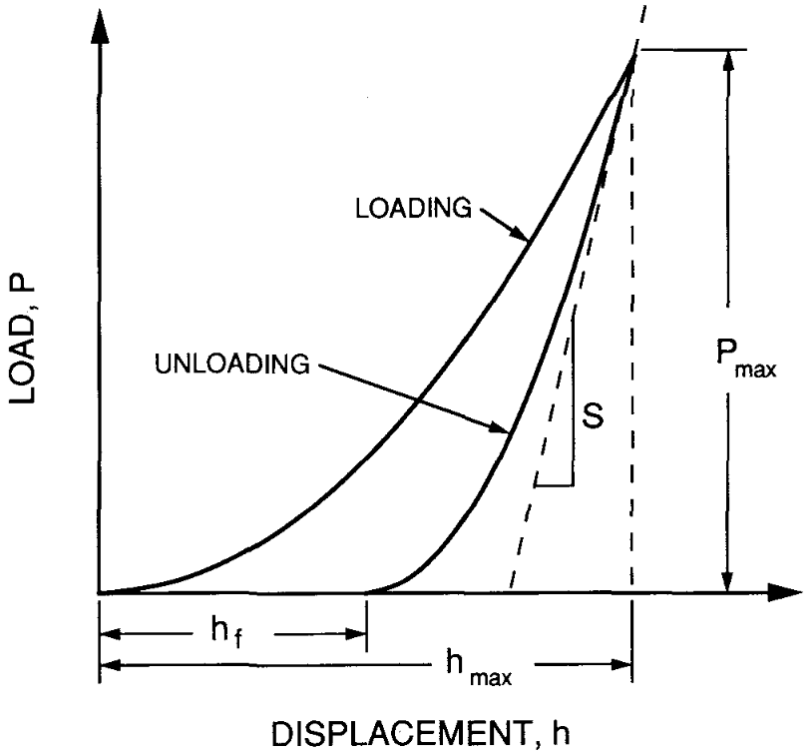

Figure 1.2 *A representation of a load-depth curve resulting from a nanoindentation test*[40].

Key features of a load-depth curve are: the maximum applied load P_{max}, the maximum depth of indentation h_{max}, and the final depth of indentation after elastic recovery, h_f. The initial portion of the unloading curve is assumed to be linear, and the slope of this initial unloading is the stiffness S. Material response during loading is both elastic and plastic in nature, but unloading is assumed to be purely elastic, allowing information about a material's elastic properties to be determined using this elastic unloading.

The initial loading portion of the load-depth curve, which is often elastic, can be described with the Hertzian elastic contact model [41], calculated using Equation 1.1. In this equation, P is the applied load, R is the radius of the indenter probe, δ is the depth of indentation, and E_r is the reduced elastic modulus of the indented material, which will be discussed with Equations 4 and 5. When plastic deformation begins, the Hertzian elastic contact model is no longer valid to describe loading behavior.

$$P = \frac{4}{3} E_r \sqrt{R\delta^3} \tag{1.1}$$

Hardness of the material is calculated using Equation 1.2. In this equation, P_{max} is the maximum load that is applied to the material during indentation, and A is the projected contact area of the indent. Projected contact area will be discussed later in this section.

$$H = \frac{P_{max}}{A} \tag{1.2}$$

Hardness measured by nanoindentation is related to yield stress linearly by a constraint factor C, shown in Equation 1.3 [42]. C is typically approximately 3 for metals, and less for brittle materials. This relationship allows the results of a nanoindentation test to be related to the results of a tensile test in cases where a tensile test is not possible.

$$H = CY \tag{1.3}$$

Reduced elastic modulus is calculated using Equation 1.4. In this equation, S is the stiffness of the material, which is the slope of the initial unloading portion of the load-depth curve (depicted in Figure 1.2), A is the projected contact area of the indent, and β is a constant based on the indenter probe geometry.

$$E_r = \frac{S\sqrt{\pi}}{2\beta\sqrt{A}} \tag{1.4}$$

The elastic modulus calculated from a nanoindentation test is reduced elastic modulus, E_r. Reduced elastic modulus is related to elastic modulus by Equation 1.5, in which E is the elastic modulus of the material, v is the Poisson's ratio of the material, and E_i and v_i are the elastic modulus and Poisson's ratio of the indenter probe. The nanoindenter reports reduced elastic modulus rather than actual elastic modulus because the load is applied via a diamond probe which may deflect some due to the load rather than transferring the entire load to the material in question. While E_i and v_i for the diamond indenter tip are known (1141 GPa and 0.07, respectively), we do not know for certain the Poisson's ratio of these samples, and therefore this paper reports only E_r; however, this effect typically is small, and E_r is generally a very good approximation for E.

$$\frac{1}{E_r} = \frac{(1-\nu^2)}{E} + \frac{(1-\nu_i^2)}{E_i} \tag{1.5}$$

As previously mentioned, the contact area *A* used in Equations 1.2 and 1.4 is not necessarily the true contact area, but rather a projected contact area. Contact area during indentation is not measured, as the only quantities measured directly are applied load and depth of indentation. In order to determine contact area from this information, a calibration is done in which a material with precisely known elastic modulus (typically fused quartz) is indented many times over a range of depths, and the contact area determined using the measured depth, stiffness, and elastic modulus. The contact area calculated for these depths is interpolated to form a function relating indentation depth to contact area, and this function then makes that conversion for subsequent indents. A consequence of this is that a sample with a tilted surface may not fit this idealized relationship between depth and contact area, and the projected contact area used for property measurements may not be accurate [43]. Therefore, in order to ensure the accuracy of the projected contact area and thus property measurements, nanoindentation samples should have minimal surface roughness (or at least a degree of surface roughness that is significantly less than the indentation depth) and a level surface.

Despite well-known limitations of molecular crystals in accommodating plasticity [18], plastic deformation resulting from an indentation can cause a plastic deformation zone in the material around the indent with a radius approximately twice the radius of the indent impression[18,38]. Because of this, subsequent indents must be separated by more than twice the indent impression radius in order to prevent interaction with this deformation zone from influencing an indentation test.

1.4.2 Incipient Plasticity

When initial loading is elastic, the onset of plasticity during indentation can be seen on the load-depth curve as a sudden increase in displacement during loading, a feature known as a pop-in, excursion, or yield point, seen in Figure 1.3 as "Displacement Discontinuity P" [44].

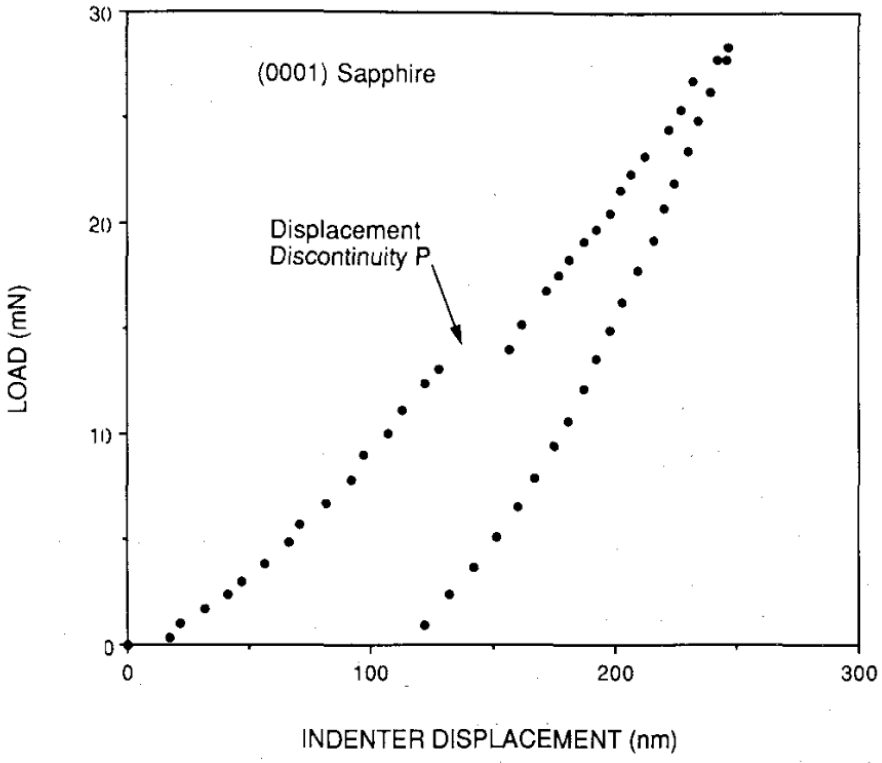

Figure 1.3 *A "pop-in" or "displacement discontinuity" indicating the transition from elastic to plastic deformation during a nanoindentation test of sapphire* [44]

Generally, if there are no excursions, then either deformation was purely elastic and the unloading curve will perfectly trace the loading curve with no residual impression left in the indented material, or otherwise the material experiences elastic-plastic deformation during the entire loading process.[44] A material that is extremely high in defect density may not experience a pop-in but rather plastically flow during the entire indentation, whereas materials with lower defect density may require a certain amount of force in order to nucleate dislocations or activate existing dislocations before plastic deformation begins [45–48]. Therefore, pop-in behavior can generally indicate defect density.

It can, however, be difficult to determine exactly what type of defect led to a particular pop-in event, be it dislocation nucleation[49], movement of pre-existing dislocations[46], or interaction with a point defect[50]. A strong indicator for this can be in both the shear stress at yield τ as well as the range of variation of this stress between multiple indents in the same material. Shear stress can be calculated using Equation 1.6, and is valid for Hertzian loading, that is, fully elastic loading, which should be the case right up to the yield point.

$$\tau = 0.31 \left(\frac{6\overline{E_r}^2}{\pi^3 R^2} \right)^{1/3} P^{1/3} \quad 1.6$$

When repeated indentation tests show pop-ins repeatedly occurring at approximately the same stress, and that stress approaches the theoretical shear stress, then this is indicative of dislocation nucleation in a volume with low defect density[51,52]. The alternate case is that where repeated indentation tests do not show a particular trend in yield stress but rather a wide and stochastic range, and at lower stresses relative to the theoretical shear stress, then this suggests that the source of plasticity was activation of existing defects within the material[46,50].

The indentation yield stress of a material can vary as a result of quite a few different influences. For example, there is some degree of size-dependency in yield, where smaller volumes have been found to yield at higher stresses than in larger volumes of the same material[53]. Temperature can also have a very slight effect, as increased temperature lowers the energy barrier to yield[50]; this effect is extremely minimal, with experiments on platinum showing only about a 5 μN variation in load at yield between temperatures of 25°C and 200°C. Crystallographic orientation is another factor that has been found to affect yield point, with some crystallographic planes quicker to yield than others in the same material[18,54]. Surface preparation method can also affect yield point, as actions such as polishing or washing the surface with a solution can influence defects that may then be activated during indentation[55].

1.4.3 Indentation Fracture

Nanoindentation can also be used to determine fracture properties [56–65]. Given the brittle nature of molecular crystals, material failure during mechanical testing is quite common. If the material fails during mechanical testing, then the properties measured may not be representative of the undeformed material or suitable for comparison to simulations for finding new mock compositions. For example, the Oliver and Pharr method of calculating elastic modulus and hardness via indentation [40] is only valid for materials that did not fracture during indentation. Therefore, understanding the indentation fracture behavior of a brittle material provides confidence in measurements that are taken without causing fracture.

The topic of indentation fracture has been covered extensively, with a thorough consideration given to the topic by Lawn and Wilshaw[56], beginning with the indentation stress

field. As described by Lawn and Wilshaw, a stress field forms when the indenter comes in contact with the material. This stress field can concentrate very high stresses locally at sharp contacts, whether the sharp contact is along a line or at a point. Inelastic deformation may serve to temper the sharp contrast of these stress concentrations and the adjacent areas where stresses are much lower. The magnitude of these concentrated stresses and the degree of difference in adjacent lower stress areas can be affected by factors such as indenter geometry and magnitude of mechanical anisotropy (which we know to be significant in molecular crystals). The stress field intensity, p_0, is then generally described by Equation 1.7,

$$p_0 = \frac{P}{\alpha\pi a^2} \tag{1.7}$$

where P is the applied load, a the radius of indenter contact, and α a dimensionless constant to account for indenter geometry. One may notice that this is strikingly similar to the equation by which hardness is calculated, Equation 1.2, and indeed p_0 remains constant with hardness, as later defined by Lawn and Marshall that hardness is equivalent to p_0 multiplied by π[66].

This understanding of the indenter stress field lends to an understanding of fracture mechanics in that material. In order for fracture to occur in a material, there must first be a flaw, whether pre-existing or purposefully induced (such as with indentation). When multiple flaws exist, local stress concentrations will determine which will predominate subsequent fracture events. Once fracture has been initiated at a given flaw, propagation is then driven by several factors that ultimately relate to the energy released by crack propagation, as described by Equations 1.8 and 1.9, in which Equation 1.9 is a derivative of Equation 1.8:

$$U = (-W_L + U_E) + U_S \tag{1.8}$$

$$\frac{dU}{dC} = \frac{d(-W_L + U_E)}{dC} + \frac{dU_S}{dC} = -G + 2\Gamma \tag{1.9}$$

Here, U is the total energy, W_L is the work of the applied forces, U_E is the elastic strain energy in the cracked body, and U_S is the total surface energy of the cracked walls. In equation 1.9 then, the rate of change is considered with respect to C, crack area. Here, G is the mechanical energy release rate, and Γ is the fracture surface energy. Γ is then equivalent to reversible surface energy γ when there is no dissipative component in creating new crack surfaces. When total

energy is constant, it then follows that G is equal to 2Γ. When G exceeds 2Γ, that is when the mechanical energy release rate is more than double the fracture surface energy, then crack propagation occurs.

Following crack initiation, cracks then propagate along paths which had lower stresses prior to fracture. This propagation path can be strongly influenced by orientation dependence, particularly in anisotropic materials such as molecular crystals. In isotropic systems, cracks will prefer to form along sharp indenter edges, but in anisotropic system preferred cleavage planes may dominate. The preferred propagation path may or may not be visible from the indentation surface, but rather extend into the material below the surface. In Lawn and Wilshaw's work, all cracks were expected to be subsurface, and surface crack traces were thought to be subsurface cracks that had propagated far enough to eventually experience "breakthrough" to the surface. This was later disproven, as Cook and Pharr showed that surface-level cracks could occur independently of subsurface cracks[67].

Lawn and Marshall defined toughness of an indented material, K_c as in Equation 1.10,

$$K_c = \frac{P}{\beta_0 c^{3/2}} \tag{1.10}$$

where β_0 is a geometric constant and c is the length of the radial/median crack. This raises two concerns: first, that it requires measurement of the crack length. Indeed, many indentation fracture analysis methods require post-indentation imaging to identify the presence of a crack, in which case particularly small or subsurface fracture may go undetected. Because of this, Equation 1.10 may be difficult to apply or even entirely incorrect when cracks are unseen or only partially visible and therefore mis-measured.

The second concern with Equation 1.10 is that it is presented as a K_c measurement. It is difficult to apply the concept of a K_c or a K_{1c} to indentation fracture events, as these toughness measurements are defined as measuring the resistance to propagation of an existing flaw. As previously discussed, fracture that occurs during indentation often emanates from a flaw that is created during the course of the indentation. Because of this discrepancy, rather than K_c or K_{1c}, indentation toughness is now often defined by the variable T. Various models have been

proposed for *T*, one from Jang and Pharr shown as Equation 1.11[68], and another from Morris and Cook shown as Equation 1.12[69]:

$$P_C = C\left(\frac{H}{E}\right)^2\left(\frac{T}{H}\right)^3 T \tag{1.11}$$

$$\frac{P}{c^{3/2}} = \frac{T}{\chi^R} - \frac{\chi^E}{\chi^R}\frac{P}{c^{3/2}}\ln\left(\frac{2c}{P^{\frac{1}{2}}}(\alpha H)^{1/2}\right) \tag{1.12}$$

where P_C is the critical load to initiate fracture, C is an agglomeration of geometric constants that address indenter shape and the stress fields around the indenter, χ^E is a dimensionless stress-intensity factor amplitude term, χ^R varies with hardness and elastic modulus as well as incorporating a geometry factor, and α relates to the projected contact area. Equation 1.12 requires a crack length measurement, which has been mentioned as a concern, whereas Equation 1.11 does not require a crack length measurement and in fact only requires known constants and data gathered from an indentation test.

Given the difficulties that can arise with fracture analysis techniques that require optical inspection, it is beneficial to have a non-optical detection method. In order to identify cracks without this visual inspection, Morris et al [70] introduced a technique in which presence or absence of a crack is indicated by analysis of the indentation unloading traces. This was accomplished by indenting a material multiple times using probes of varying acuity, ranging from Berkovich as the broadest, with an included angle of 142.3°, to cube corner as the most acute, with an included angle of 90°. The unloading portions of the resultant load-depth curves were plotted together, as seen in Figure 1.4, and if the unloading curves were not superimposable or nearly superimposable, then the material was found to have fractured.

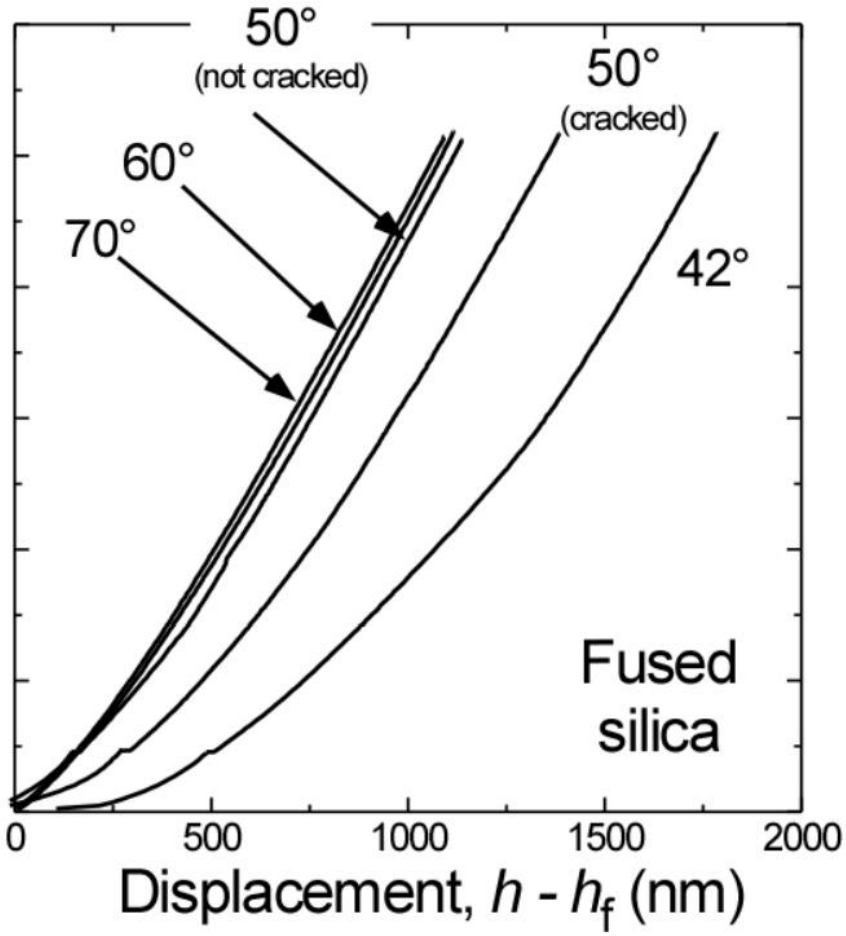

Figure 1.4 *Morris' depiction of the superimposability of the unloading portions of load-depth curves when cracking has not occurred, and the nonsuperimposability when cracking has occurred via sufficiently acute indenter probes* [71].

This variation in unloading slope, dP/dh, which is described as the stiffness, can be observed in the power-law function for unloading P-h behavior during unloading at an elastic-plastic contact, Equation 1.13[40,72]

$$P = F(h - h_f)^m \tag{1.13}$$

Where m is the unloading exponent and F is a constant, both found from a best-fit of this equation. The unloading slope, stiffness, is then found by differentiating Equation 1.13 with respect to h. In indentation, broad probes apply a largely normal force to the surface with only some lateral displacement of material, whereas an acute indenter acts like a "wedge"[69], driving significant lateral displacement and upon fracture driving radial cracks outward. Therefore,

during a fracture event, this *m* exponent is impacted for particularly acute indenter geometries, while more broad probes can induce fracture without impacting *m*. The result of this is an unloading slope altered by fracture events for particularly acute indenters, which would cause it to deviate from the slope achieved by an unfractured indent or even a fractured indent from a broader probe.

This unloading slope analysis method specifically detects the occurrence of radial cracks, which are parallel to the indentation axis and typically originate from the corners of the indent impression [67], as shown in Figure 1.5(a). There can also exist secondary radial cracks, shown in Figure 1.5(b), which occur at an angle to the indentation axis rather than parallel, and typically are adjacent to the corners of the indent impression. During indentation fracture events, it is also possible to observe lateral fracture [67], shown in Figure 1.5(c), though this mechanism is not detected by unloading analysis. Lateral cracks appear parallel to the material surface, emanating outward in a circle below the plastic deformation zone. "Shallow" lateral cracks as shown in Figure 1.5(d) may appear less symmetrically and closer to the indented material surface.

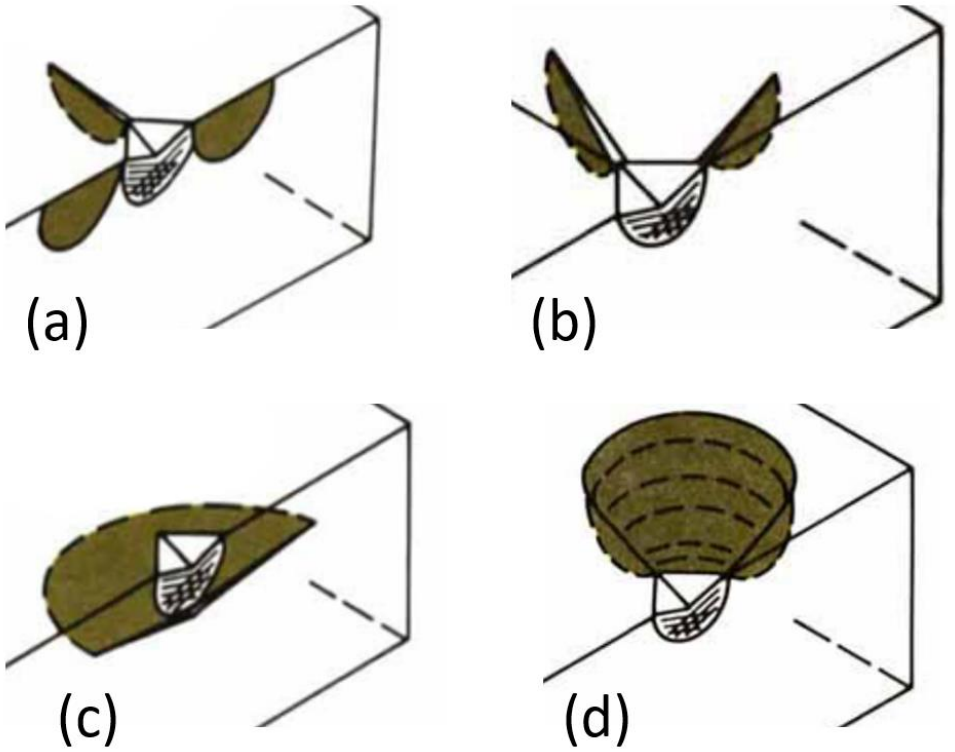

Figure 1.5 *Representations of (a) radial fracture, (b) secondary radial fracture, (c) lateral fracture, and (d) shallow lateral fracture*[67]

Another indication of fracture besides differing unloading slopes can be the presence of a pop-out. Similar to a pop-in during loading, there can also be a sudden change, a decrease, in displacement without a corresponding change in load during *un*loading, called a pop-out. An example of a pop-out can be seen in Figure 1.6.

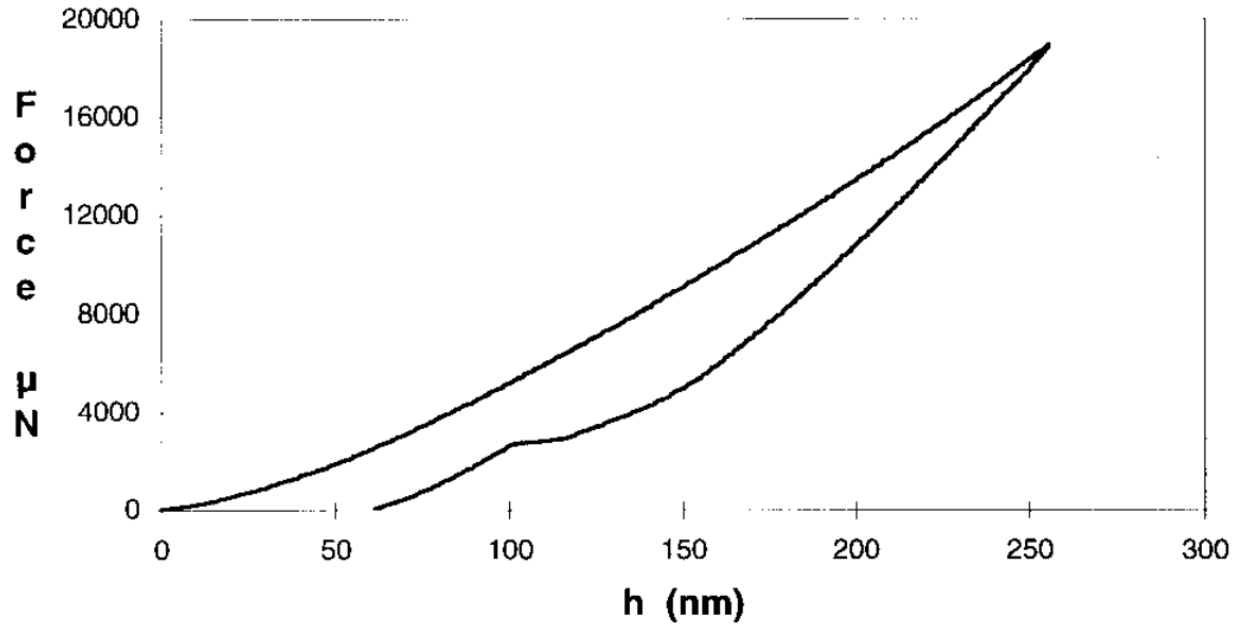

Figure 1.6 *A "pop-out" indicating a density change resulting from an indentation-induced phase transformation in Si*[73].

Pop-outs can be attributed to different phenomena. The example shown in Figure 1.6 is of a pop-out that was indicative of a phase transformation[73]. In cases such as this, indentation can cause a pressure-induced phase transformation, and the different density of this new phase can cause a sudden change in the volume of the material in that area, resulting in a change in displacement of the indenter in the material surface. In other cases, such as a case of indentation in a ZnO thin film[74], pop-outs can occur as the result of lateral fracture formation during unloading.

1.4.4 Orientation Effects in Nanoindentation

It is known that molecular crystals can tend to be quite anisotropic[75,76]. Because nanoindentation probes a very small localized area, anisotropic property variation throughout the sample is generally not accounted for with a single indentation. To account for this, typically many measurements are taken on various crystallographic faces of a sample, and in different areas of that face if the crystal is sufficiently large. There can be significant variation in hardness and modulus between different crystallographic planes, which has been well-documented via indentation[17,18,33].

Vlassak and Nix explored orientation effects using both isotropic and anisotropic materials, as well as with axisymmetric and non-axisymmetric indenter tips, in 1994. Their experiments were performed on crystals with either cubic or hexagonal symmetries with varying degrees of anisotropy: tungsten, aluminum, copper, β-brass, and zinc. The indenter tips used were both flat-punch geometries, one circular (axisymmetric) and the other triangular (non-axisymmetric). For the axisymmetric punch, they calculated indentation modulus M (previously defined here as E_r) as shown in Equation 1.14

$$M = \frac{P\sqrt{\pi}}{2d\sqrt{A}} \tag{1.14}$$

M with the non-axisymmetric punch, then, was found to be as shown in Equation 1.15

$$M = 1.058\frac{E}{1-\nu^2} \tag{1.15}$$

meaning that M is measured to be 5.8% higher with a non-axisymmetric punch than with an axisymmetric punch.

In addition to this slight variation in indentation modulus between different probe geometries, they also found a slight cyclic variation in indentation modulus with rotation angle within a single crystallographic plane for some faces with the triangular indenter. Both of these effects, of both orientation and indenter probe symmetry, were found to vary less than normal experimental scatter and therefore were determined to be negligible.

Later, orientation and radius effects were studied by Lawrence[77] et al. for their impact on plastic yield, which is described earlier within this chapter. In this study, a nickel sample was assessed via nanoindentation of differently oriented grains in the (001), (111), and (101) planes. Maximum pressure, p_0, at the time pop-in occurred was calculated with Equation 1.16

$$p_0 = \left[\frac{6PE_r{}^2}{\pi^3 R^2}\right]^{\frac{1}{3}} \tag{1.16}$$

where R is indenter radius. When p_0 at yield was compared as a function of grain orientation, there was a clear separation, with the (001) orientation consistently exhibiting a higher yield point than all others and the (001-111) boundary region consistently exhibiting a lower yield

point than all others. However, as this procedure was repeated with indenters of varying radii ranging from 100 nm to 1300 nm, this separation became less clear as tip radius decreased; that is, blunter indenter tips displayed this discrepancy between grain orientations, whereas sharper tips did not. This is to say, that the impact of tip sharpness can in some cases be greater than the impact of grain orientation on yield point, likely due to the probability of a tip and its stress field interacting with dislocations in the material.

While these indentation orientation effects have been studied extensively in metals, molecular crystals have received less attention. It was previously mentioned that anisotropy between different crystallographic planes of RDX and sucrose were characterized via nanoindentation, with up to 30% difference between orientations. Variation among different directions within a single crystallographic plane has also received little attention. In-plane orientation variation with a radially non-uniform indenter probe has been studied in aspirin by Taw et al.[19]. Aspirin, a monoclinic molecular crystal, showed negligible differences in its in-plane orientation testing results. This has also been studied in griseofulvin, a tetragonal molecular crystal, by Maughan et al. with both elastic and elastic-plastic loading[78], again showing negligible differences within a single plane. While these results so far are consistent with one another, with so few studies devoted to exploring indentation orientation effects in molecular crystals, this is hardly comprehensive. In-plane orientation effects in brittle, anisotropic molecular crystals are currently unknown for various crystal lattices, as well as for conditions besides low-load quasistatic indentation with pyramidal probes.

2. MATERIALS AND METHODS

This chapter describes the materials chosen for study and the criteria for their selection, and gives detailed technical procedures for both sample preparation and nanoindentation experiments. The procedures described here were performed at Purdue University and at the Center for Integrated Nanotechnologies (CINT) at Los Alamos National Laboratory (LANL). Materials tested range from pharmaceuticals to food products to explosives, and the primary experimental technique was nanoindentation.

2.1 Materials

Three materials were chosen as potential mock candidates for HMX: 5-iodo-2'-deoxyuridine (idoxuridine, IDOX), 2,3,4,5,6-pentafluorobenzamide (PFBA), and N,N'-bis(2,3,4,5,6-pentafluorophenyl)oxamide (N-BPFPO). Five materials were chosen as potential mock candidates for PETN: meso-erythritol (erythritol), PFBA, 2,4,6-trifluorobenzoic acid (246 TFBA), 1,1,1,5,5,5-hexafluoropentane-2,2,4,4-tetraol (HFPT), and (N-BPFPO). These materials span much of the breadth of molecular crystal applications; for example, HMX and PETN are explosives, IDOX is a pharmaceutical, an antiviral medicine, 246 TFBA is a pharmaceutical as well, and erythritol is a zero-calorie sweetener.

These materials were chosen by using the Cambridge Structural Database[79] to search for organic materials that fall within a certain density range. Materials returned by the search were then systematically eliminated for reasons such as being explosive or being liquid at room temperature. When a solid crystalline inert material was found to have an acceptable density and crystal structure (listed in Table 2.1 for the relevant materials), the next criteria was that the material be commercially available. Materials that passed this threshold were purchased in small amounts (typically 1-10 gram quantities) and analytical tests were done to determine thermal stability: differential scanning calorimetry and vacuum thermal stability testing. Materials that proved to have thermal stability comparable to their respective explosive were then crystallized and subjected to mechanical testing, both of which will be described later in this chapter.

Table 2.1 *Physical property values used as initial mock selection criteria, for PETN and each of the materials initially under consideration as mechanical mocks for PETN.*

Material	**Density (g/cm^3)**	**Crystal Structure**
HMX	1.902	Monoclinic
PETN	1.778	Tetragonal
IDOX	2.001	Triclinic
246 TFBA	1.759	Monoclinic
PFBA	1.884	Monoclinic
HFPT	1.941	Monoclinic
N-BPFPO	1.932	Monoclinic
Erythritol	1.45	Tetragonal

As previously mentioned and seen in Table 2.1, one of the selection criteria was crystal structure. It is commonly known that molecular crystals tend to be quite anisotropic, but some are less symmetric than others. The crystal structures relevant to this study are, in order of decreasing symmetry: tetragonal, monoclinic, and triclinic. A tetragonal unit cell is a rectangular prism with square bases; all angles are 90° and side lengths have the relationship $a=b\neq c$. A monoclinic crystal unit cell is also a rectangular prism extending from the base at a 90° angle, but with a parallelogram as the base, thus with three unequal internal angles. Finally, a triclinic unit cell is a prism extending up from the base at an angle $\alpha\neq 90°$ with a parallelogram as the base. All three of these can be seen in Figure 2.1[80].

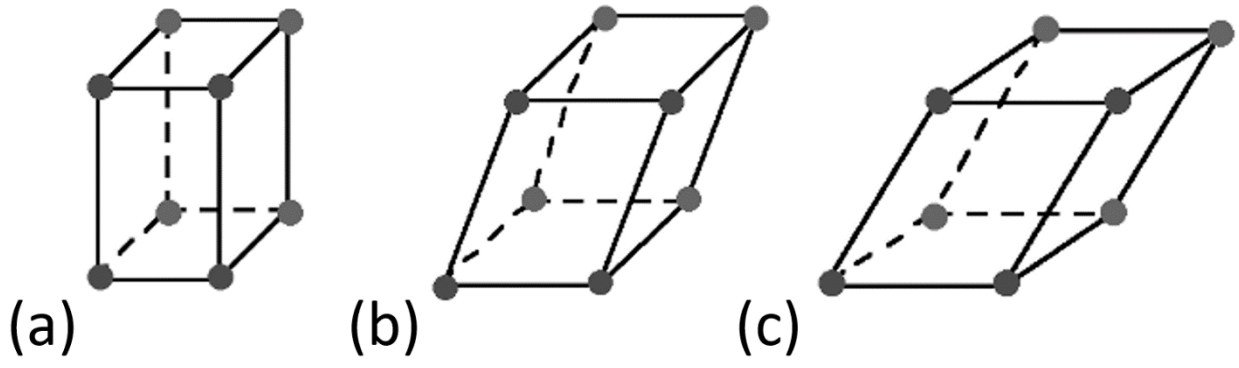

Figure 2.1 *Representations[80] of crystal unit cells in order of decreasing symmetry: (a) tetragonal, (b) monoclinic, and (c) triclinic*

Upon receipt of the materials used in this study, crystallization was required due to the fact that materials arrived in powder form. Solubility testing was done to determine an appropriate solvent for each material, and once a solvent was selected, a somewhat arbitrary amount of material was dissolved in a somewhat arbitrary amount of solvent, with ratios fine-tuned by trial and error. Many of the crystallization containers were covered with a perforated film in order to slow evaporation and thus crystallization; as mentioned in Chapter 1, these types of materials are highly prone to defects, but slower crystallization can mitigate this effect. While most materials, such as IDOX, could be collected after the solvent had evaporated entirely, other materials such as erythritol were more sensitive and had to be removed from the solvent before complete evaporation in order to prevent an undesirable "stadium" morphology that will be described shortly.

HMX single crystals were crystallized in acetone from Class 1 HMX produced by Holston. IDOX was originally purchased from Chem-Impex International, Inc. and crystallized in water. Meso-erythritol (Erythritol) was purchased from Sigma-Aldrich (now Millipore Sigma) and crystals were grown from a water solution. Pentafluorobenzamide (PFBA) was purchased from Alfa Aesar and crystallized from dichloromethane solution. 1,1,1,5,5,5-hexafluoropentane-2,2,4,4-tetraol (HFPT) was purchased from (SynQuest Laboratories, Alachua, FL). 2,4,6-trifluorobenzoic acid (246 TFBA) was purchased from TCI America and crystallized from acetone. N-BPFPO was synthesized using literature methods[81], reacting pentafluoroaniline (Sigma-Aldrich) with oxalyl chloride (Acros Organics) in benzene. The mixture was concentrated under vacuum and recrystallized in a 1:1 solution of ethyl acetate:hexanes. Fine crystalline powder was recovered, and larger crystals suitable for nanoindentation were produced by slow recrystallization from an acetone solution. PETN was synthesized at and provided by Purdue University and single crystals were crystallized in isopropyl alcohol. Figure 2.2 shows optical micrographs of the indentation surface of the eight materials, and Figure 2.3 shows their molecular structures.

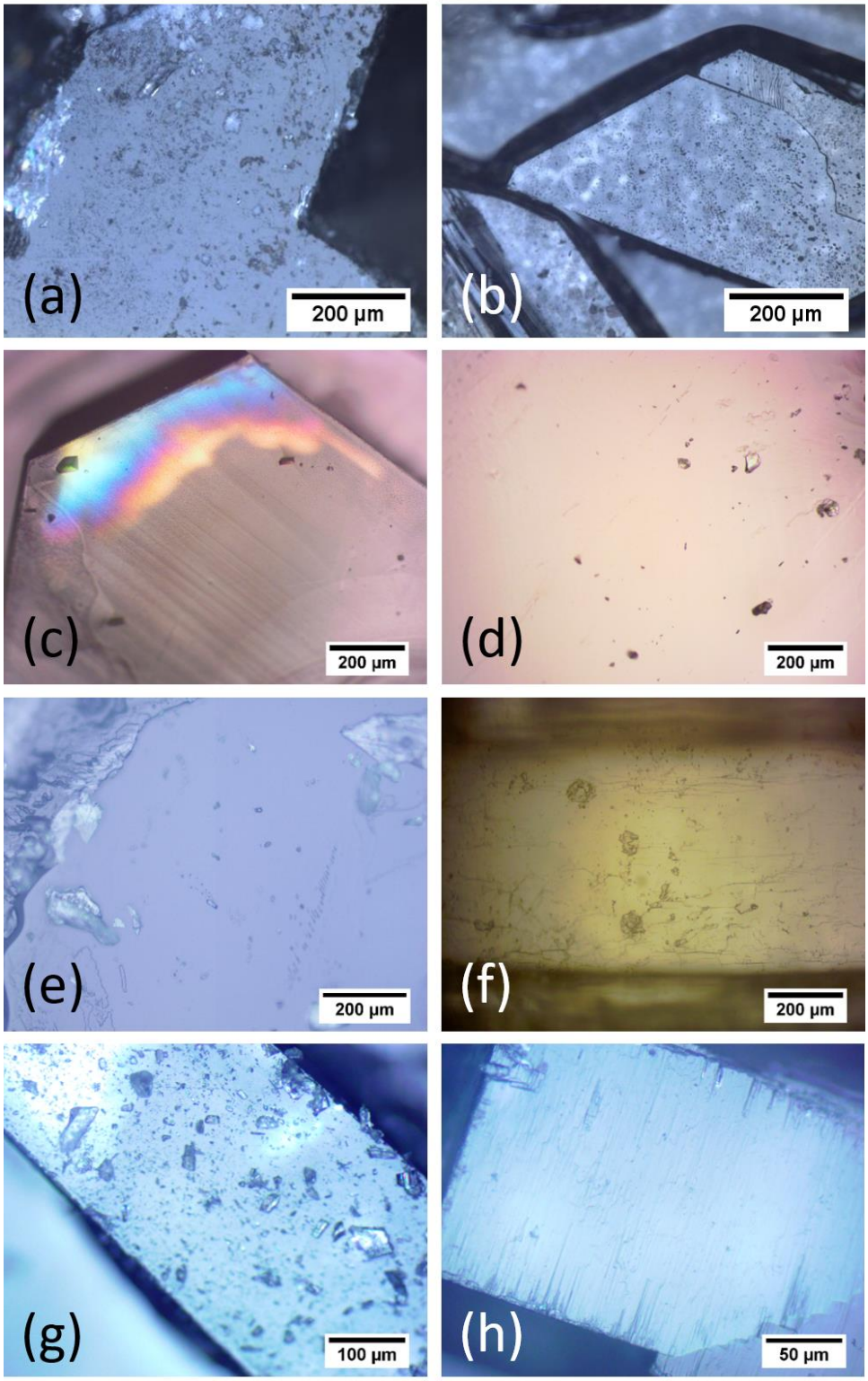

Figure 2.2 *Optical micrographs of single crystals of (a) HMX, (b) IDOX, (c) PETN, (d) erythritol, (e) 246 TFBA, (f) HFPT, (g) N-BPFPO, and (h) PFBA.*

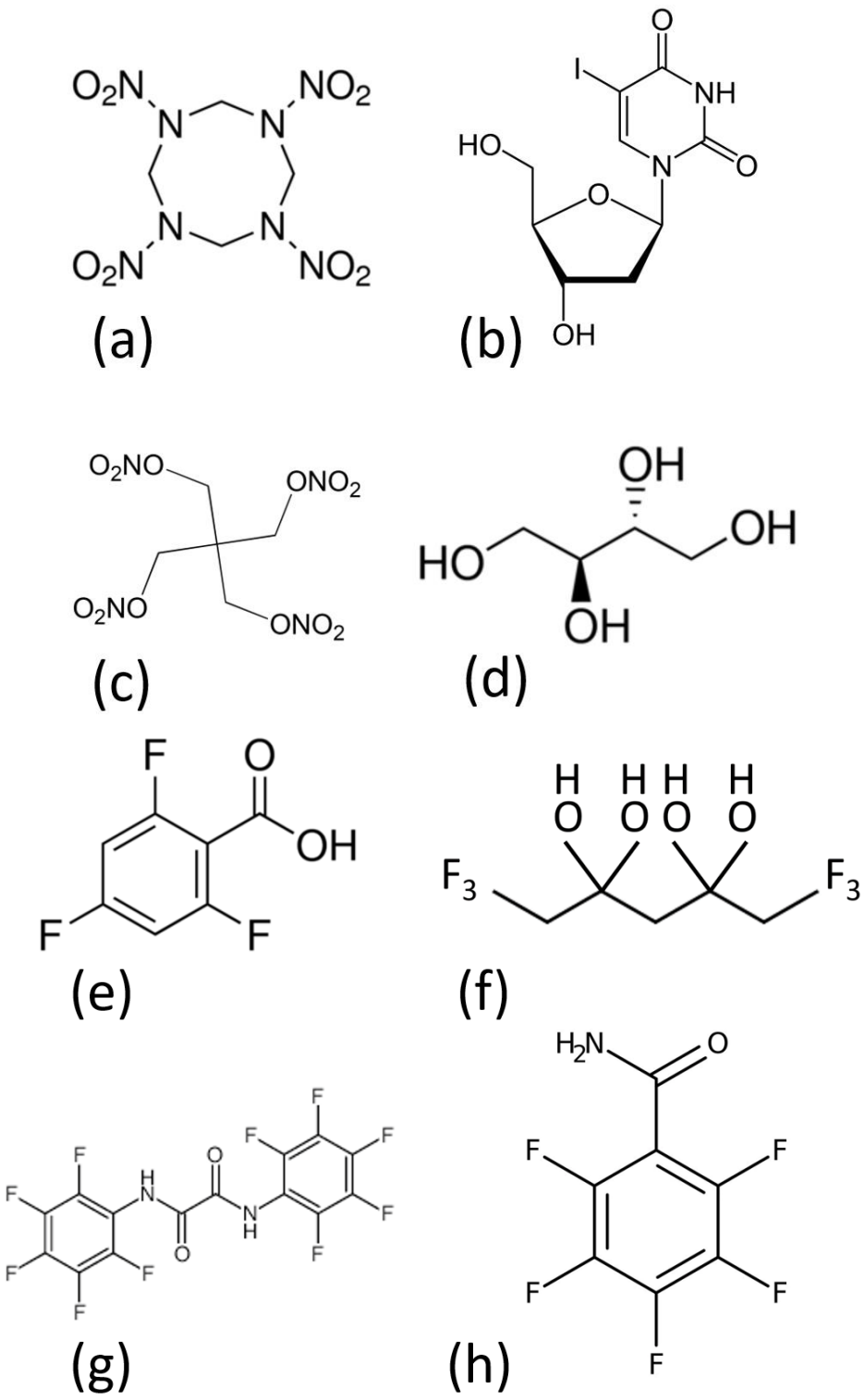

Figure 2.3 *Molecular structures of (a) HMX, (b) IDOX, (c) PETN, (d) erythritol, (e) 246 TFBA, (f) HFPT, (g) N-BPFPO, and (h) PFBA.*

2.2 Sample Preparation

As discussed in Chapter 1, it is crucial that nanoindentation samples have minimal surface roughness and a level surface. On many materials, such as metals, a smooth and level surface can be achieved by polishing, although this type of mechanical surface abrasion may cause alter the material surface sufficiently to affect indentation results [51]. Other materials, such as the organic molecular crystals previously discussed, may not lend themselves to mechanical resurfacing with techniques such as polishing, whether due to extremely limited particle size, solubility in polishing medium, or other limiting factors. This limitation was overcome by two methods, the first being careful crystallization. Because a flat surface cannot easily be polished or machined on these materials, it must be grown. As previously discussed, this growth could be controlled by slowing the evaporation rate of the solvent, controlling the solute-solvent ratio, and removing the crystal from the solvent at the appropriate time. An example of the result of incorrect technique is an erythritol "stadium" crystal. When removed from its solvent (water) before complete evaporation, erythritol often has extremely smooth and level surfaces, as can be seen in Figure 2.4(a) in which the topmost surface is brilliantly reflecting incident light. This surface is the ideal for molecular crystal indentation, and is the type of surface that is striven for. However, when the solvent is allowed to evaporate completely before erythritol crystals are collected, the resulting crystal is composed of concentric rings with innermost layers lying below outermost layers, with a gradual progression between; the structure resembles a stadium, thus the name. An example of this can be seen in Figure 2.4(b).

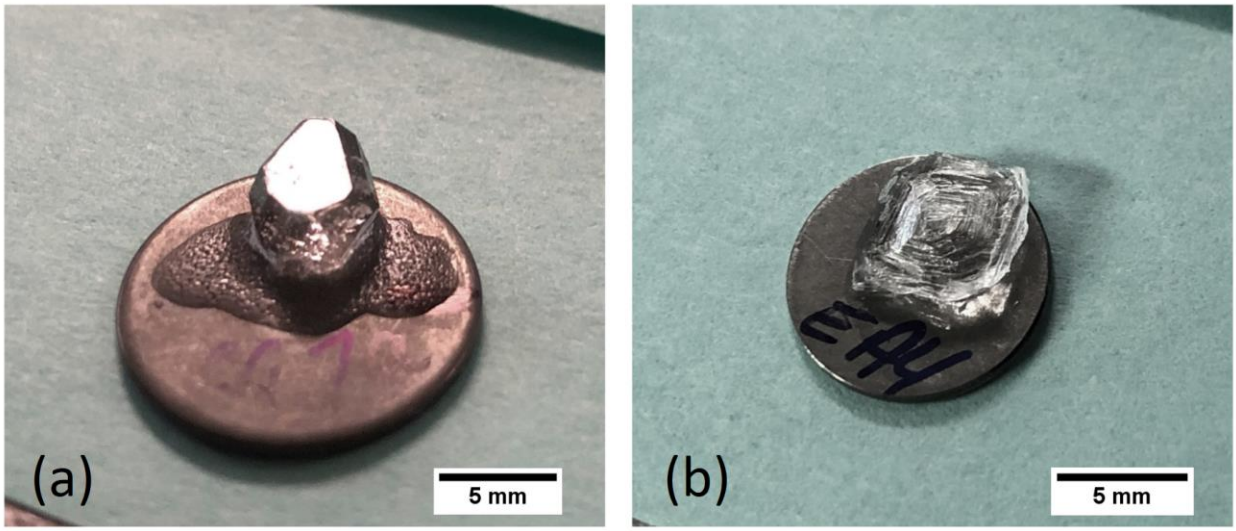

Figure 2.4 *(a) a smooth and level erythritol surface, and (b) an erythritol crystal with a "stadium" surface*

The second method of overcoming the limitation of requiring a flat and level surface without mechanical resurfacing is a mounting technique, developed by Maughan et al. [78]. With this method, depicted in Figure 2.5, a flat face of the crystal (achieved as previously described) is placed in direct contact with a level block, an orientation that will occur naturally via gravity. The crystal is then adhered to a mounting element, in this case adhered to a 15 mm steel AFM disc with the adhesive Crystalbond 555. This is done from above in such a way that when the mount is inverted, the surface of the crystal was the flat face that had previously rested on the aluminum block and was therefore parallel to the AFM disc and normal to the indenter probe.

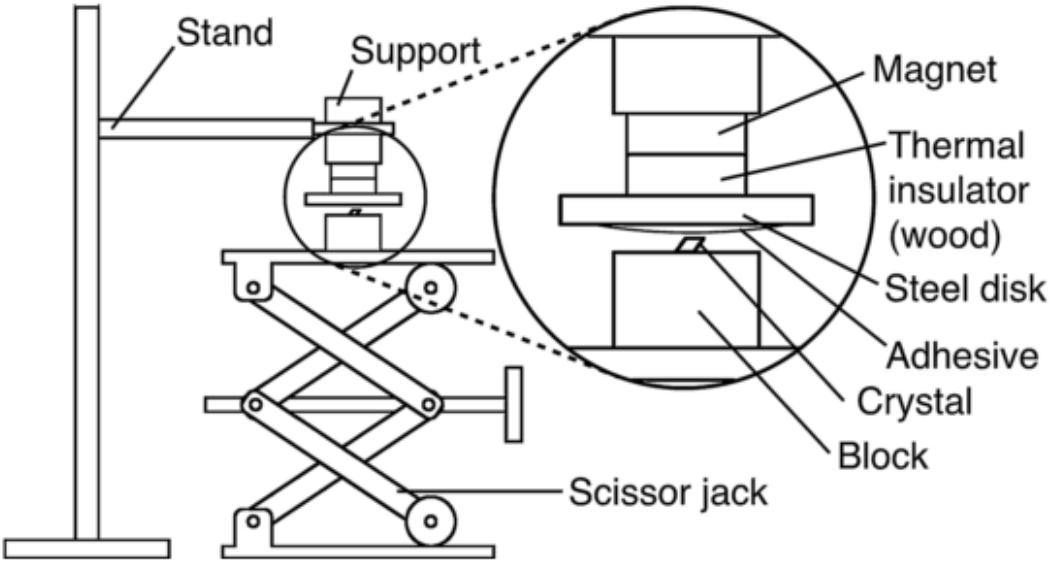

Figure 2.5 *The apparatus depicted by Maughan et al. for preparing small crystals for indentation with a level indentation surface that will be perpendicular to the indenter probe* [78].

Once crystals were mounted by this technique, it was necessary to confirm that the uppermost surface achieved was, in fact, smooth and level. As a broad screening technique, this was first determined via optical microscopy; surfaces that were quite obviously too rough for indentation could be spotted quickly, and surfaces that were extremely tilted could be identified by an inability to focus the aperture on the entire surface at once. If samples passed this optical inspection, then a more detailed inspection was done with scanning probe microscopy (SPM), a surface-rastering technique that is quite similar to atomic force microscopy (AFM). This scanning, which provides both a topographical image as well as a gradient image that indicates relative slope, gives a detailed view of both surface roughness as well as extent of surface tilt. If the SPM scan appears smooth (surface roughness below approximately 10% of intended indentation depth) and level (below approximately 5° tilt), then the sample is considered to be suitable for indentation.

2.3 Nanoindentation

2.3.1 General Nanoindentation Techniques

All nanoindentation was performed using the Hysitron Triboindenter 950. Indentation was performed in part at Purdue University and in part at the CINT facility at LANL, both facilities possessing a Hysitron Triboindenter 950. A total of three low-load Berkovich probes were used; one only at Purdue, one only at CINT, and one traveling between the two facilities. Two low-load cube corner probes were used; one only at Purdue, and one traveling between the two facilities. One conical probe was used, traveling between both facilities. Two each of high-load Berkovich and cube corner probes were used, one each only at Purdue and one each traveling between both facilities. Indenter probes were calibrated for area functions, as described in Chapter 1, using fused quartz samples. Two fused quartz samples were used, one at each facility. All indents were quasistatic open-loop with 30 s loading, 5 s hold, and 5 s unload times (with the exception of the two indents in 4.25); this loading profile was used in prior studies of RDX and some other organic molecular crystals[19]. To obtain reported hardness and elastic modulus values, 22 indents were performed on 10 HMX crystals, 19 indents were performed on 10 IDOX crystals, 112 indents were performed on 6 PETN crystals, 33 indents on 4 246 TFBA crystals, 26 indents on 4 PFBA crystals, 8 indents on 2 HFPT crystals, 19 indents on 3 N-BPFPO crystals, and 181 indents on 13 erythritol crystals. Some crystals were only indented once, while others were large enough to accommodate multiple indents; all indentations were spaced at least 10 times across the residual impression diameter to ensure the pristine material was being evaluated.

2.3.2 Indentation Fracture

For indentation fracture initiation, nanoindentation was performed with a high-load transducer for indentation loads above 12 mN and a standard transducer for indentation loads at and below 12 mN. Each material was indented at its respective load with both a Berkovich and cube corner indenter probe. As previously mentioned, three-sided pyramidal tips are chosen due to the ease of creating a sharp tip as the three planes necessarily meet at a point, however even with a three-sided pyramidal probe, sharpness is never perfect and so the tip has an effective radius[82]. With this in mind, the Berkovich and cube corner probes had radii of approximately 300

nm and 70 nm, respectively. Due to the limited size of the crystals (≈ 0.3 mm) not all indents are in the same crystals, but each complete pairing (Berkovich and cube corner) at a given load are within one single crystal. Single crystals of both HMX and IDOX were indented a minimum of six times each at each of the following maximum loads: 1 mN, 100 mN, 125 mN, 150 mN, 200 mN, 250 mN, and 300 mN. HMX single crystals were also indented a minimum of six times at each of the following maximum loads: 4 mN, 6 mN, 8 mN, 12 mN, 15 mN, and 25 mN. Single crystals of each of PETN, erythritol, and 246 TFBA were indented a minimum of six times each at each of the following loads: 0.5 mN, 1 mN, 3 mN, and 5 mN. PETN single crystals were also indented a minimum of six times at each of the following loads: 2 mN, 4 mN, 15 mN, 25 mN, and 50 mN. Erythritol single crystals were also indented a minimum of six times at each of the following loads: 10 mN, and 15 mN. Most indents were performed using quasistatic load-control mode with a 30 second load, 5 second hold, and 5 second unload. Two additional sets of indents on IDOX used a maximum load of 100 mN with 10 second loading time and a maximum load of 300 mN with the loading time extended to 90 seconds.

The unloading portions of the load-depth curves for both indents, one Berkovich and one cube corner per crystal, were plotted on the same graph with indentation depth h_f moved to the origin. This is done by taking the continuously measured load-depth data and first removing all loading and hold data. With only unloading data remaining, the value of h_f is subtracted from every depth (x-axis) data point. This moves the base of the curve to the origin. This is repeated for both the Berkovich and cube corner data, which are then plotted on the same axes. This process is shown in Figure 2.6.

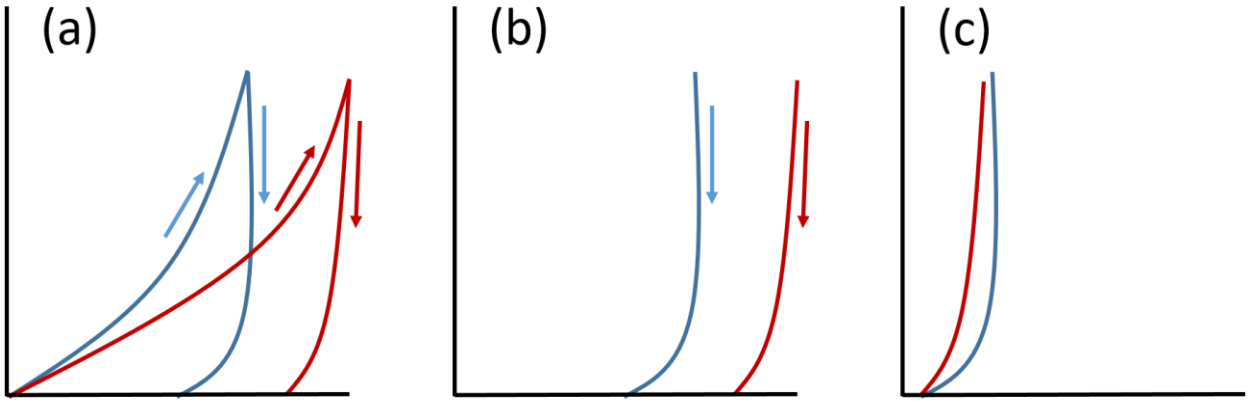

Figure 2.6 *A visual depiction of the steps of unloading analysis; (a) the load-depth curves of a material indented once each with two probes of significantly different acuity, (b) the loading portion of each curve is removed, and (c) the unloading portion of each curve is translated along the x-axis to the origin so that degree of superimposability can be easily seen*

With both curves located now at the origin of the same graph, degree of superimposability should be clear. If superimposability is still somewhat ambiguous, it can be helpful to further translate the curves along the x-axis to intersect with one another differently. Because of the way depth data was manipulated here, with curves translated along the x-axis to more easily observe superimposability, the position on the x-axis is somewhat arbitrary and can be adjusted as needed. Examples of unloading curves that have been translated along the x-axis can be seen in Chapter 1.4.3, Chapter 4, and in the appendix. This unloading superimposability was analyzed using the method described by Morris et al [70], which was discussed in detail in Chapter 1. To summarize, unloading curve pairs that were superimposable or nearly superimposable were considered to indicate that the material had not fractured as a result of indentation, and conversely unloading pairs that were *not* superimposable were considered to have fractured as a result of indentation. Indents were imaged using optical microscopy and scanning electron microscopy in order to observe the presence or lack of cracks emanating from these indents. This allowed determination of whether this unloading analysis technique correctly portrayed fracture results in these materials.

Fracture thresholds defined here are for indentation with cube corner indenters, which are sharp relative to other common indenter probes such as Berkovich. Because of this, any probe that is less sharp will likely result in a higher indentation fracture threshold.

2.3.3 Orientation-Specific Indentation

For orientation-specific indents, nanoindentation was performed with a low-load transducer to measure elastic modulus at 1 mN and with a high-load transducer to induce fracture at loads of 250, 300, and 350 mN.

For 1 mN indents, each sample was indented with both a Berkovich and a 120° conical probe, which had radii of approximately 70 nm and 540 nm respectively. For the conical probe, which is available in a variety of acuities, a 120° probe was chosen in order to apply force similarly to a Berkovich apart from geometry, as more acute probes have been found to deform materials in a different manner ("cutting" rather than "compressing") than broader probes[83–86]. On all samples, a single face of the crystal was chosen to be indented, and an arbitrary direction of that face chosen as the origin, labeled 0°. During the experiment, each crystal was rotated about a consistent normal direction relative to the arbitrary origin, and indented at 30° intervals with the previously indicated probe(s).The relative rotation angles were indicated by markings on the nanoindenter stage aligned with a marking on the sample mounting disc, similar to those depicted in Figure 2.7.

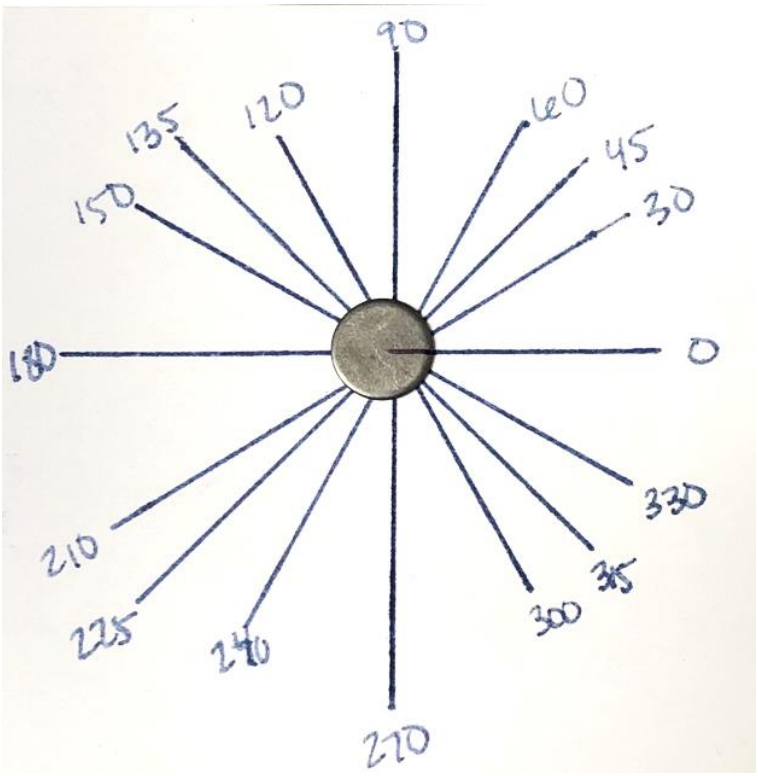

Figure 2.7 *A representation of how orientation-specific indentation angles were measured, with the angles indicated on the indenter stage and a reference direction marked on the sample mounting disc.*

For 250 mN, 300 mN, and 350 mN indents, one single crystal of IDOX was indented in 8 locations, as shown in Figure 2.8, with a cube corner probe at loads high enough to induce fracture. The sample was periodically rotated such that 3 different in-plane indenter orientations were sampled, and fracture development and direction were recorded following each indent. Figure 2.8 shows the crystal with 8 fractured indents and a diagram labelling how each indent is identified, and Table 2.2 lists the indenter angle and applied load for each indent. Particular care was not taken in spacing indents far enough to prevent interaction, as quantitative indentation measurements were not being taken, and with fracture often extreme enough to cleave the crystal, indent interactions were somewhat unavoidable while still keeping all indents on one single crystal.

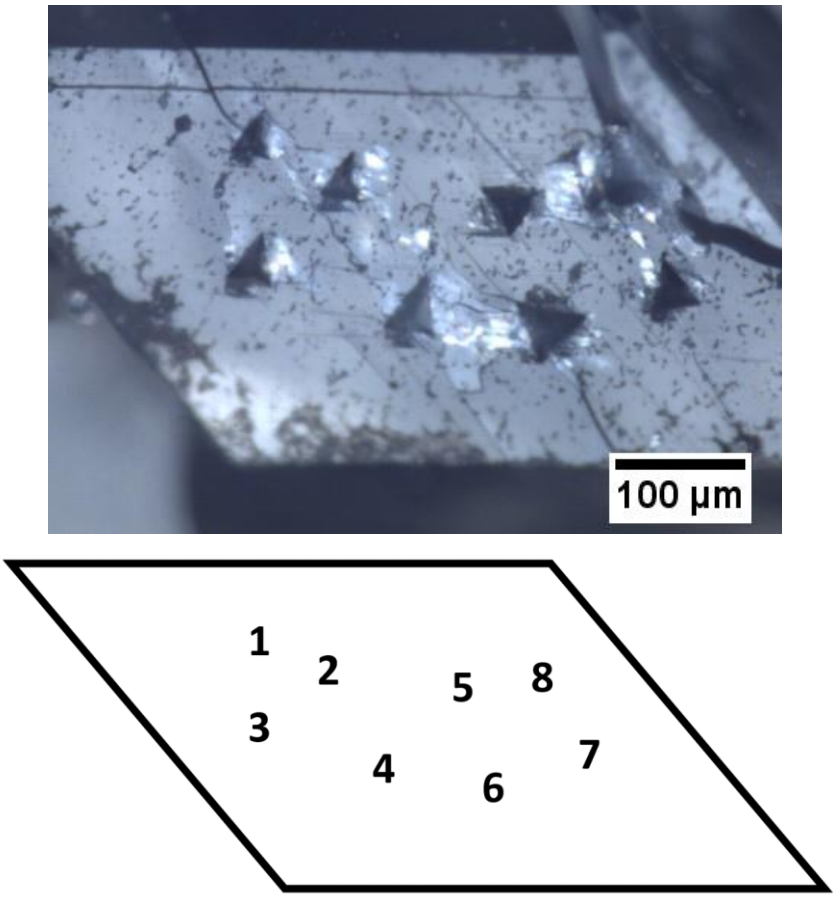

Figure 2.8 *Location of orientation fracture indents in an IDOX single crystal*

Table 2.2 *Applied load for orientation fracture indents*

Indent	Load (mN)	Relative Angle (°)
1	225	0
2	250	0
3	300	0
4	350	0
5	350	60
6	300	60
7	300	105
8	350	105

3. ELASTIC AND PLASTIC PROPERTIES MEASUREMENTS: QUASISTATIC MECHANICAL MOCK IDENTIFICATION

Portions of this chapter have previously been published in Crystals (Nanoindentation of HMX and Idoxuridine to Determine Mechanical Similarity. A Burch, J Yeager, D Bahr. Crystals, Vol 7, Issue 11, pp.335(1:9). doi: 10.3390/cryst7110335. 2017); (A Thermal and Nanomechanical Study of Molecular Crystals as Versatile Mocks for Pentaerythritol Tetranitrate. A Burch, Z Wilde, D Bahr, J Yeager. Crystals, Vol 10, Issue 2, pp.126(1:15). doi: 10.3390/CRYST10020126. 2020)

3.1 Introduction

As discussed in Chapter 1, nanoindentation techniques have previously been employed in the characterization of both energetic and inert molecular crystals, as well as in efforts to determine suitability of certain inert molecular crystals to mock various explosives[18,20,39,87]. Nanoindentation is chosen for this in part due to its ability to apply appropriate micro-scale tests to materials such as those tested here, which are μm to mm in scale, as well as its ability to probe a variety of properties with a single test.

Nanoindentation was described in great detail in Chapter 1 and will be summarized here. "Nanoindentation" describes an instrumented test in which a load is applied to a material surface via a small tip, tens to hundreds of nm in radius, and both the applied load and displacement into the surface are measured continuously. This data is reported as a load-depth curve with load on the y-axis and depth on the x-axis. The portion of this curve that reflects how the material responded as the load was applied is assumed to be influenced by both elastic and plastic deformation, which allows information to be drawn regarding the yield point where plastic deformation begins, shear stress, and hardness. The unloading portion of the load-depth curve is assumed to be fully elastic, so the slope (which is the material stiffness) can be used to determine elastic modulus.

This chapter assesses the suitability of using IDOX, PFBA, and N-BPFPO to serve as surrogates for the mechanical response of HMX, and of using erythritol, 246 TFBA, PFBA, HFPT, and N-BPFPO to serve as surrogates for PETN. This assessment is done using nanoindentation on single crystals to assess hardness, elastic modulus, and yield behavior. This

assessment is used to determine which materials warrant further consideration as potential mock materials and which do not.

3.2 Results and Discussion

3.2.1 Hardness and Modulus Measurements

Hardness and elastic modulus measurements were taken using a Berkovich indenter probe at 1000 μN in all materials; examples of typical load-displacement data are shown in Figure 3.1.

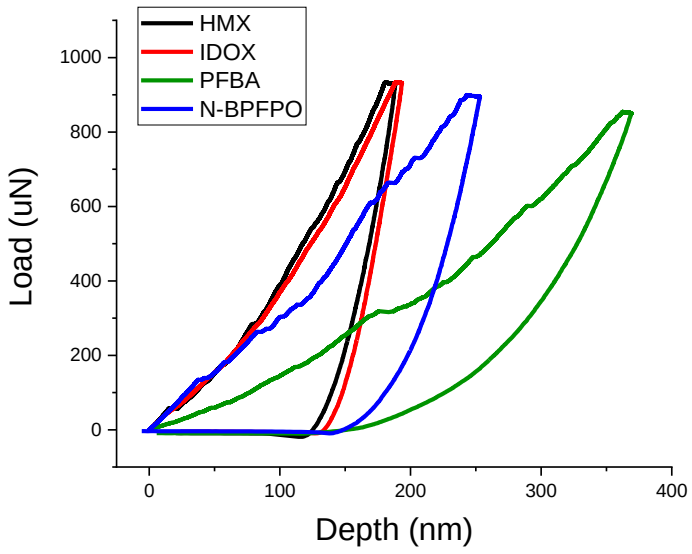

(a)

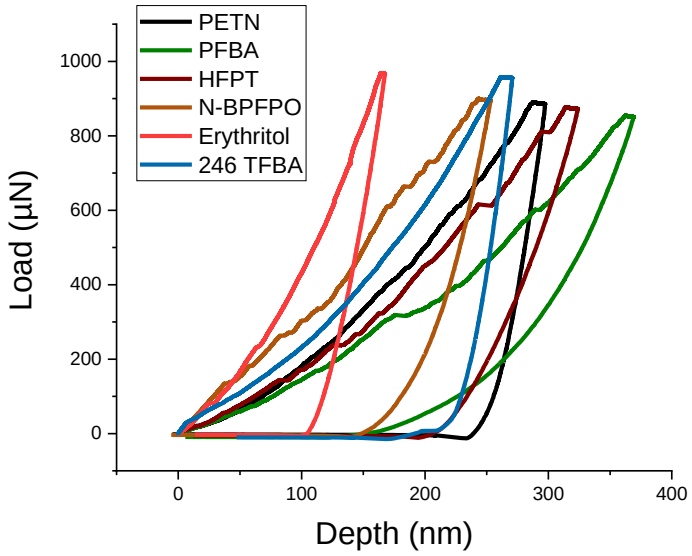

(b)

Figure 3.1 *(a) Typical load-depth curves for HMX and each of its prospective mocks, IDOX, PFBA, and N-BPFPO, with indentations in one random crystal of each material shown. (b) Typical load-depth curves for PETN and each of its prospective mocks, PFBA, HFPT, N-BPFPO, erythritol, and 246 TFBA, with indentations in one random crystal of each material shown*

Load-depth data from several such indents per material were analyzed using the method described by Oliver and Pharr[40] to obtain elastic modulus and hardness values, averages for which are reported for each material in Table 3.1.

Table 3.1 *Average values for elastic modulus and hardness, as measured via nanoindentation, for PETN, HMX, and each of the materials initially under consideration as mechanical mocks for PETN and HMX. Sample size information is available in Chapter 2.3.1.*

Mock material mechanical property comparisons		
Material	**Elastic Modulus (GPa)**	**Hardness (GPa)**
HMX	25.2 ± 2.1	1.00 ± 0.11
PETN	15.2 ± 2.4	0.45 ± 0.08
IDOX	23.3 ± 2.2	1.00 ± 0.15
246 TFBA	19.2 ± 2.6	0.54 ± 0.18
PFBA	5.8 ± 1.5	0.24 ± 0.03
HFPT	6.3 ± 0.4	0.33 ± 0.07
N-BPFPO	17.6 ± 0.4	0.44 ± 0.07
Erythritol	21.2 ± 2.4	1.22 ± 0.13

As a consequence of the results shown in Table 3.1, PFBA and N-BPFPO were found to be too dissimilar to HMX, with 76% and 56% difference in hardness respectively, and 77% and 30% difference in elastic modulus respectively. Following this result, these two materials were no longer considered as potential mechanical mocks for HMX. IDOX, however, emerged as a highly promising candidate, with 7.5% difference in elastic modulus and 0% difference in hardness. From this point, only IDOX was considered as a potential mechanical mock for HMX.

The indentation data presented in Table 3.1 for PETN and several of its mocks were collected during the same time period as DSC testing was being performed on the same materials by Dr. John Yeager at Los Alamos National Laboratory, and therefore narrowing the pool of PETN candidates at this point was done with consideration to both data sets. Dr. Yeager's DSC results are shown in Figure 3.2.

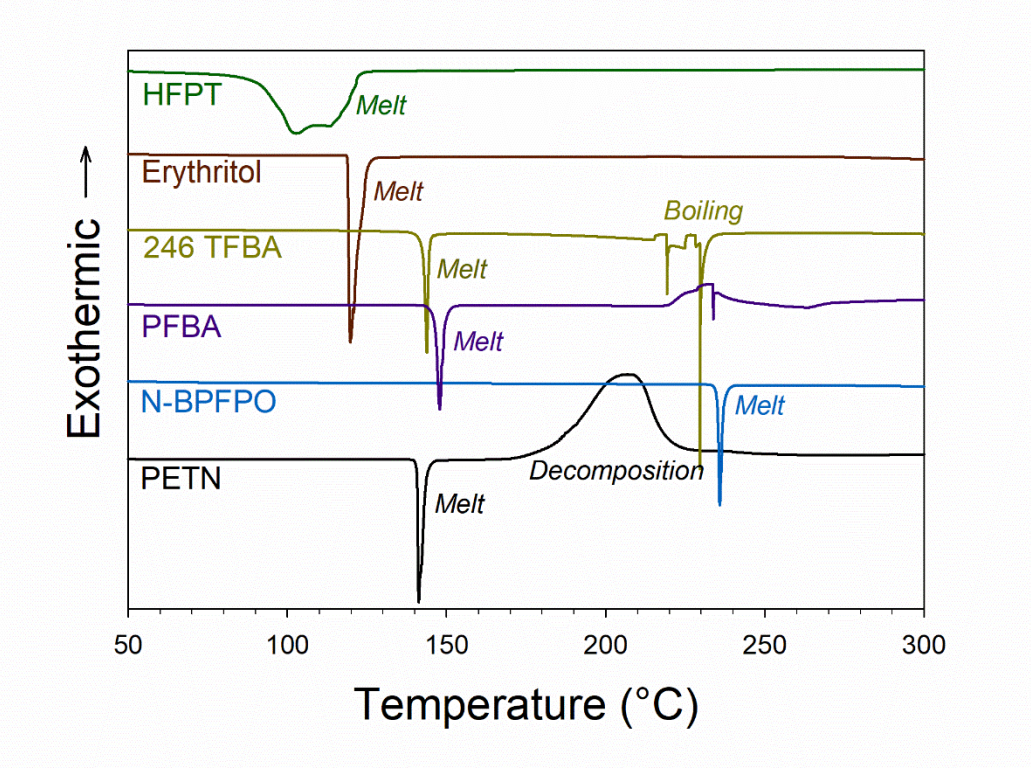

Figure 3.2 *DSC data for PETN and its initial mock candidates. Polymorphic behavior was not indicated for any of these materials.*

As a consequence of these results shown in Table 3.1 and Figure 3.2, only two materials were selected to continue as potential mechanical mocks for PETN. HFPT had a 59% difference in modulus from PETN and had too low of a melting point, and PFBA had a 62% difference in modulus and a 47% difference in hardness; therefore, HFPT and PFBA were no longer considered as potential mocks for PETN. N-BPFPO was mechanically quite similar to PETN, with 16% difference in elastic modulus and 2% difference in hardness; however, its melting point was significantly higher than PETN's, so it was no longer considered to be a viable thermomechanical mock. 246 TFBA was 26% different from PETN in elastic modulus and 20% different in hardness, and had a virtually identical melting point, and therefore was selected to continue in consideration as a potential PETN mock. Erythritol was mechanically quite different from PETN, with a 39% difference in elastic modulus and 171% difference in hardness; however, its melting point was rather similar to PETN's with about a 20°C difference, and erythritol was also remarkably affordable and easy to source and process, which are quite desirable attributes in a mock, so erythritol was also selected alongside 246 TFBA to continue as a potential PETN mock.

The distribution of the measurements shown in Table 3.1 for HMX and its most similar mock candidate IDOX are shown in Figure 3.3, and the distribution of these measurements for PETN and its mock candidates of most interest, 246 TFBA and erythritol, are shown in Figure 3.4.

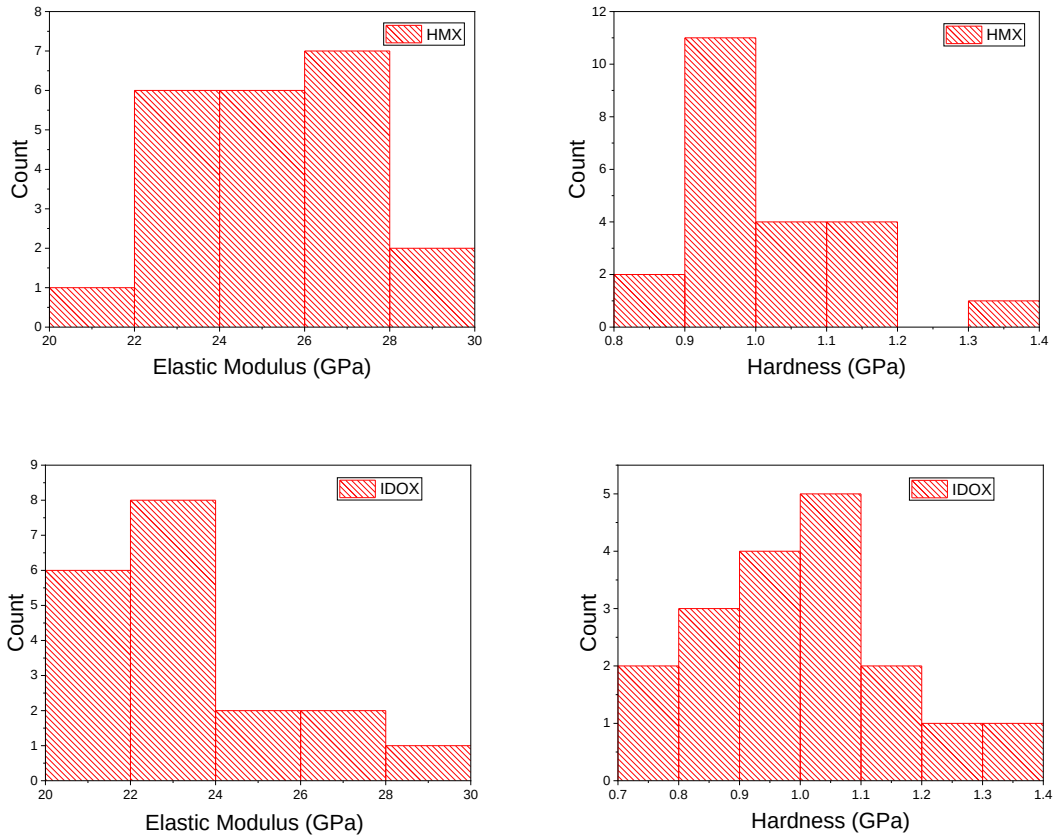

Figure 3.3 *(a) HMX reduced elastic modulus measurement distribution (b) HMX hardness measurement distribution (c) IDOX reduced elastic modulus measurement distribution (d) IDOX hardness measurement distribution*

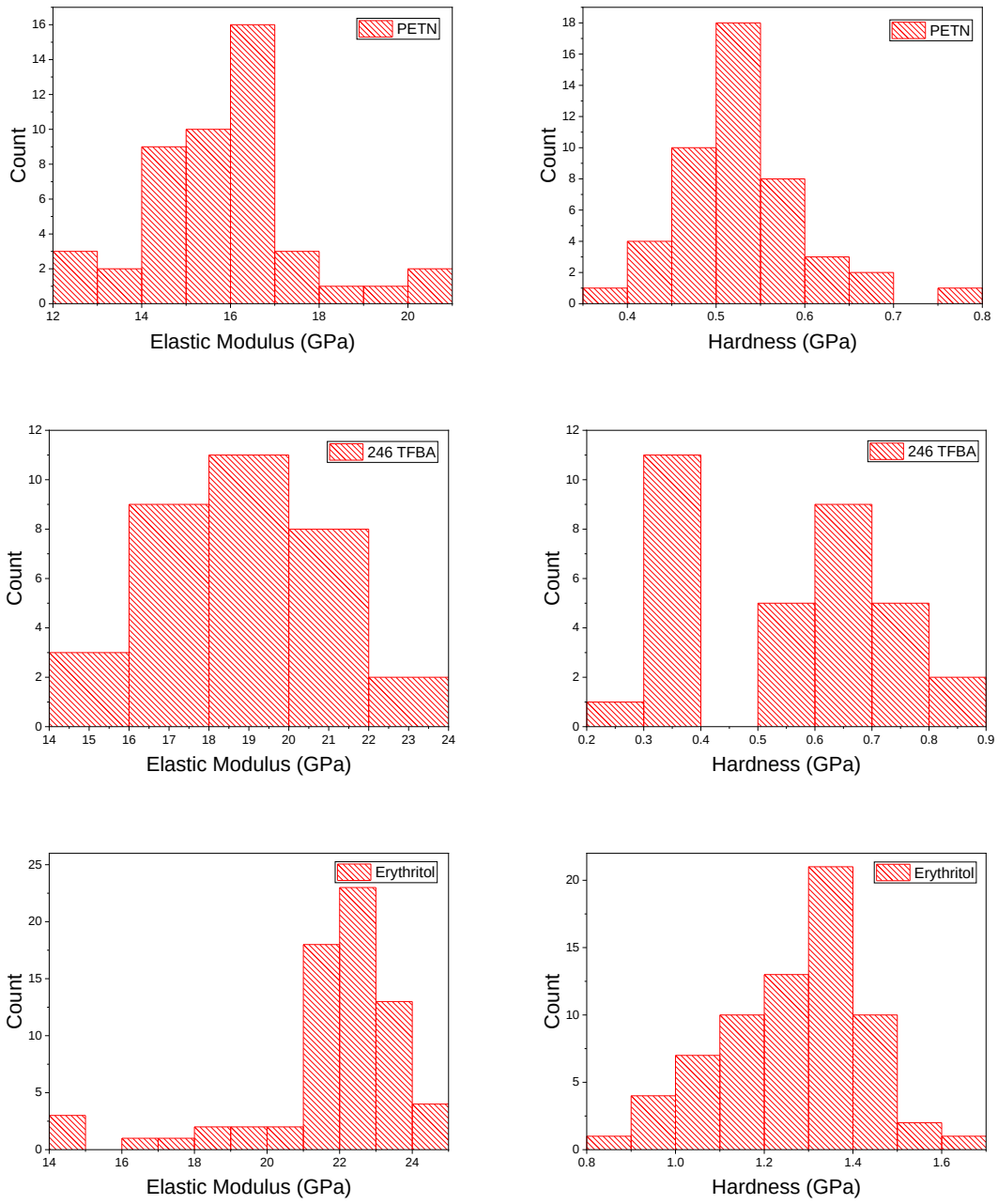

Figure 3.4 *(a) PETN reduced elastic modulus measurement distribution (b) PETN hardness measurement distribution (c) 246 TFBA reduced elastic modulus measurement distribution (d) 246 TFBA hardness measurement distribution (e) Erythritol reduced elastic modulus measurement distribution (f) Erythritol hardness measurement distribution*

These measurements can have quite a bit of stochastic variation for various reasons, such as dislocation density, size effects, and crystallographic orientation[88]. Oliver and Pharr showed that very precise indentation in isotropic materials with good technique can produce results within a 10% range[40], though that range may be wider for materials such as molecular crystals which are anisotropic and generally dissimilar to ideal models; elastic-plastic indentation of such materials has shown variation within 18%[78]. The distributions shown in Figures 3.3 and 3.4 then, while somewhat broad in range, are rather unremarkable for most materials shown, though there is an exception. The hardness of 246 TFBA exhibits a bimodal distribution, with a peak at 0.3-0.4 GPa and another peak at 0.6-0.7 GPa. This data was collected from 246 TFBA that was crystallized in two batches, indicated that there may be some batch-to-batch variation in hardness depending on crystallization conditions. However, this bimodal distribution is not reflected in reduced elastic modulus data for 246 TFBA. Different types of defects can have an uneven effect elastic modulus versus hardness; for example, elastic modulus can be affected by impurities or solutes, but would not be impacted by changes in dislocation density that would affect hardness.

Prior work published by Zhai et al.[89] on nanoindentation of PETN showed a dramatic depth dependence for elastic modulus of PETN, with values as high as 27 GPa at low depths, and a very sharp and consistent decline until a depth of approximately 200 nm where the modulus then levelled off to a consistent value of approximately 11 GPa, as seen in Figure 3.5(a). This is atypical behavior for molecular crystals; depth dependence is often seen in materials with surface films, oxide layers, or surface-level work hardening as a few examples, but properties such as elastic modulus do not tend to vary as a function of depth in molecular crystals. In an attempt to duplicate that result for this mock material study, PETN was indented at a similar range of depths and the elastic modulus was evaluated as a function of depth. This was then repeated 7 months after the initial measurements, and again 13 months after initial measurements. As can be seen in Figure 3.5(b), this depth dependence could not be replicated in any of the three data sets, and the elastic modulus measured, approximately 15 GPa, was notably higher than the 11 GPa prior data had leveled off to.

While no depth dependence was revealed, the elastic modulus of these PETN crystals did appear to decrease from month 0 to month 7, prompting additional assessment of the elastic modulus again at month 13 to observe if any changes were occurring due to the age of the material. While the elastic modulus of the newly synthesized material measured 18.2 ± 2.8 GPa,

the material at ages 7 months and 13 months appears to have settled around 15.0-15.8 GPa. Due to the behavior of the samples at larger depths at month 0 and the low indentation depths of typical nanoindentation tests, differences over time were also considered for only indents below 300 nm in depth. Considering only those indents below a depth of 300 nm had a minimal effect on the results, with the elastic modulus at month 0 measuring 18.4 ± 2.9 GPa, at month 7 measuring 15.1 ± 0.6 GPa, and at month 13 measuring 15.8 ± 1.8 GPa, unchanged due to the lack of higher-depth indents at month 13. Other studies on PETN powder have shown similar trends with properties such as surface area coarsening, where newly synthesized PETN initially coarsens at a very high rate but the rates soon become much more gradual, if not completely stable[90,91].

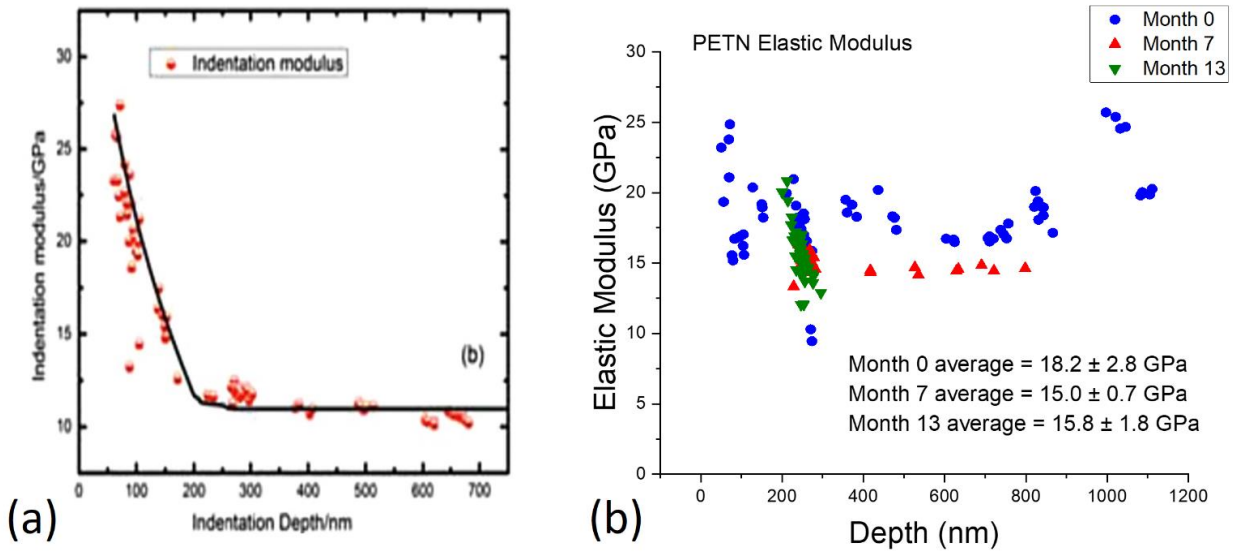

Figure 3.5 *(a) Prior nanoindentation results showing a strong depth dependence of elastic modulus in PETN[89](b) Elastic modulus of PETN as a function of depth with data collected during the course of the present study showing no depth dependence. Elastic modulus of the newly synthesized material (month 0) is higher than later measurements (month 7, month 13) but as the material ages the modulus appears to stabilize. This is consistent with observation of other properties of PETN as a function of time[90,91].*

3.2.2 Incipient Plasticity

As noted in Figure 3.6, many indentations exhibited a "pop-in" or "excursion" in the load depth curve. This is commonly considered to be indicative of the transition from elastic to plastic deformation[46,51,55,92–95].

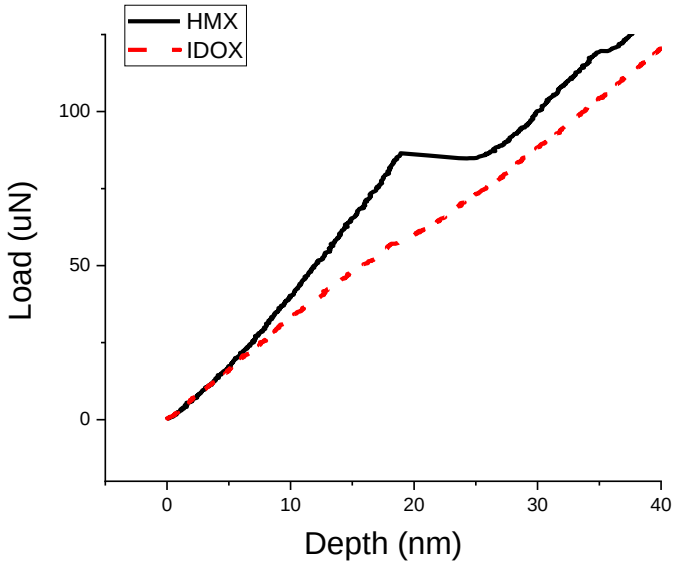

(a)

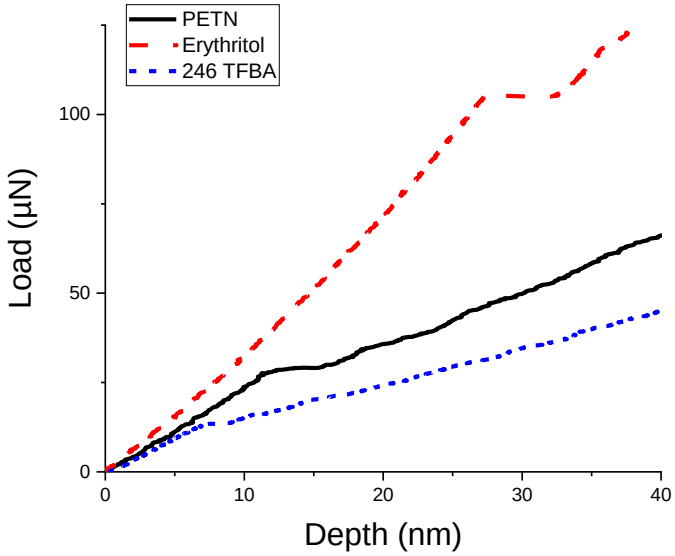

(b)

Figure 3.6 *(a) The same load-depth curves for HMX and IDOX as in Figure 3.1(a), showing only data below 125 μN (b) The same load-depth curves for PETN, erythritol and 246 TFBA as in Figure 3.1(b), showing only data below 125 μN*

Yield point behavior can be quantified by the load at yield (which is proportional to the maximum applied shear stress for materials with the same elastic modulus when a common tip with a fixed radius is used). Figure 3.7 shows the difference in the distribution of load at the first yield point for all indentations performed in this study. Using a cumulative distribution plot is a convenient way to determine if different defect densities or mechanisms are being probed [50], and the relative curvature and position are indicative of an activation energy to nucleate a dislocation when one compares the only the fraction that yielded (ignoring those that exhibit no yield point). In metallic systems, higher defect densities are linked to larger numbers of indentations that do not exhibit a yield point [94], and surface preparation can shift (in load) or "tilt" in probability the cumulative fraction plot in RDX [96].

In all indentations in HMX the indentation curve exhibited a yield point, while in the case of IDOX only half of the indents exhibited a yield point. The mean load at yield for indentations that did exhibit a yield point for IDOX was 98 μN and for HMX was 93 μN; the maximum load exhibited are also of a similar magnitude, as one might expect for materials with similar elastic modulus values. Finally, the median of the loads which caused yield are similar for these indentations, 78.5 μN for HMX and 62.8 μN for IDOX. This data can be seen in Figure 3.7(a). As discussed in Chapter 1.4.2, shear stress at yield can be calculated from the load at yield, the elastic modulus, and the tip radius, shown as Equation 3.1.

$$\tau = 0.31 \left(\frac{6\overline{E_r}^2}{\pi^3 R^2} \right)^{1/3} P^{1/3} \qquad 3.1$$

Using this equation, average shear strengths for HMX and IDOX are 1.47 GPa and 1.30 GPa, respectively. This data can be seen in Figure 3.7(b). The implication here is that while the average shear stress needed to nucleate dislocations in both materials is very similar, suggesting the nucleation phenomena is based on the same mechanism in both these samples, and the maximum shear stress is of the same order, based on the similarity of the maximum observed value in yield point, the likelihood of probing a mechanical defect (such as a pre-existing dislocation) is much higher in the IDOX than in the HMX for the forms of the materials tested in this study.

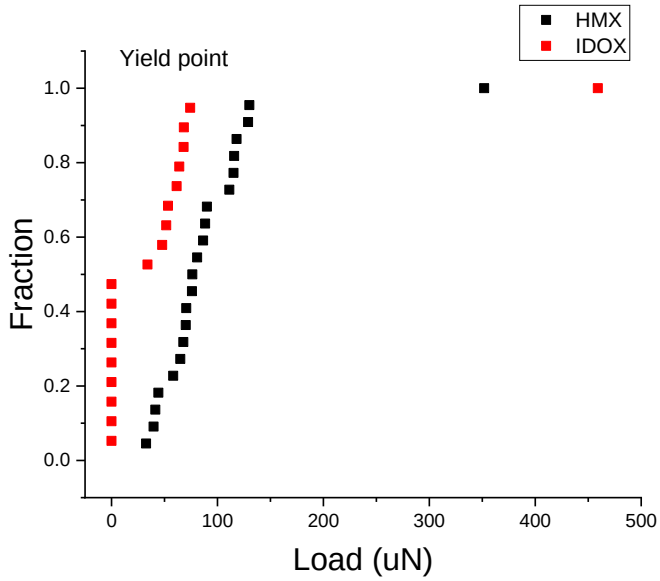

(a)

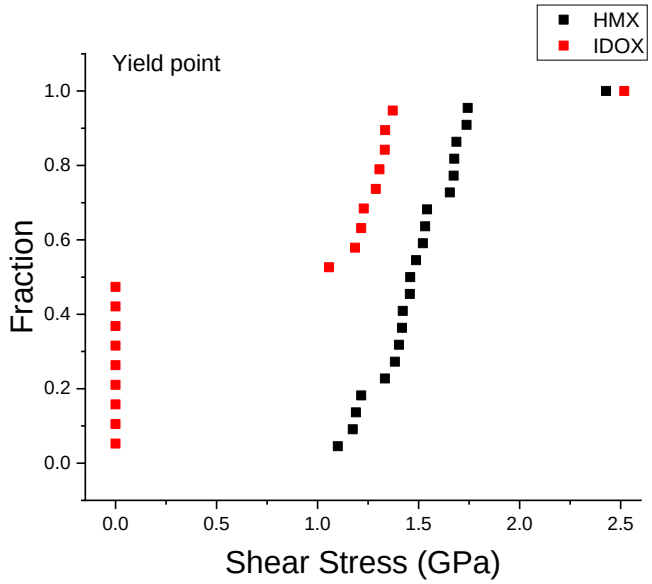

(b)

Figure 3.7 *Cumulative fraction of yield behavior for HMX and IDOX, (a) as a function of applied load, and (b) as a function of shear stress*

PETN and 246 TFBA each had a yield point in every load depth curve, and erythritol had a yield point in nearly every curve. In cases where a yield point was present, the mean load at yield was 175 µN for PETN, 140 µN for erythritol, and 15 µN for 246 TFBA. The median values of these ranges were 118 µN, 118 µN, and 13.5 µN respectively. This data can be seen in Figure

3.8(a). Equation 3.1 gives shear strengths for each material as 1.37 GPa, 1.59 GPa, and 0.71 GPa, respectively. This data can be seen in Figure 3.8(b). As indicated by these values, the yield behaviors for PETN and erythritol were similar in both magnitude and trend. The yield behavior of 246 TFBA however was quite different, with both a substantially lower yield threshold as well as an extremely narrow range, pointing to the possibility of a much higher defect density than what is expected in PETN and erythritol.

This type of yield point analysis and comparison can indicate the relative defect density in the material being probed, and the resistance to plastic deformation of each material; however, the impact of these differences are expected to be minimal given that typical processing loads for these materials far exceeds this minimum plasticity threshold; all materials tested yield at loads below 1 mN, and loads expected in regular processing such as pressing are generally a thousand times higher than this[97]. While indentation has a greater stress concentration at the pointed tip that is nanometers in radius, whereas in pressing the stresses are different due to the load being distributed over a much larger surface area, millimeters to centimeters in radius, pressing loads are still expected to produce larger stresses overall.

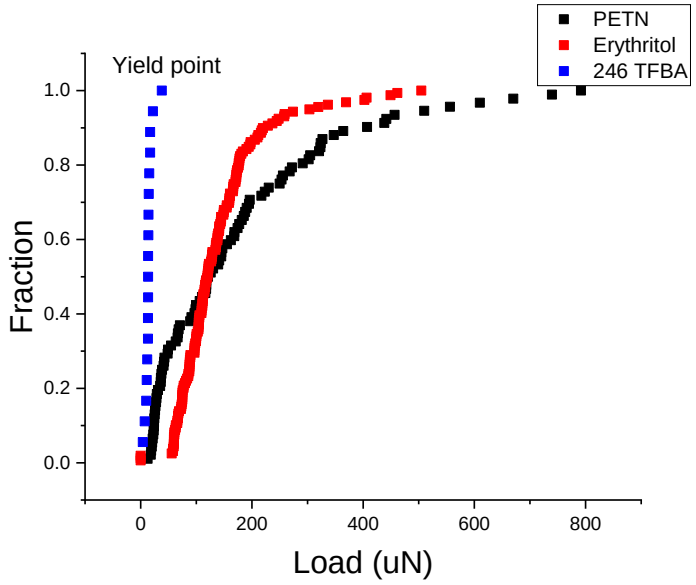

(a)

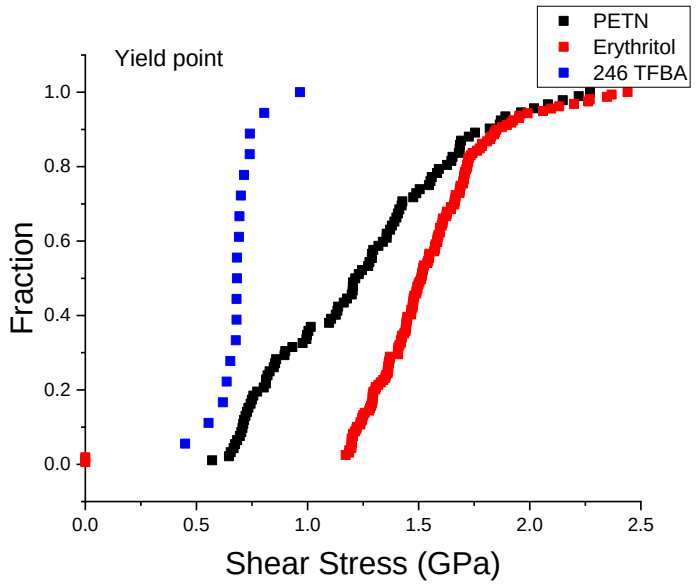

(b)

Figure 3.8 *Cumulative fraction of yield behavior for PETN, erythritol, and 246 TFBA, (a) as a function of applied load, and (b) as a function of shear stress*

3.3 Conclusions

As shown, it has been successfully determined that IDOX has similar elastic and plastic mechanical properties to HMX, which can be difficult to perform tests on due to safety concerns. The similarity in hardness and elastic modulus indicate that IDOX can be used to test the mechanical response of composite structures typically containing HMX. When yield behavior occurs in both materials, the loads (and therefore stresses) at which dislocations are nucleated appear to be similar. However, in the as-received state, it appears IDOX may have a higher mechanical defect density than the HMX (for powders of the same size).

Similarly, it has been successfully determined that 246 TFBA and erythritol have similar elastic and plastic mechanical properties to PETN, indicating that either material may be suitable to test the mechanical response of composite structures typically containing PETN. Hardness of 246 TFBA appears to be sensitive to crystallization conditions, so for cases in which hardness is of concern in mocking PETN, it may be necessary to closely monitor crystallization conditions. Yield behavior between PETN and erythritol is significantly more comparable than for 246 TFBA, though this is not expected to be relevant in typical processing.

4. INDENTATION FRACTURE MECHANICS IN MOLECULAR CRYSTALS

Portions of this chapter have previously been published in Journal of Materials Research (Indentation Fracture Behavior of Energetic and Inert Molecular Crystals. A Burch, J Yeager, D Bahr. JMR, Vol 34, Issue 23, p3954-3963. doi: 10.1557/jmr.2019.345. 2019. Reproduced with permission.) and in Crystals (A Thermal and Nanomechanical Study of Molecular Crystals as Versatile Mocks for Pentaerythritol Tetranitrate. A Burch, Z Wilde, D Bahr, J Yeager. Crystals, Vol 10, Issue 2, pp.126(1:15). doi: 10.3390/CRYST10020126. 2020)

4.1 Introduction

In the previous chapter, three materials were tested for their suitability to mock elastic and plastic mechanical properties of HMX, and similarly five materials were tested for their suitability to mock PETN. From this pool, potential mock candidates were narrowed down to one for HMX, IDOX, and two for PETN, 246 TFBA and erythritol. The indentation tests that were used to make these determinations were all under low-load quasistatic conditions; however, under normal operating parameters, explosive materials are often subjected to larger and more unpredictable forces.

As explained in detail in Chapter 1 and summarized here, indentation is a convenient technique for initiating fracture and drawing conclusions concerning fracture properties. Understanding of a material's indentation fracture behavior is helpful for two reasons: one being that it can reveal the toughness of the material in a quantifiable way, and the other being that nanoindentation that causes fracture cannot be used to measure things such as elastic modulus and hardness, so understanding how resistant a material is to fracture can determine the range of loads that can be used to characterize that material by indentation methods.

Indentation fracture occurs as the stress field formed when the indenter comes in contact with the sample concentrates locally at sharp contacts, and the material undergoes inelastic deformation in an effort to temper this stress concentration[56]. When a flaw is initiated in this way, crack propagation is then governed by the mechanical energy released by fracture versus the additional surface energy of the crack. When the mechanical energy release rate is more than double the fracture surface energy, the crack will propagate. When this condition has been met, cracks will propagate according to stress concentrations that existed prior to fracture, which can

be strongly influenced by material anisotropy. Indentation fracture toughness, the degree to which a material resists both fracture initiation and propagation, will be discussed in detail later in this chapter.

Initiation of fracture during a nanoindentation test is not necessarily indicated in a load-depth curve, so typical fracture detection is done by optical inspection. This technique can be difficult, for example in an opaque material with subsurface cracks, or in indents where cracks are extremely small and may escape optical observation. In order to bypass this limitation, a technique was developed by Morris et al.[70] in which a material is indented with multiple probes of varying acuity and the unloading portions of the resultant load-depth curves are compared for superimposability. This technique is described in detail in Chapters 1 and 2. In short, the shape of the unloading slope is determined by the stiffness of the material, and thus the unloading slope should be consistent for materials with homogenous stiffness. Fracture events change this characteristic slope for acute indenters, but not for broad indenters; therefore, a deviation in slope between the two indicates that the more acute indenter induced a fracture event.

In this current study, nanoindentation was used to identify fracture load thresholds for HMX, IDOX, PETN, 246 TFBA, and erythritol. The method outlined by Morris et al was used to determine if samples had fractured, followed by verification via imaging to ensure that unloading analysis is applicable for molecular crystals such as these. Both radial fracture, which typically emanates from the corners of the indent impression, and lateral fracture, parallel to the surface, were observed. For radial fracture, cracks appear at the sides of the indent, indicating either secondary radial fracture which occurs adjacent to corners and at an angle to the indentation axis rather than parallel, or this crack placement may be a result of anisotropy in the crystal itself. Radial fracture was detected using unloading analysis, which was found to be subject to the occurrence of false negatives in which unloading curves will not indicate the presence of fracture yet upon optical investigation a crack is present. The implications of these results to developing new mock options for single crystal materials and formulated plastic-bonded composite materials are discussed.

4.2 Results and Discussion

In this chapter, mN is used in order to best accommodate the scale of the experiments

4.2.1 Analysis of Unloading Curves to Detect Radial Fracture

There are four possible outcomes from performing an unloading analysis as outlined by Morris et al to identify fracture behavior. If unloading analysis and optical observation agree, the result is "true", and if they do not it is "false." A "positive" result is one where unloading analysis indicates radial fracture, while a "negative" result is one that does not indicate fracture. Non-superimposable unloading traces from multiple tips indicate fracture, and if this can be verified optically it is a "*true positive*" result. "*False positive*" results are if the curves are non-superimposable but no fracture of any type is observed – this type of result was never observed either by Morris[70,71] or in this present work. "*True negative*" results are typical of ductile materials or very small loads in brittle materials, wherein the unloading curves are superimposable and no fracture is observed optically. Finally, "*false negative*" results are when the unloading curves are superimposable but a crack is observed optically. Morris found occasional false negatives when the two tips being compared had similar acuities, but stated that cube corner and Berkovich tips were different enough to avoid this issue.

In both types of brittle molecular crystals tested here, we also found significant variation in superimposability of Berkovich and cube corner unloading curves corresponding to fractured crystals. The cube corner indenter probe is significantly sharper than the Berkovich and initiates fracture much more readily. Figure 4.1 compares indentation results for IDOX loaded to 125 mN with both tips. Here, the cube corner indentation resulted in fracture (Figure 4.1(c)) but the Berkovich indent did not (Figure 4.1(d)). In Figure 4.1(b) and all subsequent load-depth curves, in order to directly compare superimposability, the loading portion of the curve has been omitted, and the final depths of both unloading curves have been shifted to the origin to allow for direct comparison despite the increased indentation depth resulting from the acuity of the cube corner probe. In Figure 4.1(b), the unloading portion of the load-depth curves were nearly superimposable but exhibited slight variation in curvature, indicating that the material fractured during the experiment. This is especially notable since, at first glance, the curves do look similar. This is an example of a "true positive" result where the unloading analysis and the optical imaging agree. Sometimes, the unloading curves are quite obviously different. Figures 4.1(e) and 4.1(f) show an example of a cube corner indent that fractured and shows a clear lack of superimposability in unloading traces – another "true positive" result.

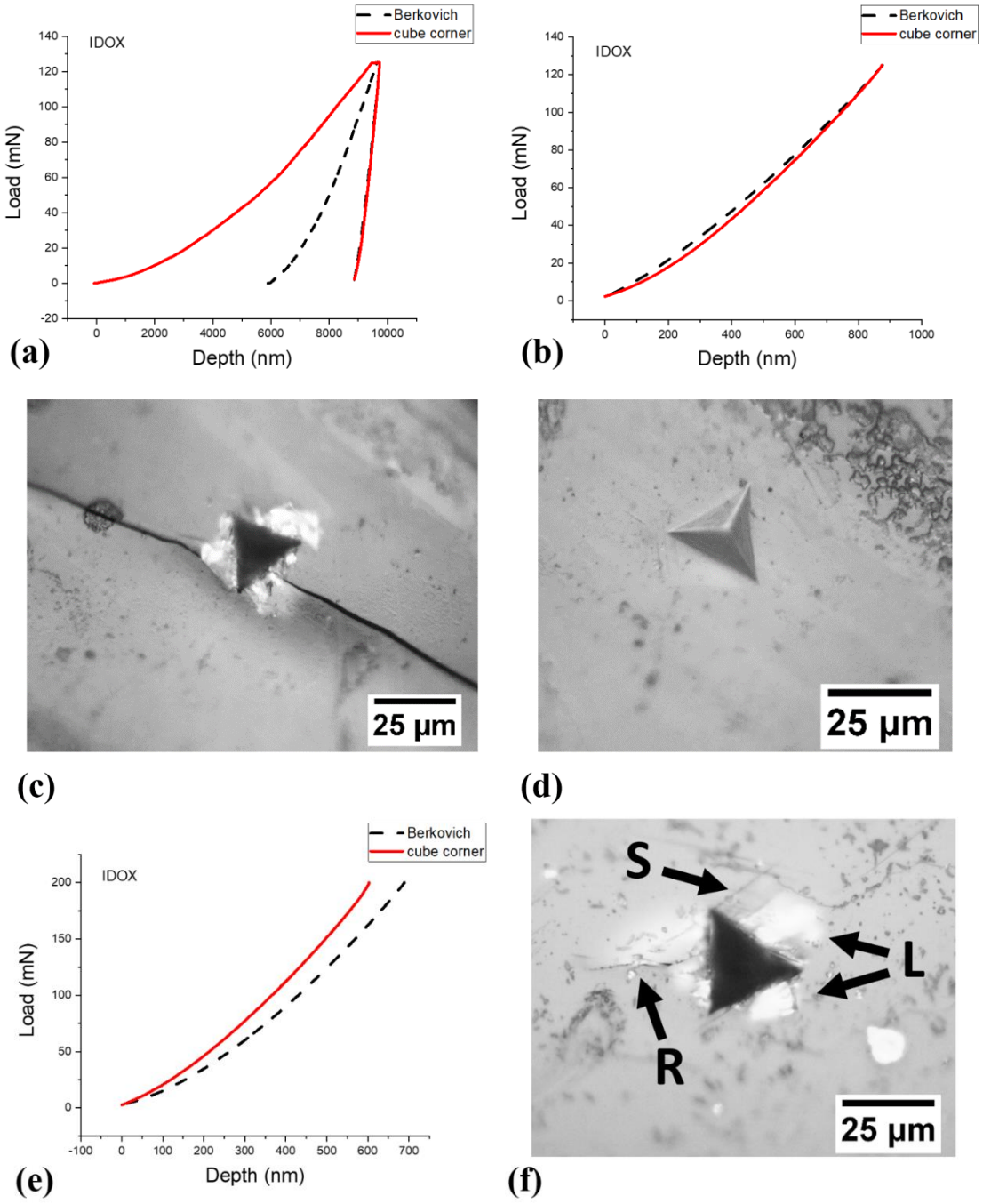

Figure 4.1 *(a) Load-depth curves for IDOX indented at 125 mN shifted along x-axis to align final depths of both curves. (b) Corresponding offset unloading portion of the load-depth show that the unloading slopes are nearly superimposable. (c) The corresponding cube corner indent with visible radial and lateral cracks. (d) The corresponding Berkovich indent with no evidence of fracture. (e) When the unloading portion of the load-depth curves for IDOX indented at 200 mN with a Berkovich indenter and with a cube corner indenter are overlayed, the unloading slopes are not superimposable. (f) The corresponding cube corner indent with visible radial fracture (R), lateral fracture (L), and slip bands (S) indicated by arrows.*

At lower loads, the analysis was generally simple because the materials did not fracture ("true negative"). Figure 4.2 shows cube corner indents that did not fracture, with corresponding unloading curves that are superimposable or nearly superimposable, as predicted by the Morris et al model. Those materials did not fracture, although slip bands were present, indicated by the arrows in Figures 4.2(b) and 4.2(d). Clearly identifiable slip bands following indentation are common in molecular crystals such as these, which have very few, limited slip systems with which to accommodate plastic deformation[36,71,98,99]. Note that the curves in Figure 4.2(c) are not perfectly superimposed. This is a function of translating the entire curve along the x-axis to allow for observation of degree of superimposability; these curves can be considered superimposable because the curvature and slope of the curves are within 5% of each other, which is effectively the resolution due to thermal drift and variations in surface roughness in these materials.

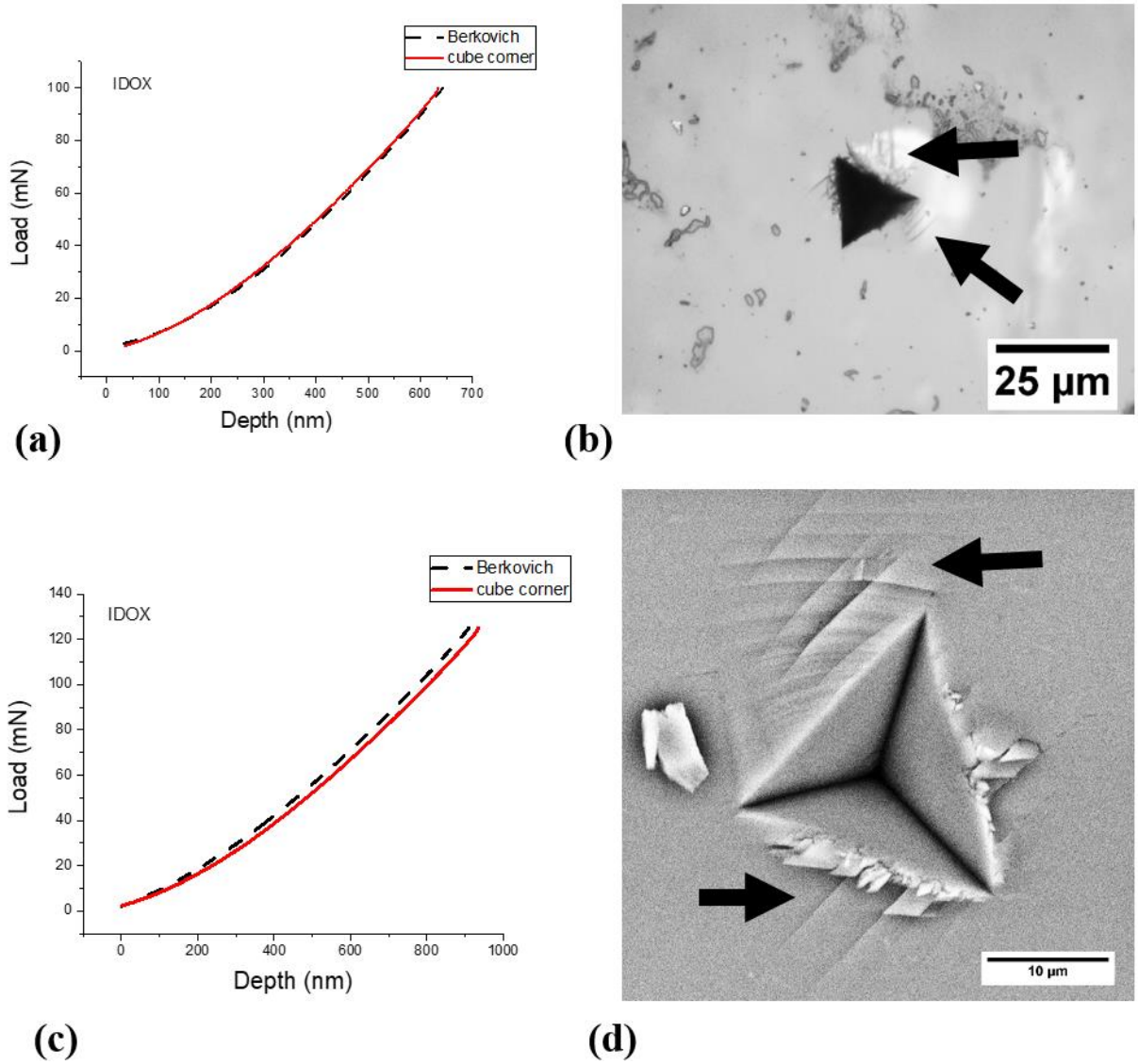

Figure 4.2 *(a) When the unloading portions of the load-depth curves for IDOX indented at 100 mN with a Berkovich indenter probe and with a cube corner indenter probe are graphed with final depth at the origin, the unloading slopes are nearly superimposable. (b) The corresponding cube corner indent with no crack, but with visible slip bands indicated by arrows (the bright region of the figure is due to out of plane deformation, not lateral fracture). (c) When the unloading portion of the load-depth curves for IDOX indented at 125 mN with a Berkovich indenter probe and with a cube corner indenter probe are graphed with final depth at the origin, the unloading slopes are nearly superimposable. (d) The corresponding cube corner indent with no radial cracks, but with visible slip bands indicated by arrows.*

Figure 4.3 shows two examples of cube corner indents causing both radial fracture as well as significant lateral fracture; however the accompanying unloading curves for one are nonsuperimposable (Figure 4.3(a)) and the accompanying unloading curves for the other are

nearly superimposable (Figure 4.3(c)). By unloading analysis alone, without optical observation, the first sample cracked while the second did not. Figure 4.3(a-b) therefore is an example of a *true positive* result, where unloading curves and imaging agree, while Figure 4.3(c-d) is an example of a *false negative*, where the fracture is undetected by unloading analysis but the imaging reveals fracture.

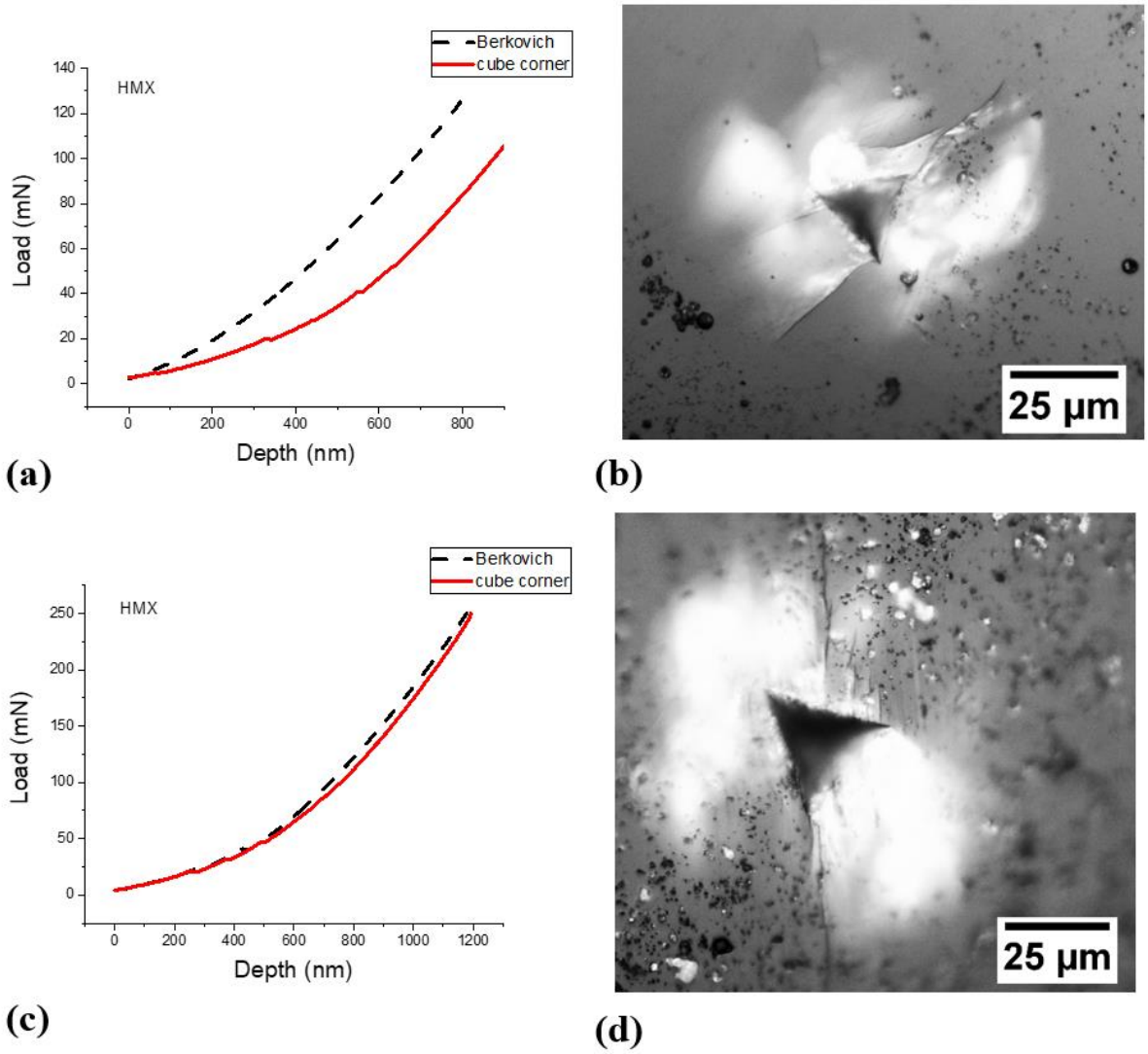

Figure 4.3 *(a) When the unloading portion of the load-depth curves for HMX indented at 125 mN with a Berkovich indenter probe and with a cube corner indenter probe are graphed with final depth at the origin, the unloading slopes are not superimposable. (b) The corresponding cube corner indent with visible radial and latera cracks. (c) When the unloading portion of the load-depth curves for HMX indented at 250 mN with a Berkovich and with a cube corner indenter probe are graphed with final depth at the origin, the unloading slopes are nearly superimposable with some slight deviation. (d) The corresponding cube corner indent with visible lateral cracks.*

4.2.2 Discussion of False Negatives and Crack Mechanisms

As previously mentioned, Morris et al have shown that if a material is indented to the same maximum load with two different indenter probes of sufficient differing acuity and the unloading portions of the load-depth curves are non-superimposable, then the material has fractured [70]. This result was replicated in indentation of IDOX and HMX, with all non-superimposable unloading traces corresponding to fractured crystals. However, the converse statement was not found to be true; if the unloading portions of the load-depth curves are superimposable, the material may or may not have fractured for one of the indenter tips. Morris found this to be true but said that the non-superimposability from cracking would be observed if probes differed enough in acuity [71], with Berkovich and cube corner as an example. Our study showed that even with the Berkovich and cube corner geometries, a fractured sample may still have superimposable or nearly superimposable unloading curves, although this is uncommon. The low frequency of this occurrence is shown in Table 4.1, showing that 92% of results were "true" and all "false" results were in the form of false negatives, where curves are superimposable yet the optical inspection shows that fracture occurred.

Table 4.1 *The number of occurrences of each of the four previously mentioned possible outcomes for each material.*

		SUPERIMPOSABLE	NONSUPERIMPOSABLE
OBSERVED CRACK	*HMX*	3	45
	IDOX	5	28
NO OBSERVED CRACK	*HMX*	9	0
	IDOX	9	0

As can be seen in Figures 4.1(b), 4.1(e), 4.3(b), and 4.3(d), significant lateral cracking was seen in many samples, where fracture is parallel to the material surface and radiates out circularly. Due to the lack of radial symmetry and apparent proximity to the surface, the lateral cracks observed around indents in these materials appear to be "shallow" lateral cracks [67]. The unloading analysis technique is only sensitive to radial fracture, and therefore cannot detect the occurrence of lateral fracture, possibly due to the fact that lateral fracture often occurs at or near

the end of the unloading cycle. Lateral fracture is also not indicated by the indentation loading trace. Because of this, lateral cracking was observed only optically. In instances where lateral fracture occurred, the radius of the optically visible lateral crack was measured and compared to the radius of the indent impression, shown in Figure 4.4. This radius analysis normalizes the crack size relative to the size of the indent (the effective indentation radius, treating the projected contact area as a circle to create an effective radius) and subsequently to the size of the plastic deformation zone. At loads where the material didn't fracture, either at all or some of the time, the ratio of lateral crack to indent impression is near 2, which is approximately the radius that would be expected for the plastic deformation zone around the indent impression. Of particular note here is that the IDOX appears to never extend significantly beyond the plastic zone, whereas the HMX crack grows more than proportionally at increasing loads.

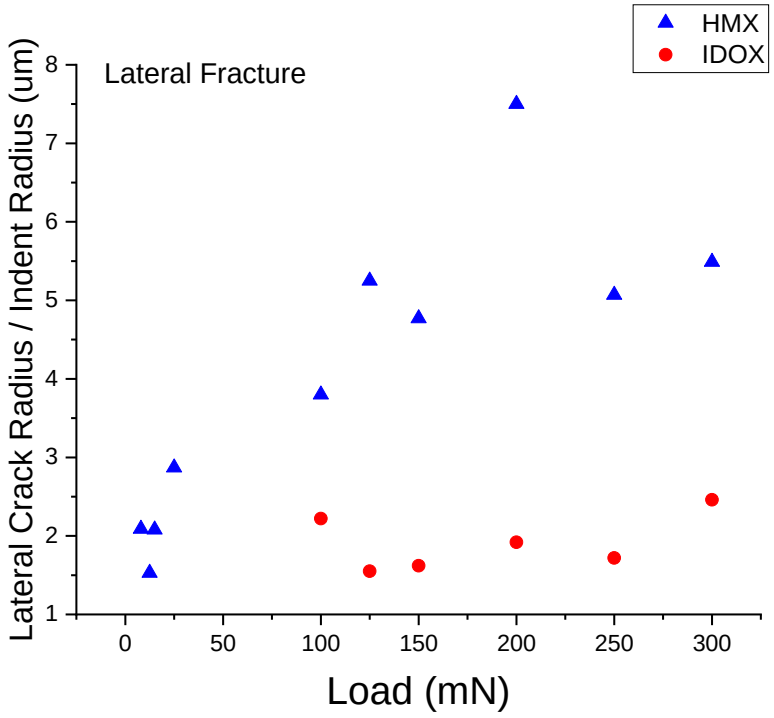

Figure 4.4 *The radius of indent impressions are compared with the lateral cracks seen around the indent, and at loads where the material is not fracturing in all cases, the ratio is approximately 2, which is consistent with the expected size of the plastic deformation zone resulting from an indentation.*

In some cases, such as the one shown in Figure 4.5, unloading analysis results can show a "false negative" where the unloading slopes superimpose yet clear radial fracture is visible, but evidence of *lateral* fracture can still be seen in the form of a pop-out.

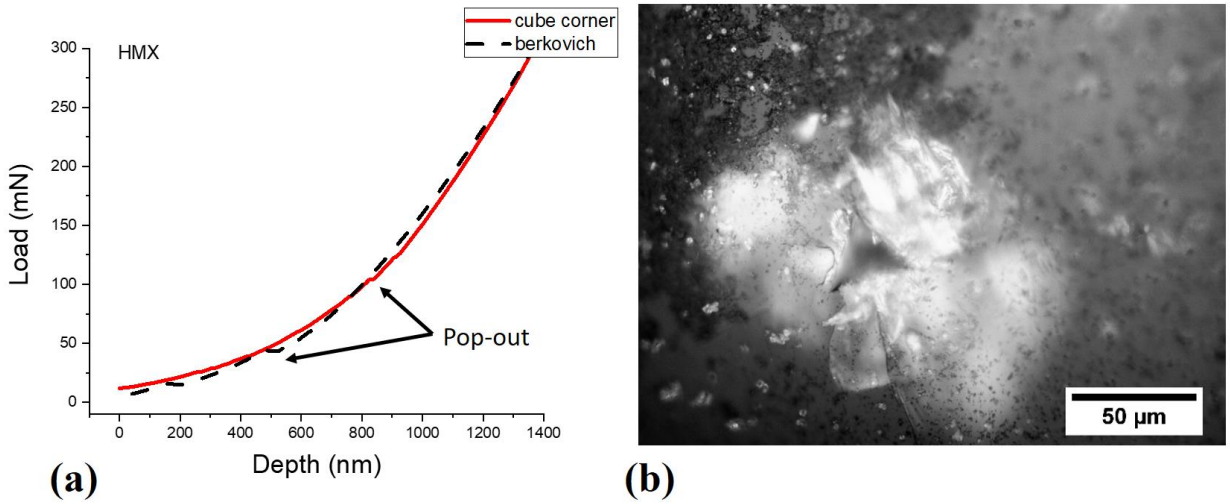

Figure 4.5 *(a) When the unloading portion of the load-depth curves for HMX indented at 300 mN with a Berkovich and with a cube corner indenter probe are graphed with final depth at the origin, the unloading slopes are nearly superimposable with pop-outs, indicated. (d) The corresponding cube corner indent with visible radial and lateral cracks.*

As previously discussed, pop-outs have been seen in samples that experiences lateral fracture. As can be seen in Figure 4.3, these pop-outs are somewhat common in HMX, as is significant lateral fracture.

4.2.3 Radial Fracture Threshold of HMX and IDOX

Approximately 100 crystals of HMX and IDOX were indented with both Berkovich and cube corner tips. The sample size was unusually large for two reasons: one being that these two materials were used to develop the experimental methods, which were subsequently more streamlined for future materials, and the second reason being that these two materials were subjected to particularly high indentation loads that often destroyed the sample such that it could not be reused.

For all indents in this case, the loading rate was proportional to the maximum load with a 30 second load duration. IDOX was found to have a higher radial fracture threshold than HMX,

shown in Figure 4.6. IDOX did not demonstrate any fracture up to or at 100 mN, fractured in every case at 300 mN, and showed a linear trend in fraction of samples fractured between those two outer boundaries. HMX did not demonstrate any fracture up to or at 4 mN, fractured in every case at 8 mN, and showed a linear trend in fraction of samples fractured between those two outer boundaries.

A variation in the threshold for fracture between HMX and IDOX could be due to two primary conditions. First, it could be based on pre-existing flaws and the distribution would be reflective of the flaw distribution. The other likely possibility would be that stochastic events in plasticity (i.e. cross slip) control this behavior. Recent studies of indentation threshold for fracture in glass [100] and earlier studies in Si and Ge [68] have noted that the threshold for fracture is linked to indenter angle, but Mound and Pharr conclude [100] that most initiation models do not yet capture the stress field dependence, and they support the threshold concept in which indentation fracture is driven by the interactions between the plastic and elastic stress fields, in a manner similar to that of Morris et al. In our current study there is not evidence that the defect distribution is significantly greater in IDOX than HMX, even though the range over which the fracture events occurred is almost two orders of magnitude smaller for HMX (< 4 mN range for HMX, and ≈200 mN range for IDOX), and so we believe these data support the plastic-elastic stress field interaction model for fracture initiation during indentation. As suggested by Cook's recent study [101], threshold prediction here would not be improved by "better" (quotes attributed to Cook) estimates of modulus, hardness and toughness; we propose that subtle differences in the elastic and plastic stress/strain fields in these materials with limited slip will always lead to variation within a material. However, the significant difference in the "threshold" value (≈ 5 mN for HMX, and 200 mN for IDOX), for materials with similar modulus and hardness values, implies that the toughness of HMX is significantly less than that of IDOX.

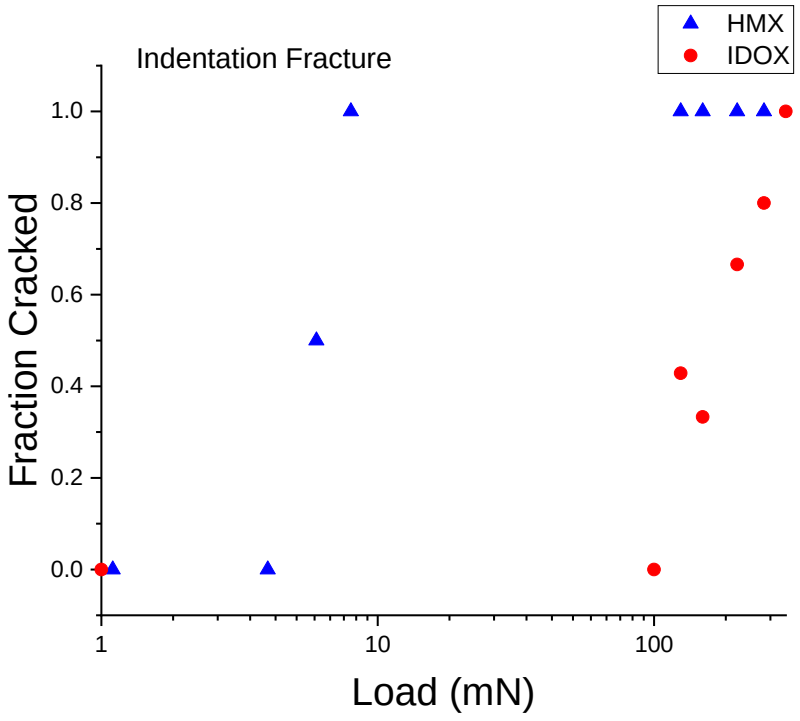

Figure 4.6 *Fraction of crystals that cracked under quasistatic loading at various loads. Indentation fracture initiation in IDOX requires loads above 100 mN and all samples fracture at a load of 300 mN, whereas indentation fracture initiation in HMX requires loads above 4 mN and all samples fracture at a load of 8 mN.*

4.2.4 Radial Fracture Threshold of PETN, 246 TFBA, and Erythritol

Similarly, 13 crystals of PETN, 246 TFBA, and erythritol were indented with both Berkovich and cube corner tips. This sample size was able to be substantially less than previous sample sizes, for two reasons: one being that the experimental methods had been well developed and optimized before these experiments were performed, and the second reason being that the crystals were large enough and the indentation loads small enough that multiple tests could be performed on a single crystal without interference.

All indents were performed with a loading rate proportional to the maximum load with a 30 second load duration. In this case, cube corner indents resulted in fracture, with all materials tested at loads as low as 500 μN. Unloading curves indicating fracture for each material at 500 μN are shown in Figure 4.7. It was decided not to continue fracture testing below this threshold,

as particularly low indentation loads are more prone to noise, and as previously noted, these loads are already far below expected processing loads for these materials[97].

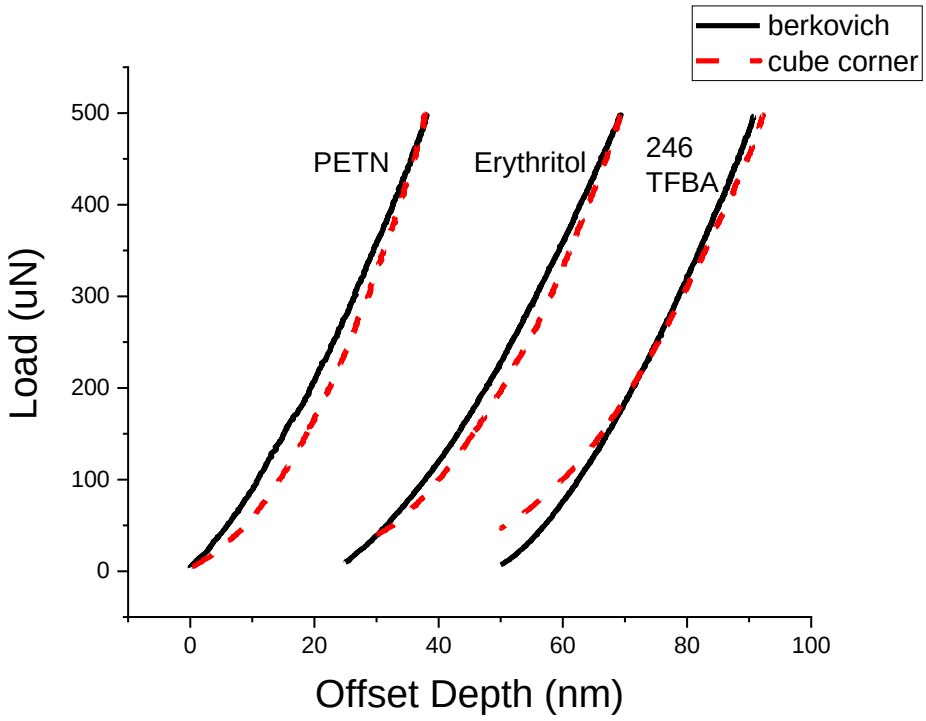

Figure 4.7 *Unloading traces indicating indentation-induced fracture at 500 μN for PETN, erythritol, and 246 TFBA.*

Based on these results showing fracture in PETN, erythritol, and 246 TFBA with a *cube corner* probe at loads as low at 500 μN, the validity of Berkovich measurements on these materials at a maximum load of 1 mN became a concern, as the method used for determining hardness and elastic modulus is only valid for indents in which a fracture event did not occur. In order to address these concerns, PETN was indented with a Berkovich probe at loads of 1 mN intervals from 2 mN to 12 mN and scanning probe microscopy was used to check for evidence of cracking. Figure 4.8 shows typical images for indents at loads of 2 mN, 4 mN, and 12 mN. The 12 mN indent shows clear evidence of fracture while the 2 mN and 4 mN indents do not. Overall, Berkovich fracture was never observed in PETN at loads below 8 mN. This result provided confidence in measurements taken with a Berkovich probe at 1 mN.

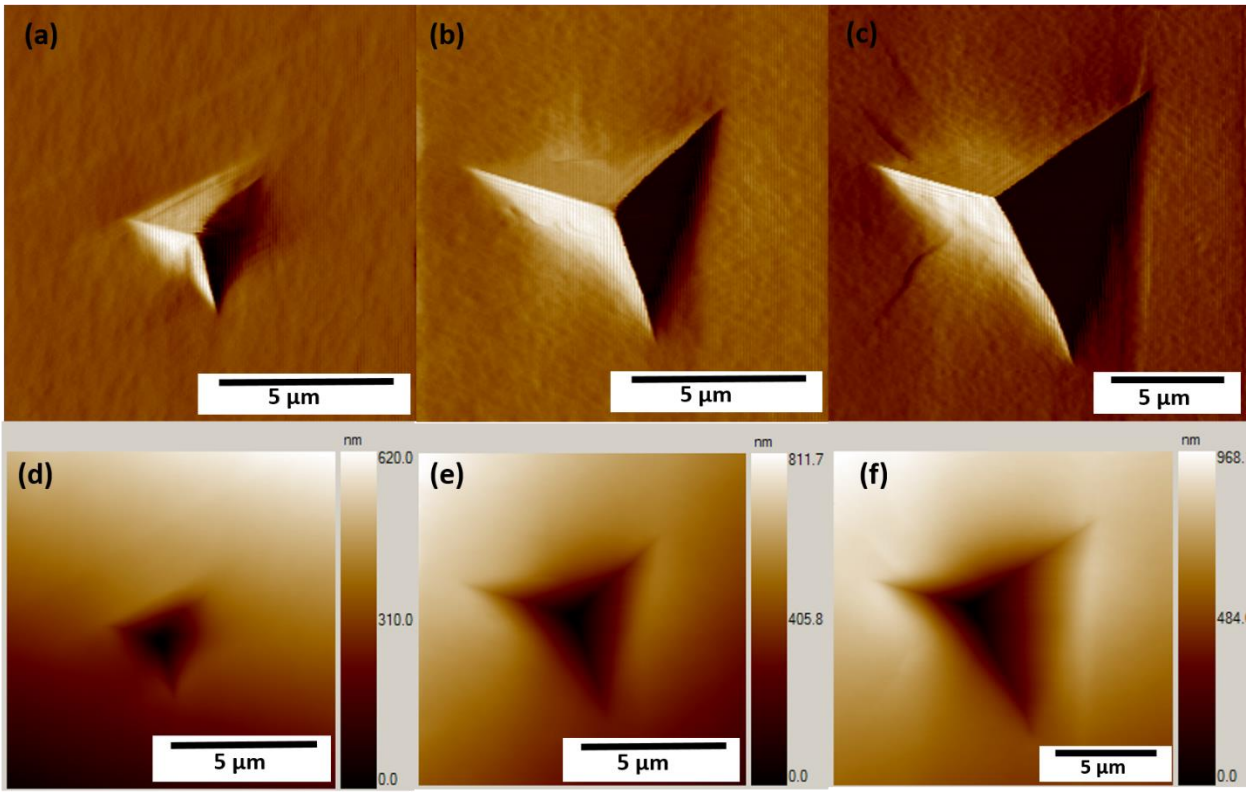

Figure 4.8 *Scanning probe images (gradient) of Berkovich indents in PETN at loads of (a) 2 mN with no evidence of fracture, (b) 4 mN with no evidence of fracture, and (c) 12 mN with possible fracture visible, and (d-f) scanning probe images (topographical) of the same indents as (a-c) respectively*

4.2.5 Loading Rate Effects

For all indent data shown in Figure 4.6, the loading time was held constant at 30 seconds, and the only parameter that was variable was maximum applied load. As a result of this, the loading rate during indentation increased with maximum applied load, as high as to 10,000 μNs^{-1} for the 300 mN indents. In order to observe the effect of variable loading rate on indentation fracture, additional indents were performed on IDOX where the loading time was variable rather than applied load. These additional tests were performed at loads of 100 mN and 300 mN, shown in Figure 4.9. As shown in Figure 4.9(a), increasing loading rate from 3,333 μNs^{-1} to 10,000 μNs^{-1} for 100 mN indents continued to show superimposability in unloading traces, yet Figure 4.9(b) shows that fracture occurred, meaning that this was a false negative result in the unloading analysis. So in this case, increasing the loading rate at lower loads induces fracture that does not occur at slower loading rates. Conversely, as shown in Figure 4.9(c), decreasing loading rate

from 10,000 μNs^{-1} to 3,333 μNs^{-1} for 300 mN indents still resulted in fracture, shown in Figure 4.9(d), just as in indents with higher loading rates. In this case then, decreasing the loading rate at higher loads does not prevent fracture.

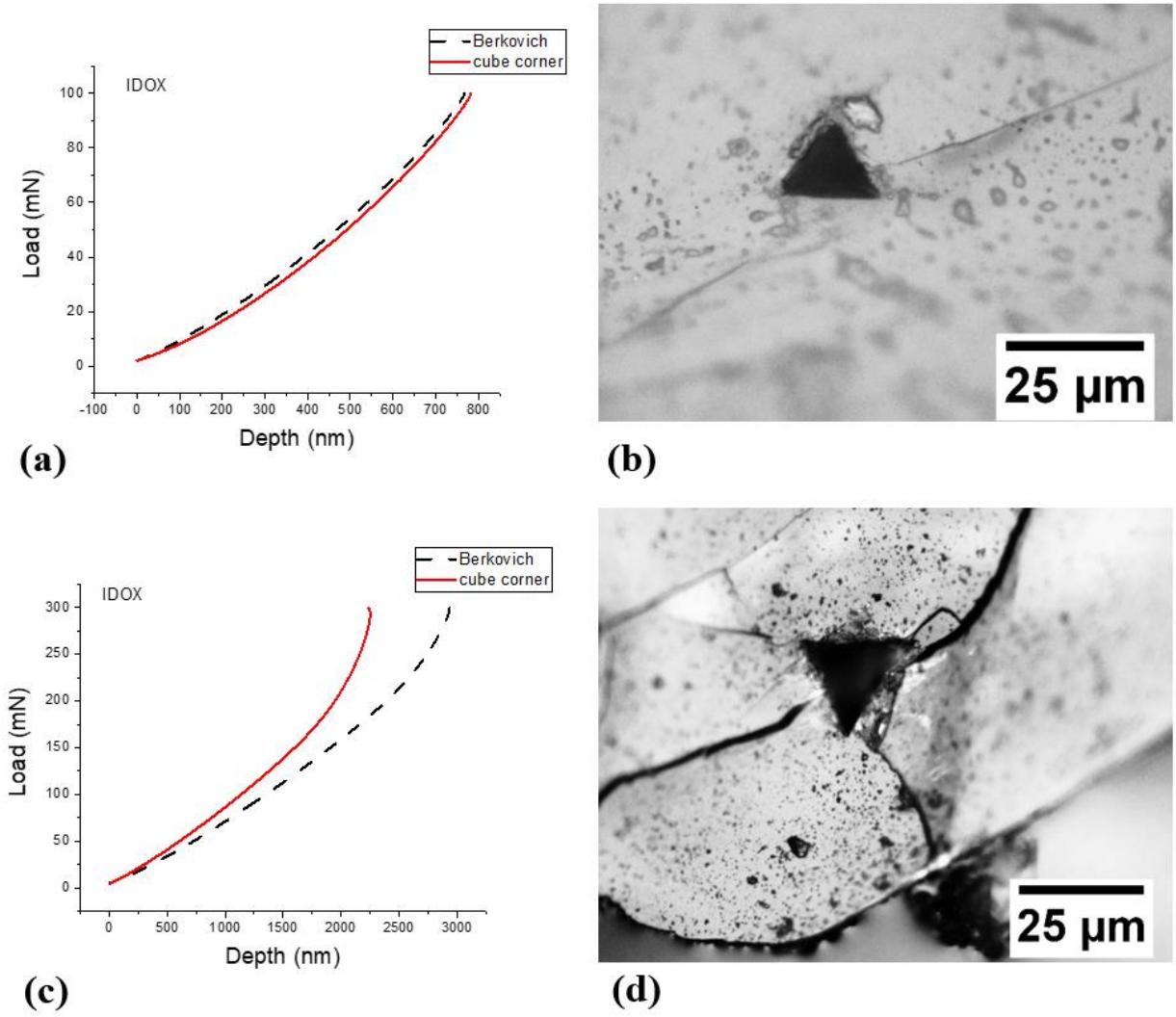

Figure 4.9 *(a) When IDOX is indented at 100 mN with a loading rate increased from 3,333 μNs^{-1} to 10,000 μNs^{-1} and the unloading portion of the load-depth curves for a Berkovich indenter probe and a cube corner indenter probe are graphed with final depth at the origin, the unloading slopes are nearly superimposable. (b) The corresponding cube corner indent with visible radial cracks, meaning that this was a false negative result. (c) When IDOX is indented at 300 mN with a loading rate decreased from 10,000 μNs^{-1} to 3,333 μNs^{-1} and the unloading portion of the load-depth curves for a Berkovich indenter probe and a cube corner indenter probe are graphed with final depth at the origin, the unloading slopes are not superimposable. (d) The corresponding cube corner indent with visible radial cracks.*

4.2.6 Toughness Measurements

Indentation fracture toughness most often relies on self-similar fracture morphologies, with relationships between load (or indentation impression size) to the crack size providing a model to extract effective toughness parameters. In the case of the anisotropic molecular solids described here (and most likely in other similar molecular organic systems), the ability to create repeatable self-similar morphologies is limited, given the state of the art in nanomechancial testing of sub-millimeter crystalline forms, with radial, secondary radial, and lateral cracks occurring stochastically. Comparing estimates of the toughness via the threshold value for fracture to those developed from crack – load relationships can help provide confidence in the material to material comparison. As described in Chapter 1, from Jang and Pharr [68], the critical threshold load, P_C is

$$P_C = C\left(\frac{H}{E}\right)^2\left(\frac{T}{H}\right)^3 T \qquad (1)$$

Where *C* here is an agglomeration of geometric constants that address indenter shape and the stress fields around the indenter. We choose to represent *T* for toughness to note we have not met the criteria for a bulk stress intensity for fracture (i.e. plane strain and crack extension, not formation). In short, the relative toughness of two materials with the same modulus and hardness, such as HMX and IDOX, should scale with the critical load to the ¼ power. So, the toughness of IDOX could be expected to be approximately 2.4 times the toughness of HMX with some variation due to the small difference in elastic modulus. This is indeed the case, with this method giving a toughness measurement of 0.219 MPa $m^{-1/2}$ for HMX and 0.572 MPa $m^{-1/2}$ for IDOX.

As discussed in Chapter 1, other indentation fracture toughness models consider the length of the resultant crack. One of these models is by Morris and Cook [69], where the load and crack length ratio relate as

$$\frac{P}{c^{3/2}} = \frac{T}{\chi^R} - \frac{\chi^E}{\chi^R}\frac{P}{c^{3/2}}\ln\left(\frac{2c}{P^{\frac{1}{2}}}(\alpha H)^{1/2}\right) \qquad (2)$$

Where χ^E is a dimensionless stress-intensity factor amplitude term, χ^R varies with hardness and elastic modulus as well as incorporating a geometry factor, and α relates to the projected contact area.

Using this model, the average T for IDOX is 0.38 MPa $m^{-1/2}$ and for HMX as 0.26 MPa $m^{-1/2}$. This is a ratio of 1.5, compared to the ratio of 2.4 that was predicted by the Jang and Pharr method, with the discrepancy coming largely from the IDOX measurements. The Morris and Cook model can be difficult to apply to HMX and IDOX, given that the predominant fracture mechanism is not radial, and when radial fracture does occur it is often not at indent corners.

Both of these models are difficult to apply to PETN and its mocks given what is currently known, which is only that each material has a 100% fracture rate at all loads at and above 500 µN with a cube corner indenter. However, this is sufficient to allow the calculation of a maximum theoretical fracture toughness (T_{max}) with the Jang and Pharr method if the critical load is assumed to be 500 µN. Under these conditions, T_{max} for PETN would be 0.0771 MPa $m^{-1/2}$, for 246 TFBA T_{max} would be 0.0896 MPa $m^{-1/2}$, and for erythritol T_{max} would be 0.0653 MPa $m^{-1/2}$. These maximum possible values are approximately a third of the toughness of HMX and approximately an eighth of the toughness of IDOX.

4.3 Implications about Proposed Inerts as Mocks

Fracture mechanisms are similar between HMX and IDOX, with radial fracture often emanating from the sides of indent impressions rather than corners, and with the presence of significant asymmetric lateral fracture near the surface. However, single crystal IDOX is more resistant to indentation fracture, whereas in plastic-bonded composites HMX had been the more fracture resistant of the two. This could indicate that besides differences in fracture toughness of single crystals, there may also be differences in surface interactions and binder adhesion between the two materials. One goal of developing IDOX was to use it as a generic mock for HMX in any plastic-bonded formulation. The fracture differences seen here could limit the ability of IDOX to mock HMX in some formulations or test conditions. However, even with these considerations IDOX still shows improved properties compared to previous mocks such as sucrose or barium nitrate.

In PETN, 246 TFBA, and erythritol, fracture mechanisms were not observed because the low fracture thresholds resulted in indents and cracks too small for optical inspection. All three materials had a 100% fracture rate at the minimum load applied via cube corner probe, so while specific fracture toughnesses cannot be compared, it can easily be concluded that 246 TFBA and erythritol are both sufficiently brittle to mock the poor indentation toughness displayed by PETN.

4.4 Conclusions

Indentation fracture in molecular organic materials can have a range of threshold values, suggesting that materials that exhibit plastic and elastic anisotropy lead to complex stress states. The variation that one would expect based on small variations of the in-plane rotational angles between the tip and crystal can result in both radial and secondary radial crack initiation. Indentation fracture in IDOX initiated between 100 mN and 300 mN, with indents at loads lower than 100 mN displaying no fracture, and all indents at loads of 300 mN or higher displaying fracture. Both radial and lateral cracks were observed. Cracks often emanated from the sides of indents rather than corners, characteristic of secondary radial fracture. HMX indentation fracture also initiated over a range, but between 4 mN and 8 mN, with all indents at loads of 4 mN or lower displaying no fracture, and all indents at loads of 8 mN or higher displaying fracture. Indentation fracture for PETN, 246 TFBA, and erythritol initiated at even the lowest loads applied.

First order estimates of the toughness using both load – radial crack models as well as a cracking threshold load suggest that the toughness of HMX is only 1/3 that of IDOX. Since IDOX is under consideration as a mechanical mock for HMX, these indentation fracture results indicate that the ability of IDOX to simulate the mechanical behavior of HMX is best suited to those cases where elasticity and plasticity, and not fracture, are the dominant deformation mechanisms. Toughness of PETN, 246 TFBA, and erythritol cannot be calculated with a known degree of accuracy, but a maximum possible toughness value can be reported for all three and is comparable for all three given what is currently known.

While unloading analysis proved to be over 90% accurate, optical inspection of indent impressions revealed some superimposable unloading curves to be false negatives,

demonstrating the value of a secondary detection technique when possible; however, in cases where fracture toughness is too low to optically view indent impressions created below the fracture threshold, unloading analysis can be a particularly useful and informative tool. Analyzing only the unloading portion of the load-depth curve can also inform on the prevalence of lateral fracture, as many indents with significant lateral cracking can be identified via pop-outs on the unloading trace.

5. ORIENTATION EFFECTS IN INDENTATION OF MOLECULAR CRYSTALS

Portions of this chapter have previously been published in Crystals (A Thermal and Nanomechanical Study of Molecular Crystals as Versatile Mocks for Pentaerythritol Tetranitrate. A Burch, Z Wilde, D Bahr, J Yeager. Crystals, Vol 10, Issue 2, pp.126(1:15). doi: 10.3390/CRYST10020126. 2020)

5.1 Background and Motivation

As was seen in Chapter 4 and is depicted again here in Figure 5.1(a), during indentation fracture investigation of HMX and IDOX there were many cases in which cracks appeared along the flat sides of the indent impression, rather than at the corners as is expected due to the stress concentration present at indent corners (shown in Figure 5.1(b))[67]. This prompted the question, if the stress field of the pyramidal indenter geometry is not the predominant driving force in crack formation, then what is determining the point of origination and direction of propagation of cracks? Furthermore, is this effect unique to fracture events, or do other indentation measurements share this seemingly "preferred" orientation effect?

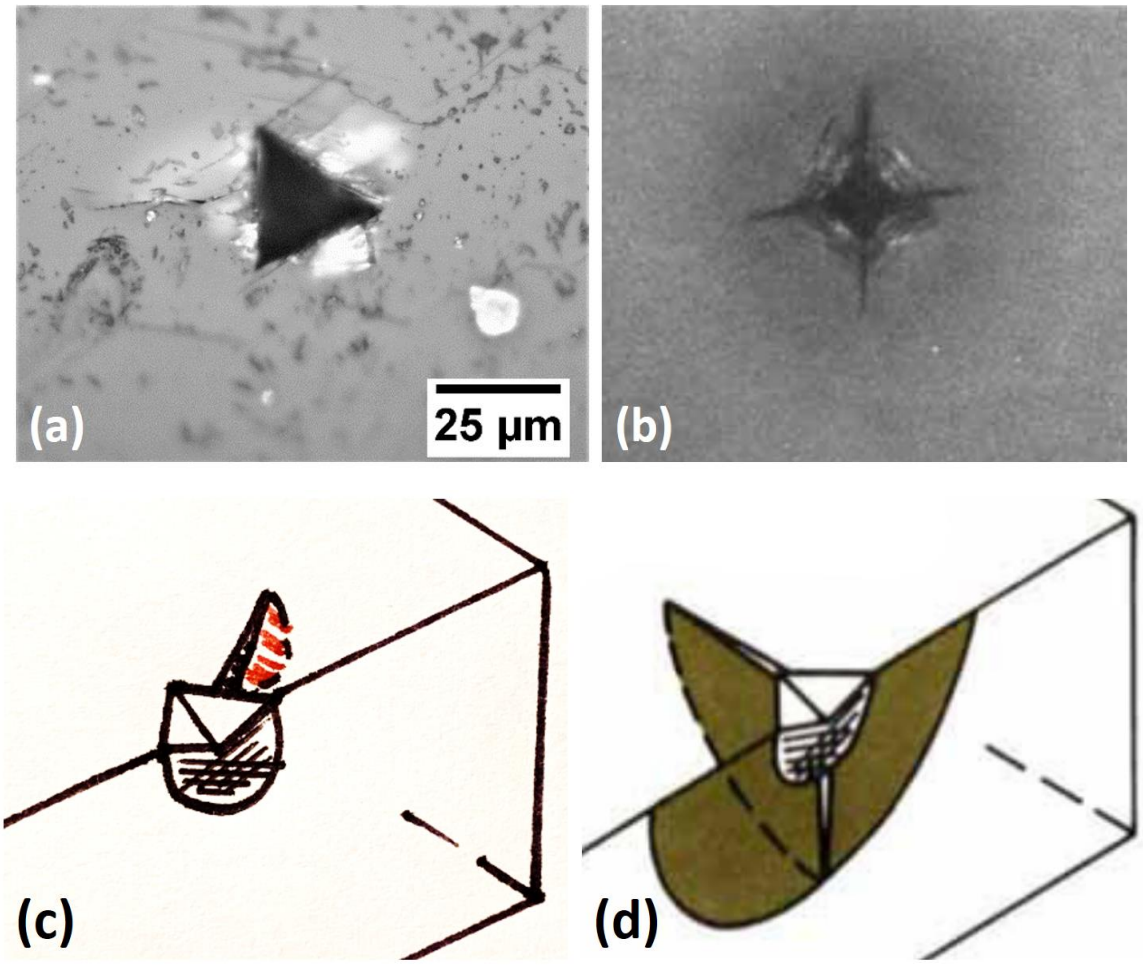

Figure 5.1 *(a) An indent in IDOX in which fracture was induced as a direct result of indentation and the crack emanates from the flat side of the indent, (b) an indent in fused silica in which fracture was induced as a direct result of indentation and the cracks emanate from indent corners*[67]*, (c) a representation of the type of radial-esque fracture that is expected to have occurred in (a), and (d) a representation of "halfpenny" fracture that is typical in cases such as (b), where radial cracks from all corners are joined below the indent impression*[67].

As discussed in Chapter 1, in-plane indenter orientation effects have previously been studied in metals[102] at quasistatic loads with flat punch indenter tips. In these types of studies and particularly in simulations, many assumptions are made, such as the material being an infinite isotropic half-space[102], and the indenter being axisymmetric[82]. Of course, real materials often are not infinite and isotropic, and many popular indenter probes are not axisymmetric. We've seen that the axisymmetric indenters will interact with a material differently than a pyramidal indenter, with a 5.8% difference in perceived modulus. While this assumption could be validated by widespread use of axisymmetric indenters, pyramidal indenters like Berkovich are popular for

good reason: a sharp point is easier to achieve with this geometry, and easy to calibrate. Additionally, indentation standards such as ISO and ASTM call for the use of pyramidal indenters. Thus, the axisymmetric indenter approximation cannot simply be validated by choosing only axisymmetric indenters.

The assumption of an isotropic material also should not be broadly applied to all indentation samples, such as molecular crystals which are known to have high degrees of anisotropy. Addressing this, as previously discussed, in-plane indenter orientation effects have also been studied in molecular crystals in a monoclinic[19] and a tetragonal[78] system at quasistatic loads with a single pyramidal indenter geometry. IDOX, the material pictured in Figure 5.1 with a radial crack emanating from the side of the indent impression rather than the corner, has a triclinic structure, which is less symmetric than monoclinic or tetragonal. As the reduced symmetry of triclinic molecules were not addressed in either of these studies, there was a desire for application of these previous methods to this structure. In addition, there was also the desire to test this quasistatic in-plane rotational technique with a *non*-pyramidal indenter probe such that there are no corners to be oriented in a particular direction, as well as to test in-plane orientation effects at loads sufficient to induce fracture, given that fracture events were what initially raised the question of in-plane orientation dependence in these materials.

5.2 Results and Discussion

5.2.1 Quasistatic Low-load Indentation Orientation

In pursuit of understanding quasistatic in-plane orientation effects of various molecular crystal symmetries, testing was done on four materials: PETN, a tetragonal crystal, HMX, a monoclinic crystal, erythritol, a tetragonal crystal, and IDOX, a triclinic crystal. As described in Chapter 2.3.3 and summarized here, on various crystals of each material a single face of the crystal was chosen to be indented, and an arbitrary direction of that face chosen as the origin, labeled 0°. Two probes were chosen to study any in-plane anisotropy. First, a typical pyramidal (Berkovich) tip was used, which has 120° angle between the edges. Second, an axisymmetric conical tip was used, with a circular cross section. The axisymmetric tip should show no in-plane orientation effects; if any were observed, the variation should only be due to random variability in the local properties. During the experiment, each crystal was rotated about a consistent normal

direction relative to the arbitrary origin, and indented at 30° intervals with both Berkovich and conical probes. The goal was to determine typical variability of elastic modulus and hardness as a function of indenter probe angle. A representation of these 30° rotations is shown with an IDOX crystal in Figure 5.2.

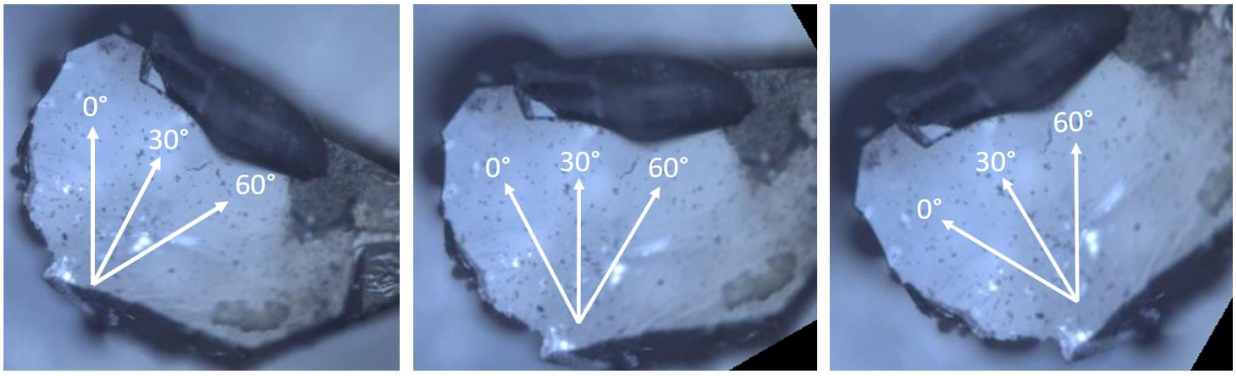

Figure 5.2 *An IDOX crystal rotated at 30° intervals to vary the in-plane angle of the indenter probe*

The results, exemplified in Figure 5.3 for one selected crystal of each material, were that the in-plane orientation of the indenter relative to the crystal surface did not seem to affect the measured properties. Some random indents had abnormally low or high modulus results due, most likely, to local material properties (e.g. defects), but there were no systematic trends, particularly trends which would repeat at orientations that would align with equivalent directions (i.e. (111) and $(11\ \overline{1})$). This finding provides confidence in all nanoindentation-derived mechanical properties measured to date in these highly anisotropic molecular crystal materials.

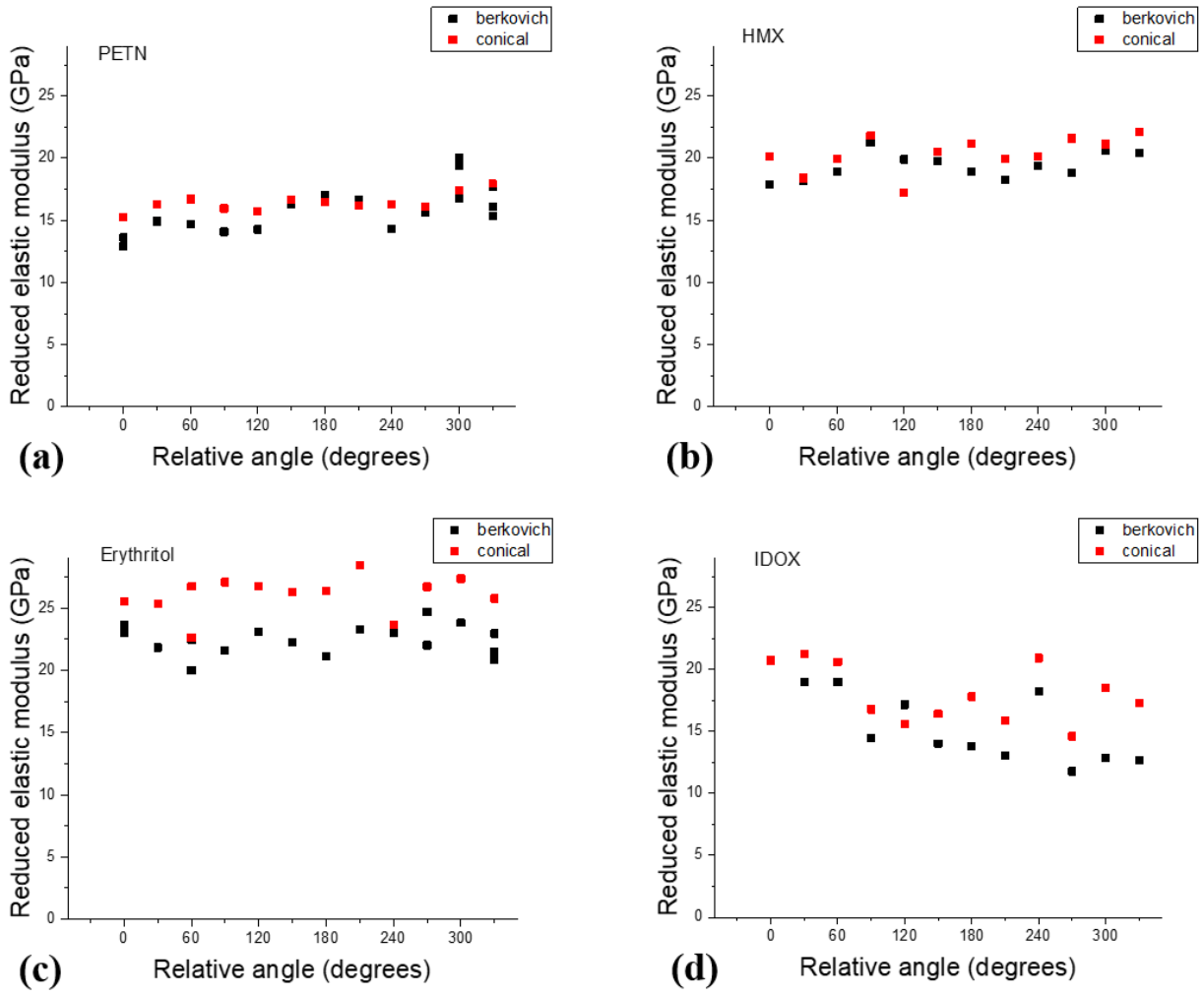

Figure 5.3 *Elastic modulus shows no correlation to angle with either a pyramidal or conical probe in (a) PETN, (b) HMX, (c) erythritol, and (d) IDOX*

It should be noted that the average elastic moduli seen in Figure 5.3 for HMX and IDOX, 19.9 GPa and 16.8 GPa respectively, are significantly lower than the averages reported in Chapter 3, which were 25.2 GPa and 23.3 GPa respectively. Rather than an error in measurement or preparation technique, this is simply an example of the amount of variation than can exist in these materials between both crystallographic faces as well as between individual crystals. This serves to exemplify the importance of sampling a broad range of crystals with varied out of plane orientations in order to best achieve a true average, and the importance of understanding the limits of what can be learned from a single crystal. IDOX has a triclinic crystal structure, which as mentioned in Chapter 2 is the least symmetric structure surveyed in this paper, and IDOX also

tends to show the highest degree of variability, making it a particularly interesting material with which to study orientation effects.

5.2.2 Indentation Fracture Orientation

Figure 5.3 shows the IDOX crystal after all 8 indents where the goal was to induce fracture at various indenter orientations. Note that a significant majority of the cracks extend down and to the right at a 55° angle (clockwise) from the top edge of the crystal as pictured, regardless of indenter orientation. Some marks on the crystal following the same approximate angle are visible before local indentation.

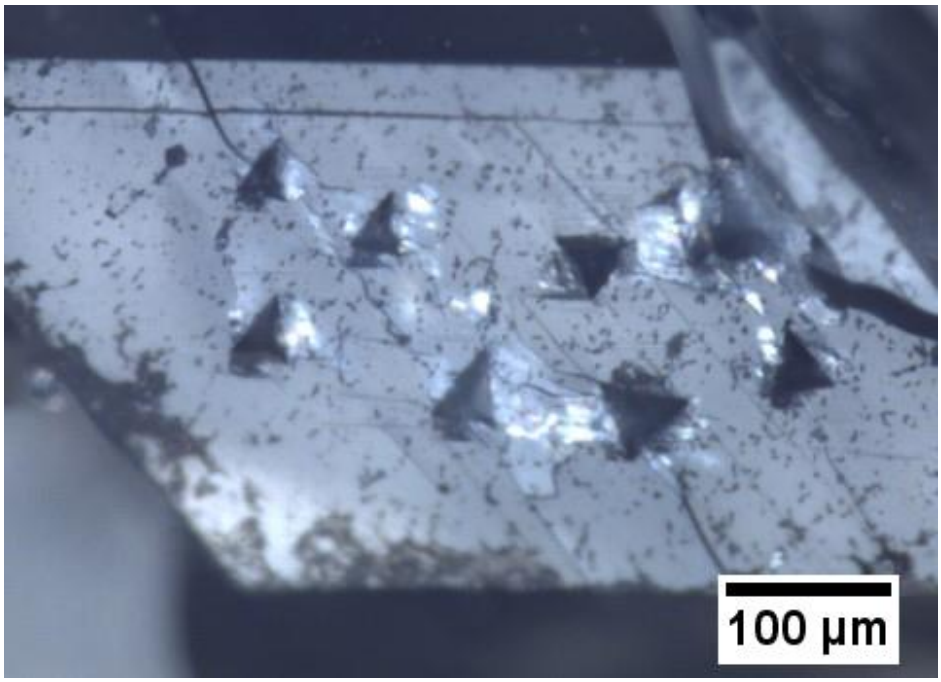

Figure 5.4 *IDOX single crystal with indentation-induced fracture with a clear preferential orientation, approximately 55° clockwise from the top edge as pictured.*

Figure 5.4 shows more detailed views of each indent, with most (though not all) cracks extending approximately 55° clockwise from the top edge of the image (which is aligned with the top edge of the crystal). Crack orientation appears to be independent of indenter orientation, and the point of origination for the crack also appears to be arbitrary with respect to the indenter, with cracks coming from both indent corners as well as along various lengths of the indent sides.

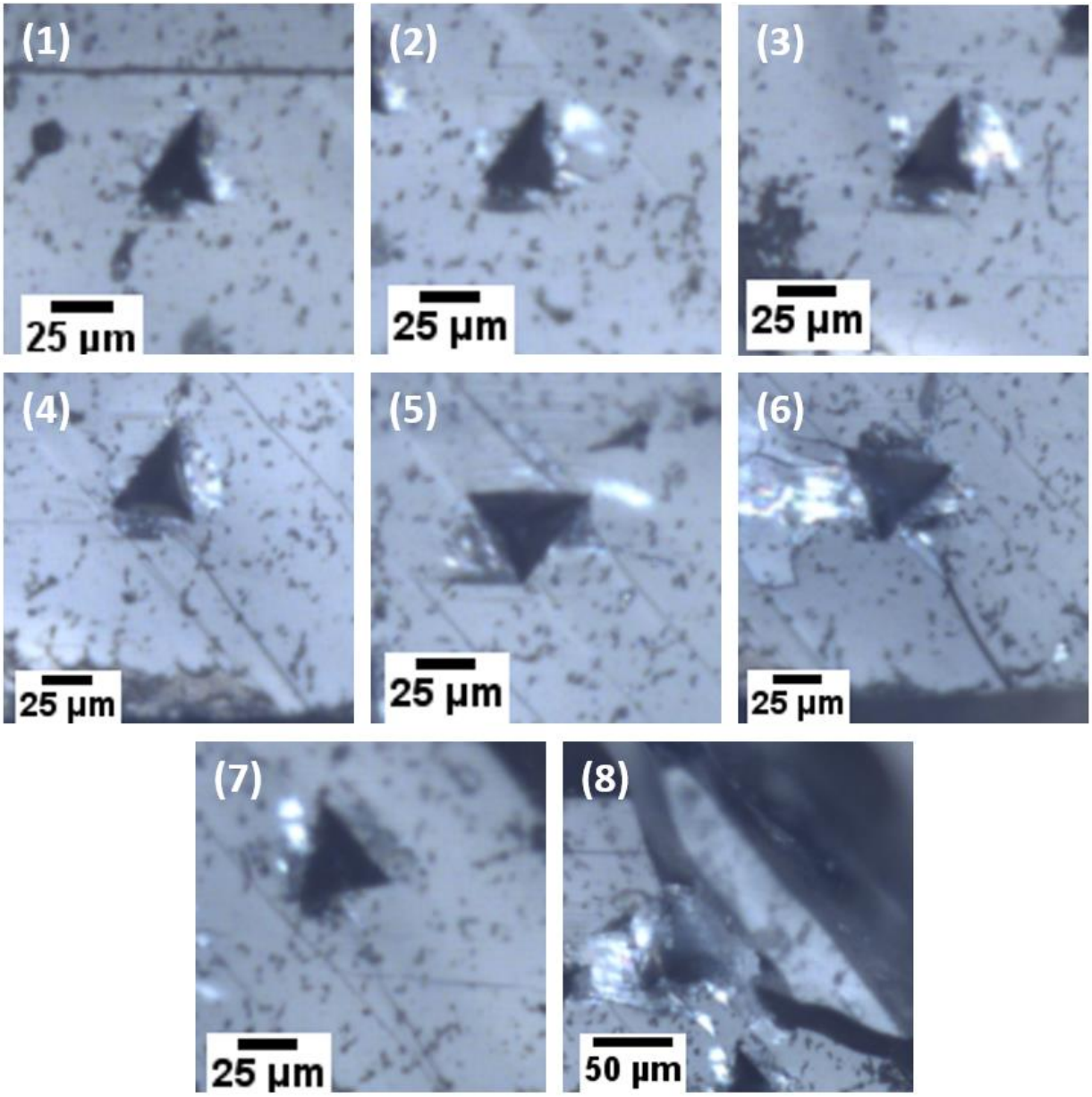

Figure 5.5 *Detailed views of each IDOX indent and its fracture patterns*

While the results in section 5.2.1 indicated a lack of any variation among orientations, the results shown here tell a broader story of *strong* orientation preferences that are simply insensitive to and agnostic of indenters and indenter orientation.

As seen in Figure 5.5, there can be some stress field interaction between indents that creates cracks that do not follow the preferred orientation otherwise seen.

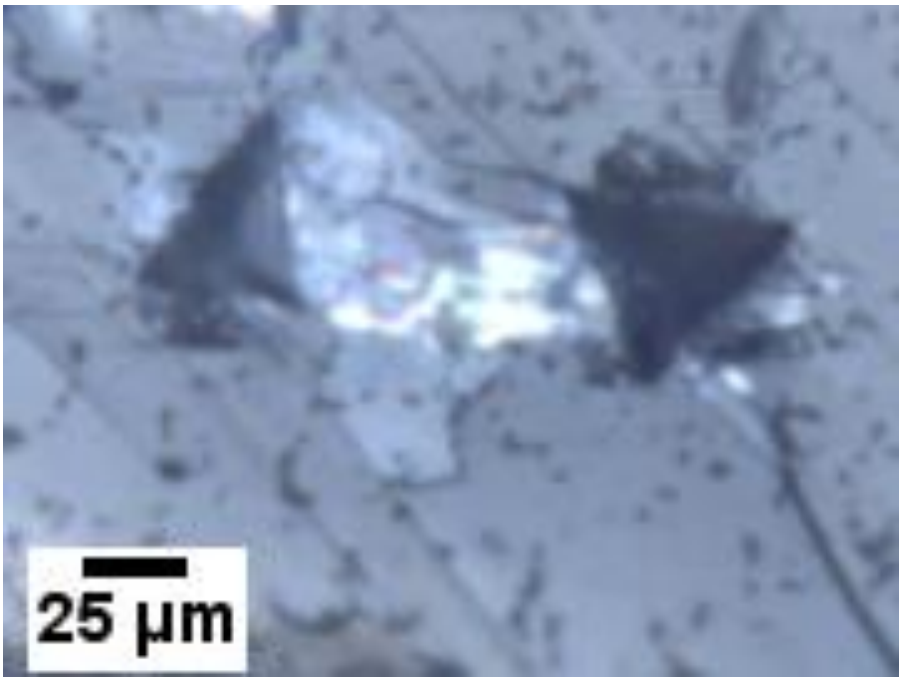

Figure 5.6 *Fracture resulting from interacting stress fields between indent 4 (left) and indent 6 (right)*

However, stress field interaction can still be sensitive to the crystal's preferred fracture direction. In the first indent applied to this sample, as seen in Figure 5.6, there was only slight fracture visible upon initial observation. Following the addition of the fourth indent, a crack appeared on (1) that had not previously been present. By the time the eighth indent had been performed, this crack had widened significantly.

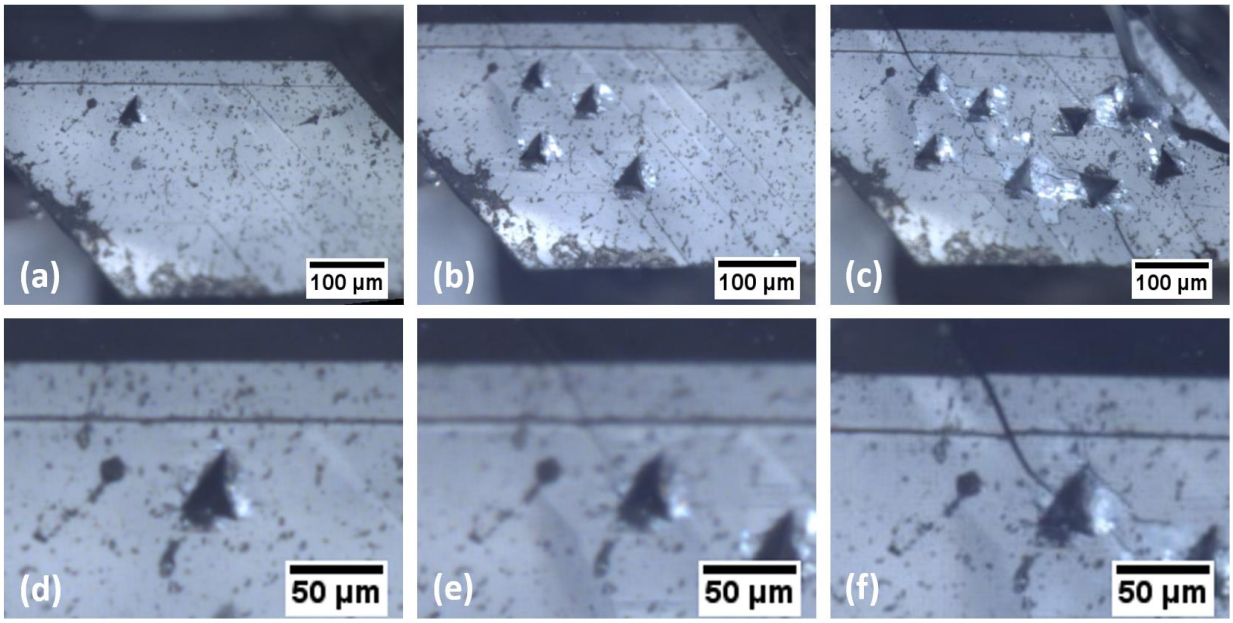

Figure 5.7 *(a) Indent (1) with minimal cracking, (b) Indent (1) now showing a hairline crack extending to the upper edge of the crystal, (c) the same crack now wider and more prominent, (d) a close-up of (a), (e) a close-up of (b), (f) a close-up of (c)*

This crack, which nucleated and propagated as a result of additional stresses from subsequent indents, follows the crystal's preferred fracture direction despite the relative location or orientation of these subsequent indents.

5.3 Conclusions

Elastic modulus as measured by nanoindentation shows only stochastic variation, independent of in-plane indenter orientation, or lack thereof in the case of an axisymmetric probe. This result was seen in four different materials, all molecular crystals, representing three different crystals structures with varying levels of asymmetry. This consistently orientation-agnostic result allows confidence that past measurements were not biased by the probe orientation, nor must care be taken in the future to orient the probe a certain way or vary the ways in which it is oriented.

Indentation-induced fracture was quite strongly oriented in a preferred direction, but this direction was entirely independent of indenter orientation or geometry; the indenter orientation did not impact the direction in which cracks propagated, and the pyramidal shape of the indenter

did not impact where the cracks originated. While it is typical for cracks to emanate from the corners of pyramidal indenters, in the triclinic IDOX crystal fractured here, cracks appeared from seemingly random points along the flat sides of the indent impression, sometimes more near to one corner and at other times centered between two corners. Because of this tendency of cracks to ignore both indenter orientation and geometry, indentation is an effective method of testing fracture behavior as fracture response is largely driven by stress fields within the material rather than the indenter itself. This does mean, however, that toughness measurements such as those calculated in Chapter 4 should be understood to be specific to the indented face of the crystal and may not be broadly applicable to the material as a whole. Crystal orientation and fracture toughness of specific planes dominate fracture response, which may affect how polycrystalline composites such as a PBX respond to stresses.

6. CONCLUSIONS

The objectives of this work were twofold:

(1) To determine the suitability and robustness of nanoindentation as a primary screening technique for new mock material candidates
(2) To identify appropriate mock materials for selected explosives

In order to address these points, nanoindentation techniques were used to assess the selected explosives and a selection of mock candidates on the basis of quasistatic mechanical properties, fracture response, and degree of in-plane orientation sensitivity. The results of these tests and their implications regarding the research objectives are discussed here.

6.1 Quasistatic Mechanical Testing of Potential Mock Materials

6.1.1 HMX Mock Candidates

HMX was used as a standard against which to judge IDOX, PFBA, and N-BPFPO as potential simulants. Comparisons were made on the basis of hardness and elastic modulus. PFBA had a 78% difference from HMX in elastic modulus and a 76% difference in hardness, and therefore was not considered any further as a potential mock. N-BPFPO had a 30% difference from HMX in elastic modulus and a 56% difference in hardness, and consequently was also discarded as a possibility to mock HMX. IDOX had a 7.5% difference from HMX in elastic modulus and 0% difference in hardness, and thus became the prime candidate for a new HMX mock. The similarity in hardness and elastic modulus indicate that IDOX can be used to test the mechanical response of composite structures typically containing HMX.

Upon the establishment of IDOX as the primary focus of this HMX mock investigation, the next area of interest was incipient plasticity. When yielding occurs in both materials, the loads (and therefore stresses) at which dislocations are nucleated appear to be similar. However, in the as-received state, due to the frequency with which plasticity begins at the onset of indentation, in IDOX, it appears that IDOX may have a higher mechanical defect density than the HMX (for powders of the same size).

6.1.2 PETN Mock Candidates

PETN was used as a standard against which to judge erythritol, PFBA, 246 TFBA, HFPT, and N-BPFPO as potential simulants. Comparisons were made on the basis of hardness and elastic modulus. PFBA had a 62% difference from PETN in elastic modulus and 47% difference in hardness, and therefore was not considered further as a potential mock. HFPT had a 59% difference from PETN in elastic modulus and a 27% difference in hardness, and therefore was also no longer considered as a potential mock. N-BPFPO had a 16% difference from PETN in elastic modulus and a 2% difference in hardness, but while these mechanical properties were similar, the thermal properties as measured by DSC were too dissimilar, and so N-BPFPO was discarded as a potential PETN mock. 246 TFBA had a 26% difference in elastic modulus from PETN and a 20% difference in hardness, and was selected for continued consideration as a potential mock. Erythritol had a 39% difference in elastic modulus and a 170% difference in hardness, and was selected for continued consideration as a potential mock with the understanding that it would not be suitable in applications where hardness was of concern. Hardness of 246 TFBA appears to be sensitive to crystallization conditions, so for cases in which hardness is of concern in mocking PETN, it may be necessary to closely monitor crystallization conditions. It was determined that either of 246 TFBA or erythritol may be suitable to test the mechanical response of composite structures typically containing PETN depending on the situation. Yield behavior between PETN and erythritol is significantly more comparable than for 246 TFBA, though this is not expected to be relevant in typical processing.

6.2 Indentation-Induced Fracture Response of Molecular Crystals

6.2.1 HMX and IDOX Fracture

Pyramidal indenter probes of varying acuity were used to initiate fracture in HMX and IDOX in order to study and compare fracture toughness and mechanisms by which fracture propagates in each material. Fracture was observed optically when possible, and also determined using an unloading analysis method. Fracture toughness was calculated using two different methods, only one of which requiring measurement of the crack length.

Indentation fracture in IDOX initiated between 100 mN and 300 mN, with indents at loads lower than 100 mN displaying no fracture, and all indents at loads of 300 mN or higher

displaying fracture. Both radial and lateral cracks were observed. Cracks often emanated from the sides of indents rather than corners, characteristic of secondary radial fracture. HMX indentation fracture also initiated over a range, but between 4 mN and 8 mN, with all indents at loads of 4 mN or lower displaying no fracture, and all indents at loads of 8 mN or higher displaying fracture. Lateral fracture was extremely prevalent in HMX, and was often indicated on the unloading traces by the presence of pop-outs.

First order estimates of the toughness using a load – radial crack model by Morris and Cook give a toughness of 0.26 MPa $m^{-1/2}$ and 0.38 MPa $m^{-1/2}$ for HMX and IDOX respectively. First order estimates of toughness using a cracking threshold load model give a toughness of 0.219 MPa $m^{-1/2}$ and 0.572 MPa $m^{-1/2}$ for HMX and IDOX respectively. These two models gave similar values for HMX, but their estimates for IDOX varied much more. It is expected that this is because these models, especially the Morris and Cook model which requires measurement of a crack length, are designed for an idealized model with typical radial fracture, which does not describe these materials well.

Since IDOX is under consideration as a mechanical mock for HMX, these indentation fracture results indicate that the ability of IDOX to simulate the mechanical behavior of HMX is best suited to those cases where elasticity and plasticity, and not fracture, are the dominant deformation mechanisms.

6.2.2 PETN, 246 TFBA, and Erythritol Fracture

Fracture toughness in PETN, 246 TFBA, and erythritol were studied in much the same way as HMX and IDOX, with pyramidal indenter probes of varying acuity initiating fracture events and unloading curve analysis used as a detection method. Unlike in HMX and IDOX, however, the toughness of these materials was so low that the scale of indentation was too small for optical inspection of cracks. Analysis was done entirely with unloading curves.

Indentation fracture for PETN, 246 TFBA, and erythritol initiated at even the lowest load applied, 500 µN. It was decided to not continue testing below that load, because at very low loads and depths there can be significant noise, and this load is already well below the stress level that these materials are expected to encounter in normal processing. Because a true fracture

threshold was not determined, toughness of PETN, 246 TFBA, and erythritol cannot be calculated with a known degree of accuracy, but a maximum possible toughness value was calculated as 0.0771 MPa $m^{-1/2}$, 0.0896 MPa $m^{-1/2}$, and 0.0653 MPa $m^{-1/2}$ for PETN, 246 TFBA, and erythritol respectively.

The extremely low toughness of these materials gave rise to concern that previous low-load indents with broad probes had fractured, rendering resultant measurements invalid. To resolve this, PETN was indented with this broad probe at a range of loads and the indent impressions imaged with scanning probe microscopy. No fracture was seen below 8 mN, and since the measurements in question had been collected from 1 mN indents, this concern was put to rest.

6.2.3 General Fracture Trends

The unloading analysis technique used here had previously never been applied to materials such as these, brittle and anisotropic molecular crystals that differ significantly from ideal models. While unloading analysis proved to be over 90% accurate, optical inspection of indent impressions revealed some superimposable unloading curves to be false negatives, demonstrating the value of a secondary detection technique when possible; however, in cases where fracture toughness is too low to optically view indent impressions created below the fracture threshold, unloading analysis can be a particularly useful and informative tool. Analyzing only the unloading portion of the load-depth curve can also inform on the prevalence of lateral fracture, as many indents with significant lateral cracking can be identified via pop-outs on the unloading trace.

The first-order fracture toughness measurements for these materials varied significantly, with the toughest material (IDOX) being up to 9 times tougher than the weakest material (erythritol) despite all being somewhat similar materials, all being molecular crystals with comparable density, elastic modulus, and hardness. This range should be taken into consideration when choosing mock materials, as generalizations cannot necessarily be made about unmeasured properties.

6.3 Indenter Orientation Effects In Molecular Crystals

6.3.1 Quasistatic Orientation Results

In all experiments leading up to this point, high levels of variability had been seen for each material, and unexpected fracture patterns had been observed in both IDOX and HMX. Given that these materials are known to be highly anisotropic, and testing was being done with nonaxisymmetric indenters, the question arose of whether these results were biased by in-plane orientation effects. In order to determine if this was the case for quasistatic measurements, crystals were indented with both axisymmetric (conical) as well as nonaxisymmetric (pyramidal) probes as the sample was periodically rotated in order to vary the in-plane orientation. Elastic modulus for individual crystals was compared on the basis of both indenter geometry and as a function of angle. From this, elastic modulus as measured by nanoindentation showed only stochastic variation, independent of in-plane indenter orientation, or lack thereof in the case of an axisymmetric probe. This result was seen in four different materials (PETN, HMX, erythritol, IDOX), all molecular crystals, representing three different crystals structures with varying levels of asymmetry (tetragonal, monoclinic, triclinic). This consistently orientation-agnostic result indicated that past measurements were not biased by the probe orientation, nor must care be taken in the future to orient the probe a certain way or vary the ways in which it is oriented.

6.3.2 Fracture Orientation and Implications Regarding Previous Fracture Trends

In pursuit of determining whether fracture toughness measurements had been biased by in-plane indenter orientation, a single IDOX crystal was indented with a sharp pyramidal indenter at loads high enough to ensure fracture, and the sample was periodically rotated in order to vary the in-plane orientation. The indentation-induced fracture was quite strongly oriented in a preferred direction, but this direction was entirely independent of indenter orientation or geometry; the indenter orientation did not impact the direction in which cracks propagated, and the pyramidal shape of the indenter did not impact where the cracks originated. While it is typical for cracks to emanate from the corners of pyramidal indenters, here cracks appeared from seemingly random points along the flat sides of the indent impression, sometimes more near to one corner and at other times centered between two corners.

Because of this tendency of cracks to ignore both indenter orientation and geometry, it can be concluded that indentation is an effective method of testing fracture behavior, as fracture response is largely driven by stress fields within the material rather than the indenter itself. Future work could be done here to determine exactly what these preferred orientations are for each of these materials and to what degree fracture toughness varies between specific crystallographic planes.

6.4 Overall Conclusions

As stated at the beginning of this chapter, the objectives of this work were twofold. The overall conclusions will be given for each objective individually:

(1) To determine the suitability and robustness of nanoindentation as a primary screening technique for new mock material candidates

Nanoindentation was used here to screen new mock material candidates on the basis of hardness, elastic modulus, yield response, and fracture toughness. This technique allowed for large sample sizes to give an inclusive representation of each material, and also returned preliminary results very quickly, providing quick turnaround on proposed materials. As a result, preferred materials were quickly given priority in subsequent tests that were more expensive, difficult, required more material, and/or required more sample preparation. Similarly, unsuitable materials were able to be identified as such before significant amounts of time and money were spent on them. This project has successfully proven nanoindentation to be a valuable primary screening technique for new mock material candidates, and as a result of this project it has been established as such.

(2) To identify appropriate mock materials for selected explosives

Three materials were initially selected as potential mocks for HMX, and as a result of nanoindentation tests done in this project, one of them, IDOX, was found to have remarkably similar quasistatic mechanical properties in yield, elastic modulus, and especially hardness where the two materials are identical. The materials are nearly perfect quasistatic mocks, but may not

be suitable in applications where fracture is expected, as IDOX is significantly tougher than HMX.

Five materials were initially selected as potential mocks for IDOX, and as a result of nanoindentation tests done in this project, two of them, 246 TFBA and erythritol, have been selected as possible mechanical mocks. 246 TFBA is very similar to PETN in terms of elastic modulus and hardness, whereas erythritol is an excellent match for PETN in terms of yield. Both materials seem suitable to mock the poor fracture toughness of PETN.

The results of this work highlighted the difficulty of mocking molecular crystals, which can display significant variation in all properties in ways that may not be consistent from one material to the next; little correlation was seen between elastic modulus and fracture toughness, hardness and fracture toughness, yield point and fracture toughness, hardness and yield point, etc. There are also high levels of anisotropy which can result in responses that may not be what previous work has shown to be possible, given that most prior work in things such as fracture has been done in isotropic amorphous or metallic materials. With the addition of this work to the literature, future studies can be more informed on the nature of responses that can be expected from this class of materials.

APPENDIX

Unloading Curves and Corresponding Cube Corner Indents, Supplemental to Chapter 4

Idoxuridine

Superimposable unloading load-depth curves for IDOX indented to a maximum load of 100 mN, and an optical micrograph of the corresponding cube corner indent with visible slip but no radial fracture

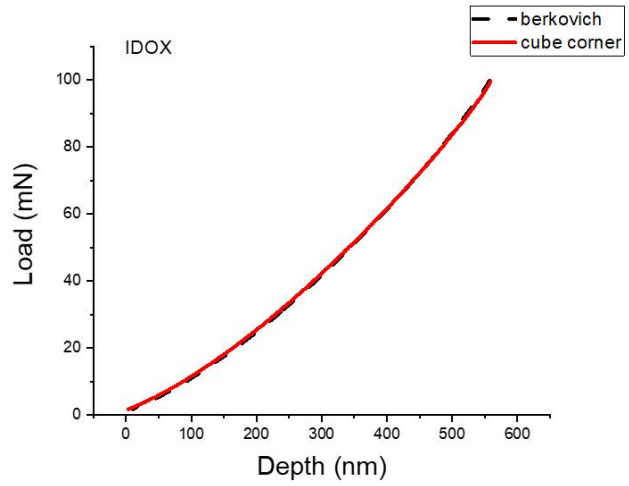

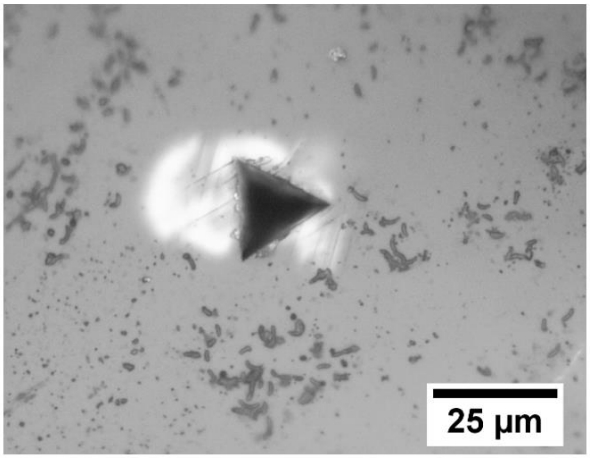

Nearly superimposable unloading load-depth curves for IDOX indented to a maximum load of 125 mN, and an optical micrograph of the corresponding cube corner indent with visible radial fracture. This is a false negative result.

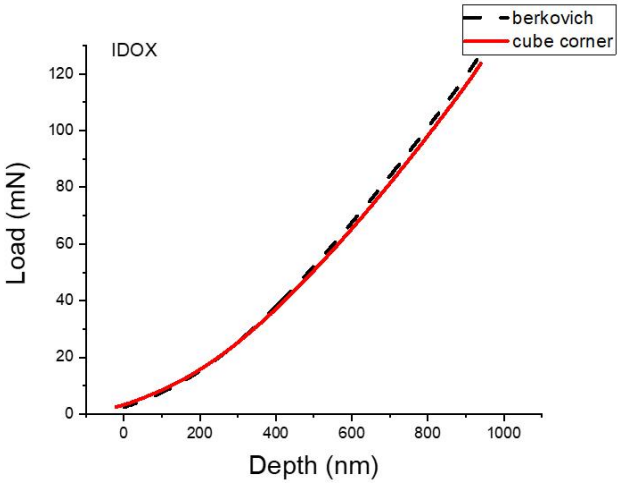

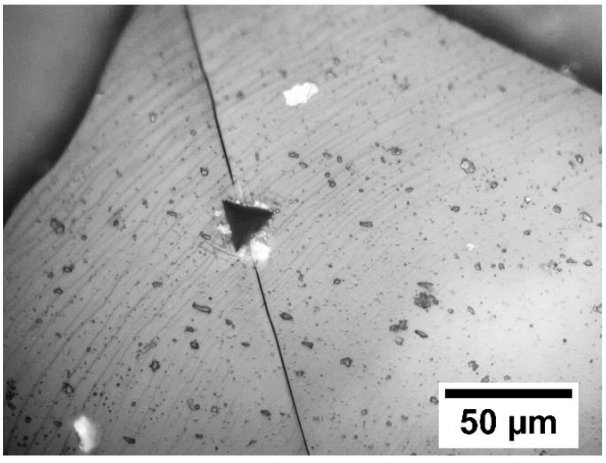

Nearly superimposable unloading load-depth curves for IDOX indented to a maximum load of 125 mN, and an optical micrograph of the corresponding cube corner indent with visible slip but no radial fracture

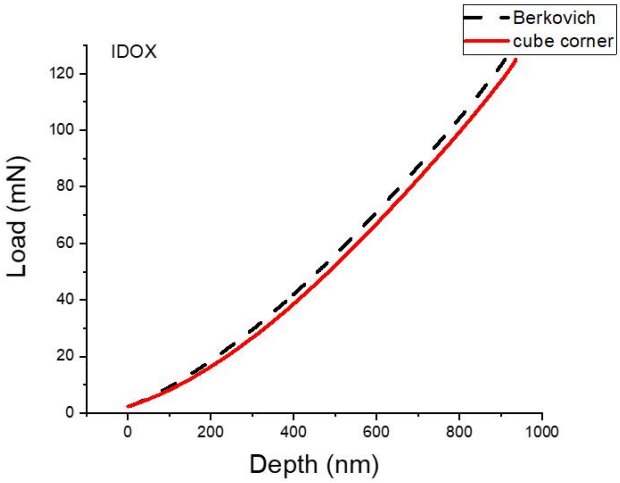

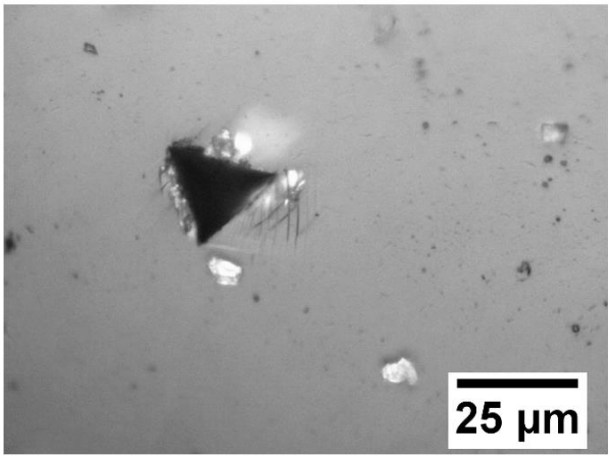

Non superimposable unloading load-depth curves for IDOX indented to a maximum load of 200 mN, and an optical micrograph of the corresponding cube corner indent with visible radial fracture

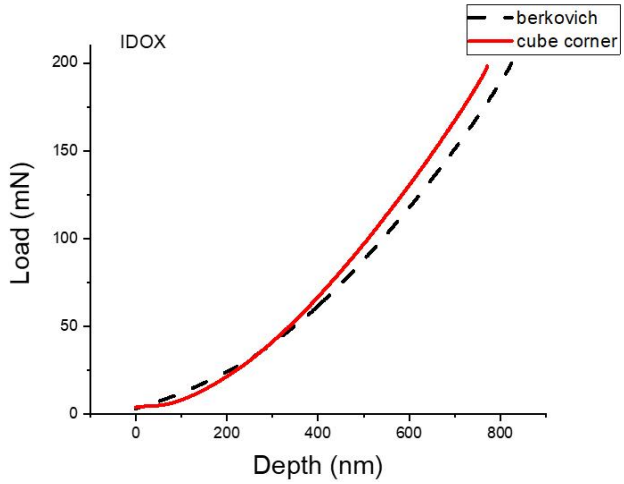

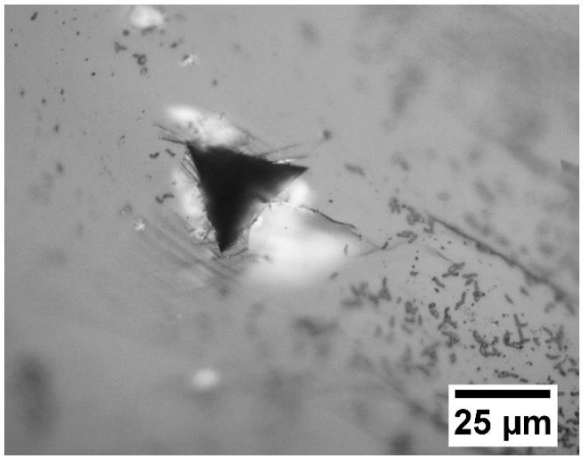

Non superimposable unloading load-depth curves for IDOX indented to a maximum load of 250 mN, and an optical micrograph of the corresponding cube corner indent with visible radial fracture

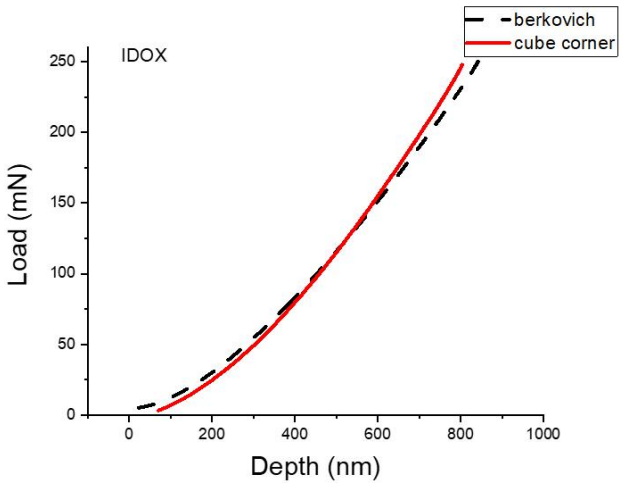

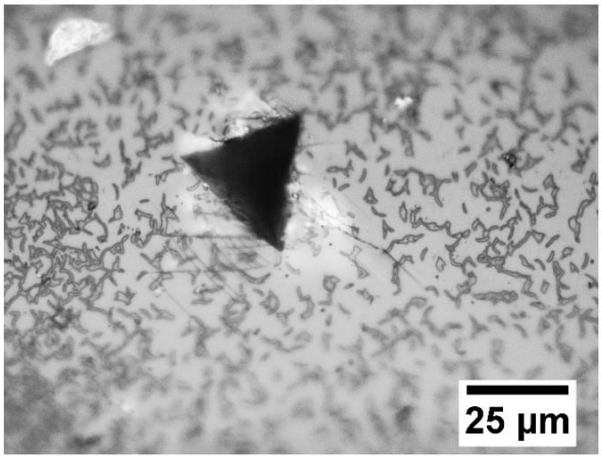

Non superimposable unloading load-depth curves for IDOX indented to a maximum load of 300 mN, and an optical micrograph of the corresponding cube corner indent with visible radial fracture

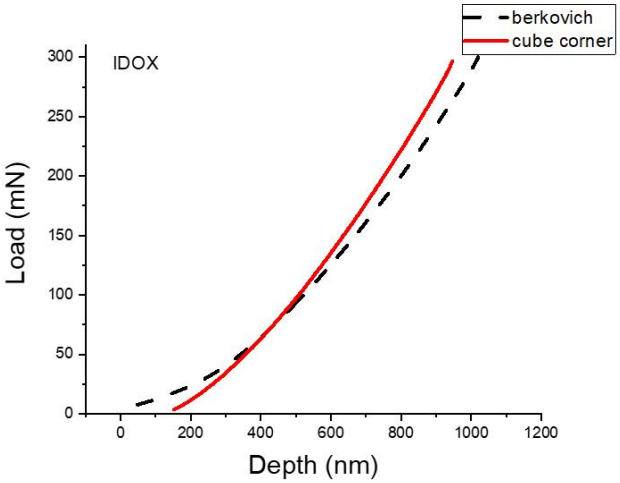

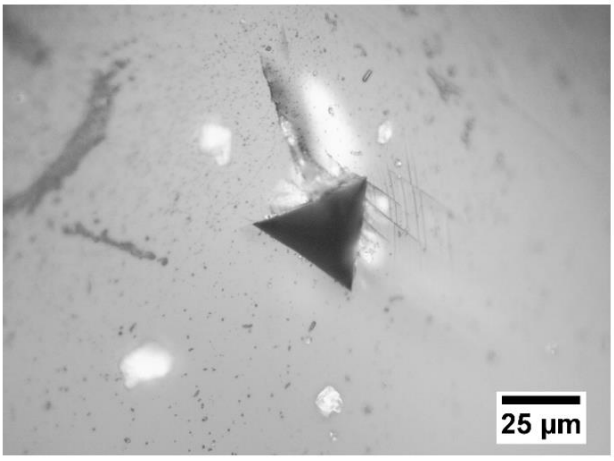

Superimposable unloading load-depth curves for IDOX indented to a maximum load of 300 mN, and an optical micrograph of the corresponding cube corner indent with visible radial fracture. This is a false negative result.

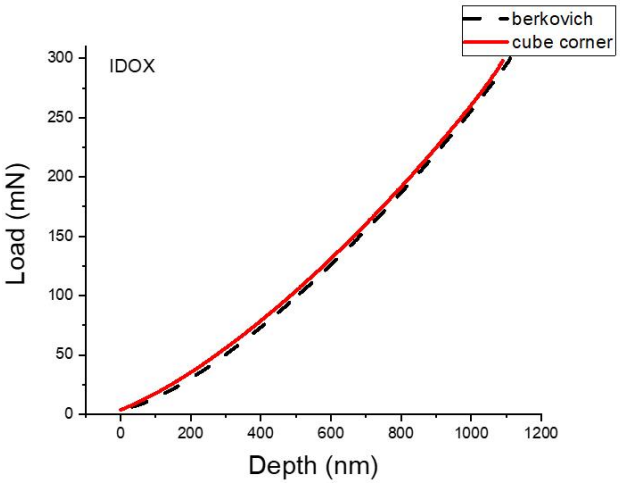

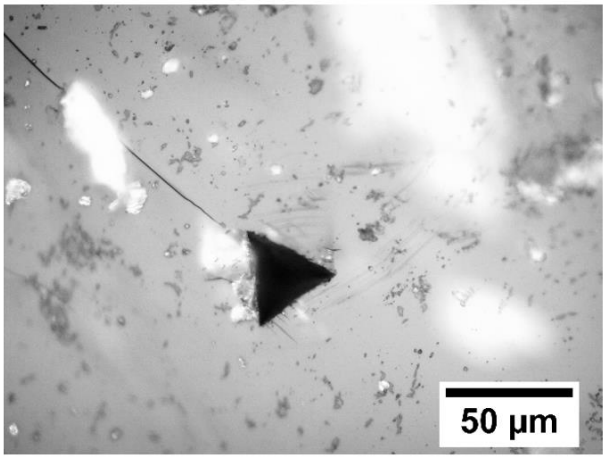

HMX

Non superimposable unloading load-depth curves for HMX indented to a maximum load of 8 mN, and an optical micrograph of the corresponding cube corner indent with visible radial fracture

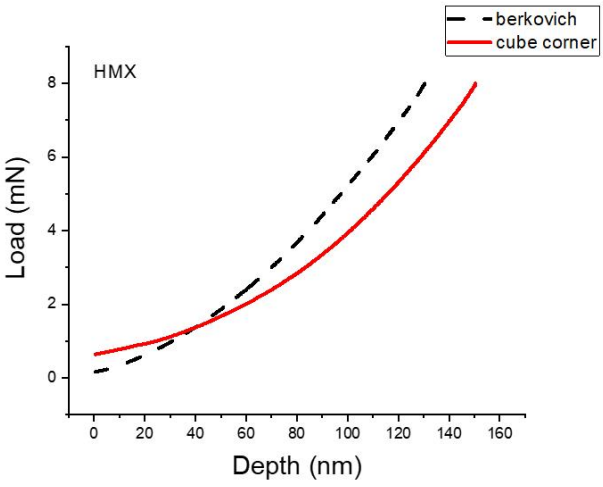

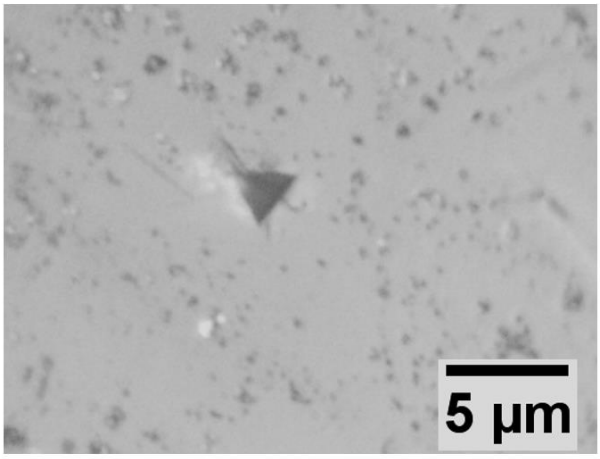

Non superimposable unloading load-depth curves for HMX indented to a maximum load of 15 mN, and an optical micrograph of the corresponding cube corner indent with visible radial fracture

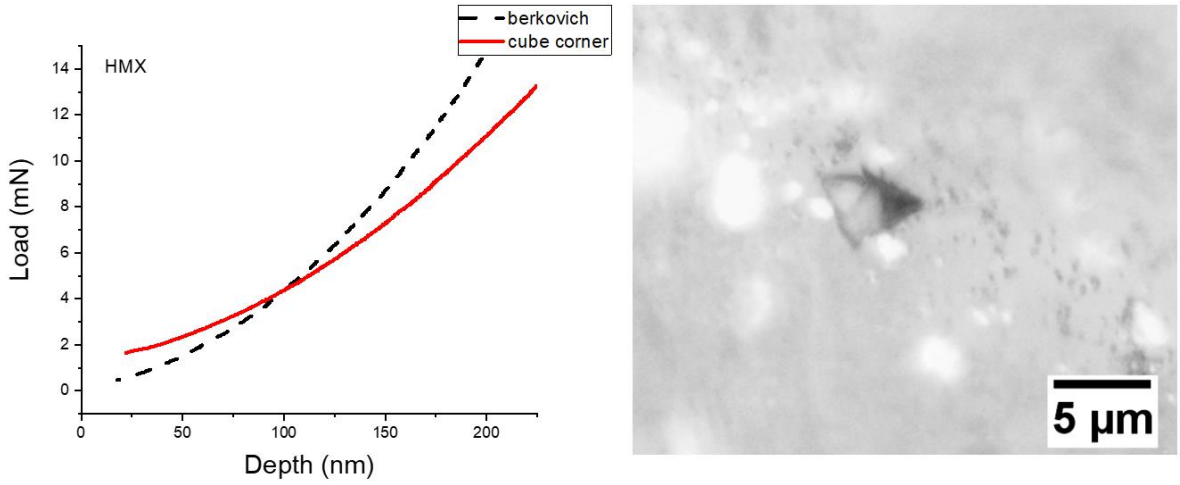

Non superimposable unloading load-depth curves for HMX indented to a maximum load of 15 mN, and an optical micrograph of the corresponding cube corner indent with visible radial fracture

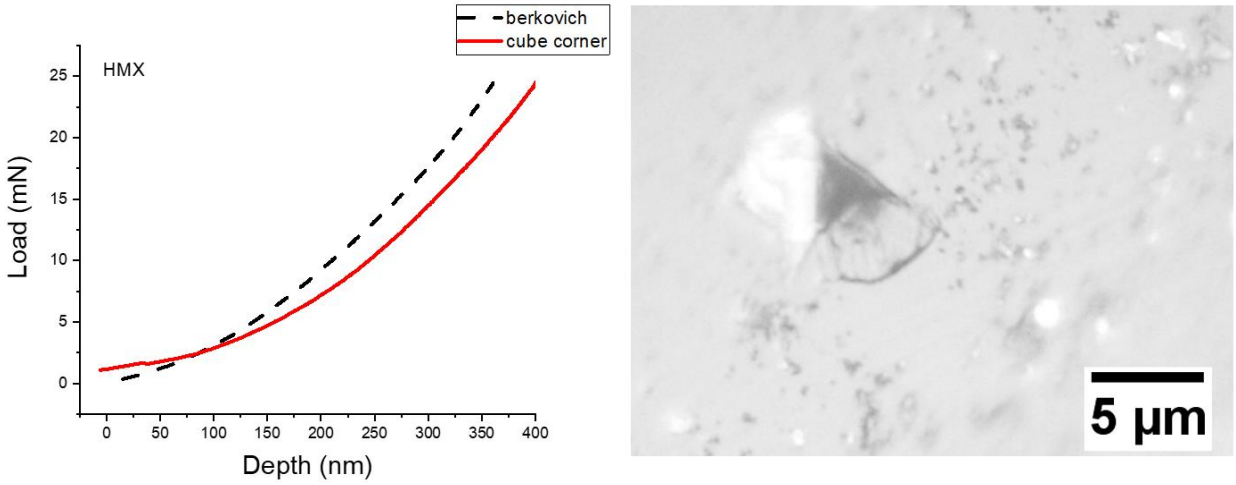

Non superimposable unloading load-depth curves for HMX indented to a maximum load of 100 mN with cube corner pop-outs, and an optical micrograph of the corresponding cube corner indent with visible radial fracture

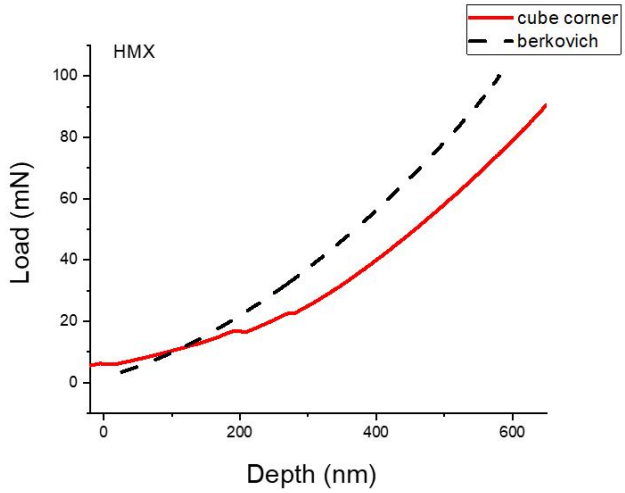

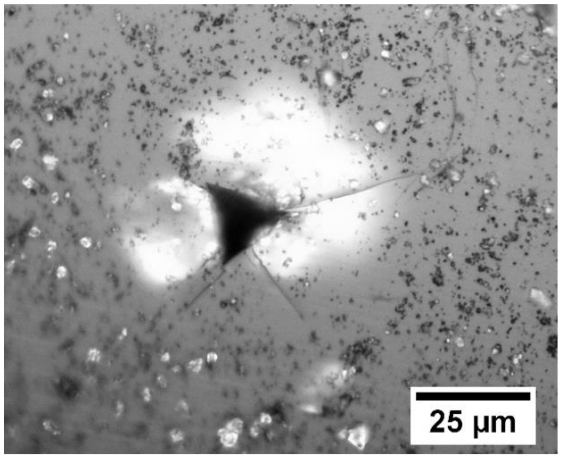

Non superimposable unloading load-depth curves for HMX indented to a maximum load of 125 mN with cube corner pop-outs, and an optical micrograph of the corresponding cube corner indent with visible radial fracture

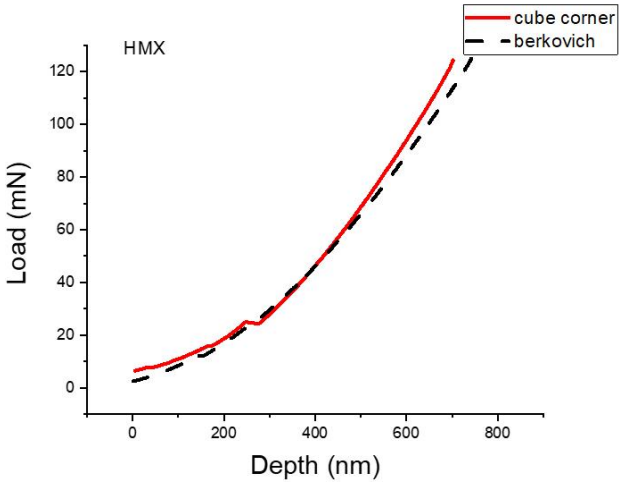

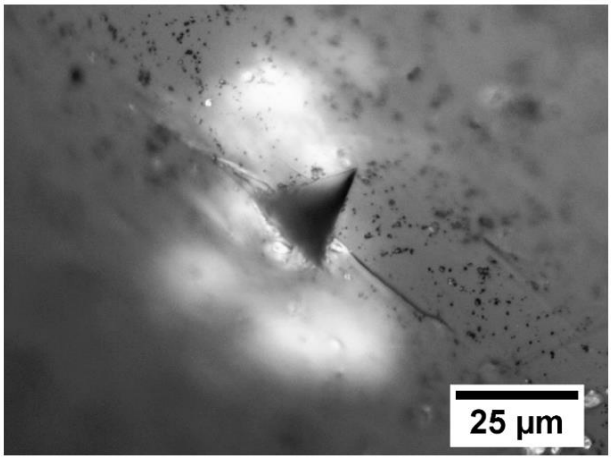

Non superimposable unloading load-depth curves for HMX indented to a maximum load of 200 mN with Berkovich and cube corner pop-outs, and an optical micrograph of the corresponding cube corner indent with visible radial fracture

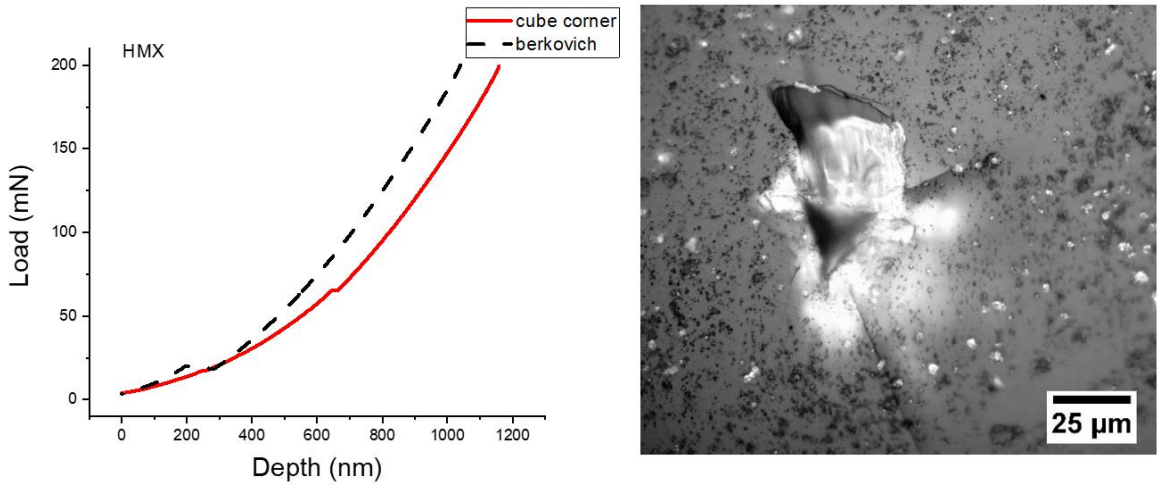

Nearly superimposable unloading load-depth curves for HMX indented to a maximum load of 250 mN with Berkovich and cube corner pop-outs, and an optical micrograph of the corresponding cube corner indent with visible radial fracture. This is a false negative result.

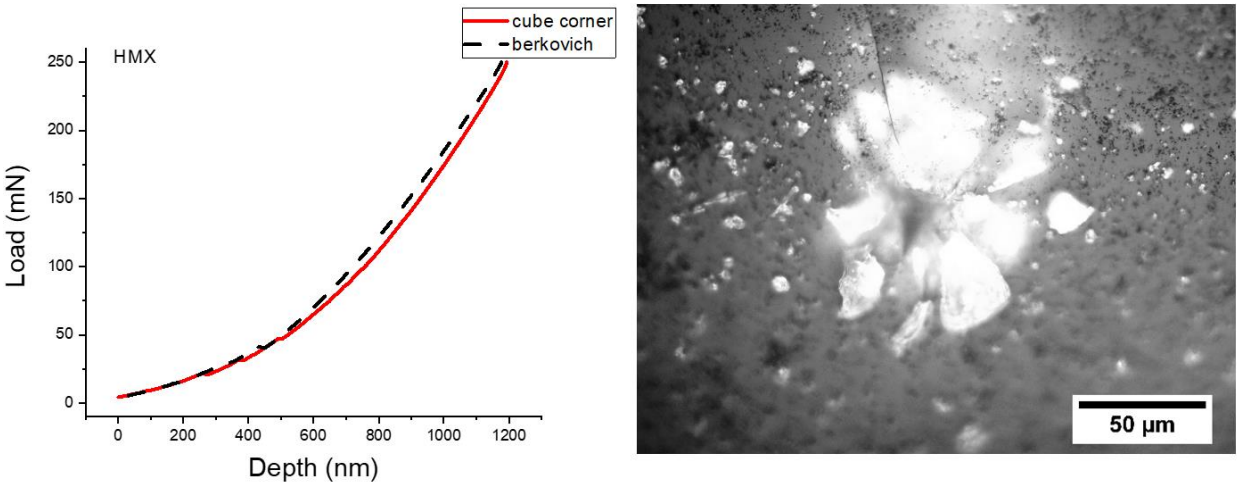

REFERENCES

1. Wright, J. D. *Molecular crystals*. (Cambridge University Press, 1995).
2. Mohammed, H., Briscoe, B. J. & Pitt, K. G. The interrelationship between the compaction behaviour and the mechanical strength of pure pharmaceutical tablets. *Chem. Eng. Sci.* **60**, 3941–3947 (2005).
3. Duncan-Hewitt, W. C. & Weatherly, G. C. Modeling the Uniaxial Compaction of Pharmaceutical Powders Using the Mechanical Properties of Single Crystals. II: Brittle Materials. *J. Pharm. Sci.* **79**, 273–278 (1990).
4. Jain, S. Mechanical properties of powders for compaction and tableting: an overview. *Pharm. Sci. Technolo. Today* **2**, 20–31 (1999).
5. Luscher, D. *et al.* Using Neutron Diffraction to Investigate Texture Evolution During Consolidation of Deuterated Triaminotrinitrobenzene (d-TATB) Explosive Powder. *Crystals* **7**, 138 (2017).
6. Elban, W. L. & Chiarito, M. A. Quasi-static compaction study of coarse HMX explosive. *Powder Technol.* **46**, 181–193 (1986).
7. Stepanov, V., Patel, R. B., Mudryy, R. & Qiu, H. Investigation of Nitramine-Based Amorphous Energetics. *Propellants, Explos. Pyrotech.* **41**, 142–147 (2016).
8. Yu, L. Amorphous pharmaceutical solids: preparation, characterization and stabilization. *Adv. Drug Deliv. Rev.* **48**, 27–42 (2001).
9. Bower, J. K., Kolb, J. R. & Pruneda, C. O. Polymeric Coatings Effect on Surface Activity and Mechanical Behavior of High Explosives. *Ind. Eng. Chem. Prod. Res. Dev.* **19**, 326–329 (1980).
10. Vekilov, P. G. & Rosenberger, F. Dependence of lysozyme growth kinetics on step sources and impurities. *J. Cryst. Growth* **158**, 540–551 (1996).
11. Anderson, K. J. Energetic Materials, Part I: Black Powder, Nitroglycerin, and Dynamite. *MRS Bull.* **14**, 84–86 (1989).
12. Anderson, K. J. Energetic Materials, Part II: TNT and Other Military Explosives. *MRS Bull.* **14**, 63–64 (1989).
13. Cooper, P. W. & Kurowski, S. R. *Introduction to the Technology of Explosives*. (Wiley-VCH, Inc., 1996).

14. Matyáš, R., Šelešovský, J. & Musil, T. Sensitivity to friction for primary explosives. *J. Hazard. Mater.* **213**, 236–241 (2012).
15. Millett, J. C. F. & Bourne, N. K. The shock Hugoniot of a plastic bonded explosive and inert simulants. *J. Phys. D Appl. Phys.* **37**, 2613–2617 (2004).
16. Sheffield, S. A., Gustavsen, R. L. & Alcon, R. R. Porous HMX initiation studies - sugar as an inert simulant. *AIP Conf. Proc.* **429**, 575–578 (1998).
17. Ramos, K. J. & Bahr, D. F. Mechanical behavior assessment of sucrose using nanoindentation. *J. Mater. Res.* **22**, 2037–2045 (2007).
18. Ramos, K. J., Hooks, D. E. & Bahr, D. F. Direct observation of plasticity and quantitative hardness measurements in single crystal cyclotrimethylene trinitramine by nanoindentation. *Philos. Mag.* **89**, 2381–2402 (2009).
19. Taw, M. R., Yeager, J. D., Hooks, D. E., Carvajal, T. M. & Bahr, D. F. The mechanical properties of as-grown noncubic organic molecular crystals assessed by nanoindentation. *J. Mater. Res.* 1–10 (2017) doi:10.1557/jmr.2017.219.
20. Taw, M. R. & Bahr, D. F. The Mechanical Properties of Minimally Processed RDX. *Propellants, Explos. Pyrotech.* **42**, 659–664 (2017).
21. Yeager, J. D., Luo, S. N., Jensen, B. J., Fezzaa, K., Montgomery, D. S. & Hooks, D. E. High-speed synchrotron X-ray phase contrast imaging for analysis of low-Z composite microstructure. *Compos. Part A Appl. Sci. Manuf.* **43**, 885–892 (2012).
22. Eilerman, D. & Rudman, R. Refinement of pentaerythritol. *Acta Crystallogr. Sect. B Struct. Crystallogr. Cryst. Chem.* **35**, 2458–2460 (1979).
23. Yeager, J. D., Higginbotham Duque, A. L., Shorty, M., Bowden, P. R. & Stull, J. A. Development of inert density mock materials for HMX. *J. Energ. Mater.* **36**, 253–265 (2018).
24. Wilde, Z. & Peralta, P. Hugoniot of Meso-Erythritol as an Inert Surrogate for PETN (symp). *Bull. Am. Phys. Soc.* **64**, (2019).
25. Hertz, H., Jones, D. E. & Schott, G. A. Miscellaneous papers by H. Hertz. *Jones and Schott, London, Macmillan* (1896).
26. Auerbach, F. Smithsonian Report for 1891. *Gov. Print. Off. Washingt.* 207–236 (1893).
27. Brinell, J. A. Brinell's method of determining hardness and their properties of iron and steel.''II. Cong. Int. Methodes d''Essai, Paris,''(translated to English by A. Wahlberg). *J.*

Iron Steel Inst **59**, 243–298 (1901).

28. Meyer, E. Untersuchungen uber Harteuprufung und Harte. *Zt. Vereines Deutsch. Ing. 52, 645* **654**, (1908).
29. Smith, R. L. & Sandland, G. E. Some notes on the use of a diamond pyramid for hardness testing. *Iron Steel Inst* **1**, 285–304 (1925).
30. Berkovich, E. S. Three faceted diamond pyramid for micro-hardness testing. *Ind. Diam. Rev.* **11**, 129 (1951).
31. Loubet, J. L., Georges, J. M., Marchesini, O. & Meille, G. Vickers indentation curves of magnesium oxide (MgO). (1984).
32. Newey, D., Wilkins, M. A. & Pollock, H. M. An ultra-low-load penetration hardness tester. *J. Phys. E.* **15**, 119 (1982).
33. Kiran, M. S. R. N., Varughese, S., Reddy, C. M., Ramamurty, U. & Desiraju, G. R. Mechanical anisotropy in crystalline saccharin: Nanoindentation studies. *Cryst. Growth Des.* **10**, 4650–4655 (2010).
34. Olusanmi, D., Roberts, K. J., Ghadiri, M. & Ding, Y. The breakage behaviour of Aspirin under quasi-static indentation and single particle impact loading: Effect of crystallographic anisotropy. *Int. J. Pharm.* **411**, 49–63 (2011).
35. Hudson, R. J., Zioupos, P. & Gill, P. P. Investigating the Mechanical Properties of RDX Crystals Using Nano-Indentation. *Propellants, Explos. Pyrotech.* **37**, 191–197 (2012).
36. Egart, M., Janković, B., Lah, N., Ilić, I. & Srčič, S. Nanomechanical properties of selected single pharmaceutical crystals as a predictor of their bulk behaviour. *Pharm. Res.* **32**, 469–481 (2015).
37. Mathew, N. & Sewell, T. D. Nanoindentation of the Triclinic Molecular Crystal 1,3,5-Triamino- 2,4,6-trinitrobenzene: A Molecular Dynamics Study. doi:10.1021/acs.jpcc.6b01103.
38. Elban, W. L., Hoffsommer, J. C. & Armstrong, R. W. X-ray orientation and hardness experiments on RDX explosive crystals. *J. Mater. Sci.* **19**, 552–566 (1984).
39. Yeager, J. D., Ramos, K. J., Singh, S., Rutherford, M. E., Majewski, J. & Hooks, D. E. Nanoindentation of explosive polymer composites to simulate deformation and failure. *Mater. Sci. Technol.* **28**, 1147–1155 (2012).
40. Oliver, W. C. & Pharr, G. M. An improved technique for determining harness and elastic

modulus using load and displacement sensing indentation experiments. *J. Mater. Res.* **7**, 1564–1583 (1992).

41. Johnson, K. L. *Contact Mechanics*. (Cambridge University Press, 1985).
42. Fischer-Cripps, A. C. *The Handbook of f Nanoindentation*. (2009). doi:10.1201/b12116.
43. Xu, Z.-H. & Li, X. Effect of sample tilt on nanoindentation behaviour of materials. *Philos. Mag.* **87**, 2299–2312 (2007).
44. Page, T. F., Oliver, W. C. & McHargue, C. J. The deformation behavior of ceramic crystals subjected to very low load (nano)indentations. *J. Mater. Res.* **7**, 450–473 (1992).
45. Lodes, M. A., Hartmaier, A., Gö Ken, M. & Durst, K. Influence of dislocation density on the pop-in behavior and indentation size effect in CaF 2 single crystals: Experiments and molecular dynamics simulations. *Acta Mater.* **59**, 4264–4273 (2011).
46. Zbib, A. A. & Bahr, D. F. Dislocation Nucleation and Source Activation during Nanoindentation Yield Points. *Metall. Mater. Trans. A* **38**, 2249–2255 (2007).
47. Barnoush, A., Welsch, M. T. & Vehoff, H. Correlation between dislocation density and pop-in phenomena in aluminum studied by nanoindentation and electron channeling contrast imaging. *Scr. Mater.* **63**, 465–468 (2010).
48. Barnoush, A. Correlation between dislocation density and nanomechanical response during nanoindentation. *Acta Mater.* **60**, 1268–1277 (2012).
49. Kelchner, C. L., Plimpton, S. J. & Hamilton, J. C. Dislocation nucleation and defect structure during surface indentation. *Phys. Rev. B* **58**, 11085 (1998).
50. Schuh, C. A., Mason, J. K. & Lund, A. C. Quantitative insight into dislocation nucleation from high-temperature nanoindentation experiments. *Nat. Mater.* **4**, 617–621 (2005).
51. Bahr, D. F., Kramer, D. E. & Gerberich, W. W. Non-linear deformation mechanisms during nanoindentation. *Acta Mater.* **46**, 3605–3617 (1998).
52. Lorenz, D., Zecker, A., Hilpert, U., Grau, P., Johansen, H. & Leipner, H. S. Pop-in effect as homogeneous nucleation of dislocations during nanoindentation. *Phys. Rev. B - Condens. Matter Mater. Phys.* **67**, 172101 (2003).
53. Morris, J. R., Bei, H., Pharr, G. M. & George, E. P. Size effects and stochastic behavior of nanoindentation pop in. *Phys. Rev. Lett.* **106**, 165502 (2011).
54. Salehinia, I., Lawrence, S. K. & Bahr, D. F. The effect of crystal orientation on the stochastic behavior of dislocation nucleation and multiplication during nanoindentation.

Acta Mater. **61**, 1421–1431 (2013).

55. Ramos, K. J., Bahr, D. F. & Hooks, D. E. Defect and surface asperity dependent yield during contact loading of an organic molecular single crystal. *Philos. Mag*. **91**, 1276–1285 (2011).
56. Lawn, B. & Wilshaw, R. Indentation fracture: principles and applications. *J. Mater. Sci.* **10**, 1049–1081 (1975).
57. Khan, Z., Faisal, H. & Tarefder, R. Fracture toughness measurement of asphalt concrete by nanoindentation. in *PROCEEDINGS OF THE ASME INTERNATIONAL MECHANICAL ENGINEERING CONGRESS AND EXPOSITION, 2017 VOL 10* (2017).
58. Jungk, J. M. *et al*. Indentation fracture toughness and acoustic energy release in tetrahedral amorphous carbon diamond-like thin films. *Acta Mater*. **54**, 4043–4052 (2006).
59. Cai, X., Xu, Y., Zhong, L. & Liu, M. Fracture toughness of WC-Fe cermet in W-WC-Fe composite by nanoindentation. *J. Alloys Compd*. **728**, 788–796 (2017).
60. Guo, H., Jiang, C. B., Yang, B. J. & Wang, J. Q. On the fracture toughness of bulk metallic glasses under Berkovich nanoindentation. *J. Non. Cryst. Solids* **481**, 321–328 (2018).
61. Mannepalli, S. & Mangalampalli, K. Indentation Plasticity and Fracture Studies of Organic Crystals. *Crystals* **7**, 324 (2017).
62. Yen, C.-Y., Jian, S.-R., Tseng, Y.-C. & Juang, J.-Y. The deformation behavior and fracture toughness of single crystal YSZ(111) by indentation. *J. Alloys Compd*. **735**, 2423–2427 (2018).
63. Anstis, G. R., Chantikul, P., Lawn, B. R. & Marshall, D. B. A Critical Evaluation of Indentation Techniques for Measuring Fracture Toughness: I, Direct Crack Measurements. *J. Am. Ceram. Soc*. **64**, 533–538 (1981).
64. Chantikul, P., Anstis, G. R., Lawn, B. R. & Marshall, D. B. A Critical Evaluation of Indentation Techniques for Measuring Fracture Toughness: II, Strength Method. *J. Am. Ceram. Soc*. **64**, 539–543 (1981).
65. Fuller, E. R., Quinn, G. D. & Cook, R. F. Strength and Fracture Measurements at the Nano Scale. in *AIP Conference Proceedings* vol. 931 156–160 (AIP, 2007).
66. Lawn, B. & Marshall, D. Hardness, Toughness, and Brittleness: An Indentation Analysis. *J. Am. Ceram. Soc*. **62**, 347.

67. Cook, R. F. & Pharr, G. M. Direct Observation and Analysis of Indentation Cracking in Glasses and Ceramics. *J. Am. Ceram. Soc.* **73**, 787–817 (1990).

68. Jang, J. & Pharr, G. M. Influence of indenter angle on cracking in Si and Ge during nanoindentation. *Acta Mater.* **56**, 4458–4469 (2008).

69. Morris, D. J. & Cook, R. F. Radial Fracture During Indentation by Acute Probes: I, Description by an Indentation Wedging Model. *Int. J. Fract.* **136**, 237–264 (2005).

70. Morris, D. J., Myers, S. B. & Cook, R. F. Sharp probes of varying acuity: Instrumented indentation and fracture behavior. *J. Mater. Res.* (2004) doi:10.1557/jmr.2004.19.1.165.

71. Morris, D. J. Instrumented Indentation Contact with Sharp Probes of Varying Acuity. in *MRS Proceedings* vol. 1049 AA06-09 (2007).

72. Pharr, G. M. & Bolshakov, A. Understanding nanoindentation unloading curves. *J. Mater. Res.* **17**, 2660–2671 (2002).

73. Woirgard, J., Tromas, C., Girard, J. C. & Audurier, V. Study of the mechanical properties of ceramic materials by the nanoindentation technique. *J. Eur. Ceram. Soc.* **18**, 2297–2305 (1998).

74. Jian, S.-R. & Lee, Y.-H. Nanoindentation-induced interfacial fracture of ZnO thin films deposited on Si (1 1 1) substrates by atomic layer deposition. *J. Alloys Compd.* **587**, 313–317 (2014).

75. Brunelli, M., Wright, J. P., Vaughan, G. B. M., Mora, A. J. & Fitch, A. N. Solving larger molecular crystal structures from powder diffraction data by exploiting anisotropic thermal expansion. *Angew. Chemie Int. Ed.* **42**, 2029–2032 (2003).

76. Turner, M. J., Thomas, S. P., Shi, M. W., Jayatilaka, D. & Spackman, M. A. Energy frameworks: insights into interaction anisotropy and the mechanical properties of molecular crystals. *Chem. Commun.* **51**, 3735–3738 (2015).

77. Lawrence, S. K., Bahr, D. F. & Zbib, H. M. Crystallographic orientation and indenter radius effects on the onset of plasticity during nanoindentation. *J. Mater. Res.* **27**, 3058–3065 (2012).

78. Maughan, M. R., Carvajal, M. T. & Bahr, D. F. Nanomechanical testing technique for millimeter-sized and smaller molecular crystals. *Int. J. Pharm.* **486**, 324–330 (2015).

79. Groom, C. R., Bruno, I. J., Lightfoot, M. P. & Ward, S. C. The Cambridge structural database. *Acta Crystallogr. Sect. B Struct. Sci. Cryst. Eng. Mater.* **72**, 171–179 (2016).

80. Raja, P. M. V. & Barron, A. R. LibreTexts. https://chem.libretexts.org/Bookshelves/Analytical_Chemistry/Book%3A_Physical_Methods_in_Chemistry_and_Nano_Science_(Barron)/07%3A_Molecular_and_Solid_State_Structure/7.01%3A_Crystal_Structure (2020).
81. Yamaguchi, K., Matsumura, G., Haga, N. & Shudo, K. Structure of N, N-bis (2, 3, 4, 5, 6-pentafluorophenyl) oxamide. *Acta Crystallogr. Sect. C Cryst. Struct. Commun.* **48**, 558–559 (1992).
82. Thurn, J. & Cook, R. F. Simplified area function for sharp indenter tips in depth-sensing indentation. *J. Mater. Res.* **17**, 1143–1146 (2002).
83. Brookes, C. A., Green, P., Harrison, P. H. & Moxley, B. Some observations on scratch and indentation hardness measurements. *J. Phys. D. Appl. Phys.* **5**, 1284 (1972).
84. Atkins, A. G. & Tabor, D. Plastic indentation in metals with cones. *J. Mech. Phys. Solids* **13**, 149–164 (1965).
85. Bishop, R. F., Hill, R. & Mott, N. F. The theory of indentation and hardness tests. *Proc. Phys. Soc.* **57**, 147 (1945).
86. Hill, R., Lee, E. H. & Tupper, S. J. The theory of wedge indentation of ductile materials. *Proc. R. Soc. London. Ser. A. Math. Phys. Sci.* **188**, 273–289 (1947).
87. Taw, M. R. Linking nanoscale mechanical behavior to bulk physical properties and phenomena of energetic materials. *Theses Diss. Available from ProQuest* (2016).
88. Askari, H. *et al.* A stochastic crystal plasticity framework for deformation of micro-scale polycrystalline materials. *Int. J. Plast.* **68**, 21–33 (2015).
89. Zhai, M. & McKenna, G. B. Mechanical properties of pentaerythritol tetranitrate(PETN) single crystals from nano-indentation: Depth dependent response at the nano meter scale. *Cryst. Res. Technol.* **51**, 414–427 (2016).
90. Maiti, A., Han, Y., Zaka, F. & Gee, R. H. In-situ Monitoring of Flow-Permeable Surface Area of High Explosive Powder using Small Sample Masses. *Propellants, Explos. Pyrotech.* **40**, 419–425 (2015).
91. Maiti, A. & Gee, R. H. PETN Coarsening–Predictions from Accelerated Aging Data. *Propellants, Explos. Pyrotech.* **36**, 125–130 (2011).
92. Salehinia, I., Perez, V. & Bahr, D. . Effect of vacancies on incipient plasticity during contact loading. *Philos. Mag.* **92**, 550–570.

93. Minor, A. M. *et al.* A new view of the onset of plasticity during the nanoindentation of aluminium. *Nat. Mater.* **5**, 697–702 (2006).
94. Maughan, M. R. & Bahr, D. F. Discontinuous yield behaviors under various pre-strain conditions in metals with different crystal structures. *Mater. Res. Lett.* **4**, 83–89 (2015).
95. Bahr, D. F., Jennerjohn, S. L. & Morris, D. J. Dislocation nucleation and multiplication in small volumes: The onset of plasticity during indentation testing. *JOM* **61**, 56–60 (2009).
96. Hooks, D. E., Ramos, K. J. & Bahr, D. F. The effect of cracks and voids on the dynamic yield of RDX single crystals. *AIP Conf. Proc.* **955**, 789–794 (2007).
97. Monroe, D. C. *(U) Historical PETN Pressing Data: 1965-78.* (2015).
98. Jing, Y., Zhang, Y., Blendell, J., Koslowski, M. & Carvajal, M. T. Nanoindentation Method To Study Slip Planes in Molecular Crystals in a Systematic Manner. *Cryst. Growth Des.* **11**, 5260–5267 (2011).
99. Wildfong, P. L. D., Hancock, B. C., Moore, M. D. & Morris, K. R. Towards an Understanding of the Structurally Based Potential for Mechanically Activated Disordering of Small Molecule Organic Crystals. *J. Pharm. Sci.* **95**, 2645–2656 (2006).
100. Mound, B. A. & Pharr, G. M. Nanoindentation of Fused Quartz at Loads Near the Cracking Threshold. *Exp. Mech.* **59**, 369–380 (2019).
101. Cook, R. F. Fracture sequences during elastic–plastic indentation of brittle materials. *J. Mater. Res.* **34**, 1633–1644 (2019).
102. Vlassak, J. J. & Nix, W. D. Measuring the Elastic Properties of Materials By Means of Indentation. *J. Mech. Phys. Solids* **42**, 1223–1245 (1994).

PUBLICATIONS

A Thermal and Nanomechanical Study of Molecular Crystals as Versatile Mocks for Pentaerythritol Tetranitrate

A. C. Burch, Z. R. Wilde, D. F. Bahr, J. D. Yeager. Crystals, vol. 10, pp. 126(1:15) (2020) DOI: 10.3390/cryst10020126

Indentation Fracture Behavior of Energetic and Inert Molecular Crystals

A. C. Burch, J. D. Yeager, D. F. Bahr. Journal of Materials Research, Vol. 34, Issue 23, pp. 3954-3963 (2019) DOI: 10.1557/jmr.2019.345

Nanoindentation of HMX and Idoxuridine to determine mechanical similarity

A. C. Burch, J. D. Yeager, D. F. Bahr. Crystals, vol. 7, pp. 335(1:9) (2017) DOI: 10.3390/cryst7110335